Quantum criticality in magnetically unstable $4f$- and $3d$-electron metals

Von der Fakultät für Elektrotechnik, Informationstechnik, Physik
der Technischen Universität Carolo-Wilhelmina zu Braunschweig

zur Erlangung des Grades einer Doktorin
der Naturwissenschaften (Dr. rer. nat.)
genehmigte Dissertation

von Daniela Rauch

aus Beckendorf-Neindorf, Oschersleben (Bode)

eingereicht am: 21.05.2015
Disputation am: 04.08.2015

1. Referent: apl. Prof. Dr. Stefan Süllow
2. Referent: Dr. F. Malte Grosche

Druckjahr: 2015

Vorveröffentlichungen der Dissertation

Teilergebnisse aus dieser Arbeit wurden mit Genehmigung der Fakultät für Elektrotechnik, Informationstechnik, Physik, vertreten durch den Betreuer der Arbeit, in folgenden Beiträgen vorab veröffentlicht:

Publikationen

D. Rauch, S. Süllow, M. Bleckmann, A. Buchsteiner, N. Stüßer, H.-H. Klauss, H. Luetkens, E. Bauer: *"Magnetic order in non-centrosymmetric $CePt_3B$"*, J. Phys.: Conf. Ser. **391**, 012055 (2012).

D. Rauch, S. Süllow, M. Bleckmann, B. Klemke, K. Kiefer, M.S. Kim, M. Aronson, E. Bauer: *"Phase diagram of $CePt_3B_{1-x}Si_x$"*, Phys. Rev. B **86**, 245104 (2012).

D. Rauch, M. Kraken, F. J. Litterst, S. Süllow, H. Luetkens, M. Brando, T. Förster, J. Sichelschmidt, A. Neubauer, C. Pfleiderer, W. J. Duncan, F. M. Grosche: *"Spectroscopic study of metallic magnetism in single-crystalline $Nb_{1-y}Fe_{2+y}$"*, Phys. Rev. B **91**, 174404 (2015).

D. Rauch, P. Horenburg, S. Hartwig, F. J. Litterst, S. Süllow, H. Luetkens, C. Baines, S. Yamazaki, H. Hidaka, H. Amitsuka, and E. Bauer: *"Magnetic ground-state properties of noncentrosymmetric $CePt_3B_{1-x}Si_x$"*, Phys. Rev. B **92**, 115114 (2015).

Tagungsbeiträge

D. Rauch, M. Bleckmann, S. Süllow, M. S. Kim, M. Aronson, and E. Bauer: *"Phase diagram of $CePt_3B_{1-x}Si_x$"* (poster), Frühjahrstagung der Deutschen Physikalischen Gesellschaft 2011, Dresden.

D. Rauch, M. Bleckmann, S. Süllow, M. S. Kim, M. Aronson, and E. Bauer: *"Phase diagram of $CePt_3B_{1-x}Si_x$"* (poster), International Conference on Strongly Correlated Electron Systems (SCES) 2011, Cambridge, UK.

D. Rauch, M, Kraken, F. J. Litterst, S, Süllow, and F. M. Grosche: *"A microscopic study of $Nb_{1-y}Fe_{2+y}$"* (poster), Frühjahrstagung der Deutschen Physikalischen Gesellschaft 2013, Regensburg.

D. Rauch, S. Hartwig, S. Süllow, H. Hidaka, S. Yamazaki, H. Amitsuka, and E. Bauer: *"A pressure study of $CePt_3B$"* (poster), Frühjahrstagung der Deutschen Physikalischen Gesellschaft 2013, Regensburg.

D. Rauch, M. Kraken, S. Süllow, F. J. Litterst, F. M. Grosche, and H. Luetkens: *"Microscopic investigation of the magnetic ground state of $Nb_{1-y}Fe_{2+y}$"* (poster), International Conference on Strongly Correlated Electron Systems (SCES) 2013, Tokyo, Japan.

D. Rauch, M. Kraken, S. Süllow, F. J. Litterst, F. M. Grosche, and H. Luetkens: *"Microscopic investigation of the magnetic ground state of $Nb_{1-y}Fe_{2+y}$"* (talk), Korrelationstage 2013, Dresden.

D. Rauch, M. Kraken, F. J. Litterst, H. Luetkens, M. Brando, M. Baenitz, W. J. Duncan, A. Neubauer, Ch. Pfleiderer, S. Süllow, and F. M. Grosche: *"Microscopic study about the magnetic ground state of C14 systems: $Nb_{1-y}Fe_{2+y}$ and $Ta(Fe_{1-x}V_x)_2$"* (talk), Frühjahrstagung der Deutschen Physikalischen Gesellschaft 2014, Dresden.

D. Rauch, M. Kraken, F. J. Litterst, S. Süllow, F. M. Grosche, M. Baenitz, M. Brando, and G. Kreiner: *"Metallic magnetism of Laves phases $Nb_{1-y}Fe_{2+y}$ and $Ta(Fe_{1-x}V_x)_2$"* (poster), International Conference on Strongly Correlated Electron Systems (SCES) 2014, Grenoble, France.

Abstract

Quantum phase transitions and quantum critical behavior can be observed in magnetically unstable $4f$- and $3d$-electron systems. In contrast to classical phase transitions, which are induced by temperature changes, quantum phase transitions arise as a result of the variation of a non-thermal control parameter e.g. the change of concentration at zero temperature. A great number of complex magnetic ground states are observed close to such quantum phase transitions, which are not fully understood yet. Therefore, we performed stoichiometry studies of $CePt_3B_{1-x}Si_x$, $Nb_{1-y}Fe_{2+y}$ and $Ta(Fe_{1-x}V_x)_2$. During the determination of the magnetic ground state properties of the observed materials studies were performed on a macroscopic scale by measurements of magnetization, resistivity and specific heat and on a microscopic scale by muon spin rotation (μSR) and ^{57}Fe Mössbauer spectroscopy. Combining these different experimental methods has led to comprehensive insights into the static and dynamic magnetic properties and allows the construction of magnetic phase diagrams.

For low silicon concentration, the non-centrosymmetric system $CePt_3B_{1-x}Si_x$ shows physical properties similar to those of $CePt_3B$: an antiferromagnetic ground state and for lower temperatures a weakly ferromagnetic phase. Increasing silicon content leads to a continuous decrease of the antiferromagnetic phase, while the weakly ferromagnetic ordering is completely suppressed for a critical Si concentration $x_c \geq 0.8$. Further, the heavy-fermion system $CePt_3Si$ exhibits an additional unconventional superconducting phase.

Moreover, the magnetic ground state properties of the isostructural C14

Laves phase systems $Nb_{1-y}Fe_{2+y}$ and $Ta(Fe_{1-x}V_x)_2$ are investigated in this thesis. Slight changes in stoichiometry lead to complex magnetic phase diagrams in both systems, with evidence for quantum critical behavior at the transition from a ferromagnetic ordering to a spin density wave ordering. Detailed μSR experiments confirm the rare case of a spin density wave modulated phase in $Nb_{1-y}Fe_{2+y}$, $-0.006 \leq y_c \leq 0.02$, which is surrounded by ferromagnetic phases and a quantum critical point. Furthermore, the magnetic properties are analyzed in μSR experiments close to quantum critical behavior for critical concentrations of $-0.006 \leq y_c \leq -0.015$.

$Ta(Fe_{1-x}V_x)_2$ is also discussed as a system with a spin density wave modulated phase and a ferromagnetic quantum critical point. ^{57}Fe Mössbauer spectroscopy identified a spin density wave modulated state in $Ta(Fe_{1-x}V_x)_2$ for $0.04 \leq x \leq 0.27$ similar to $Nb_{1-y}Fe_{2+y}$. Further, a ferromagnetic instability for $x = 0.02$ in $Ta(Fe_{1-x}V_x)_2$ is observed by means of magnetization studies. This indicates a quantum critical behavior similar to the behavior of $Nb_{1-y}Fe_{2+y}$.

Kurzfassung

Quantenphasenübergänge bzw. quantenkritisches Verhalten wird oft in magnetisch instabilen $4f$- und $3d$-Elektronensystemen beobachtet. Im Gegensatz zu klassischen Phasenübergängen, die bei Änderung der Temperatur auftreten, sind für einen Quantenphasenübergang am absoluten Temperatur-Nullpunkt nicht-thermische Kontrollparameter wie z. B. Konzentrationsänderungen verantwortlich. Nahe solchen Quantenphasenübergängen werden immer mehr komplexe magnetische Grundzustände beobachtet. Um dieses Verhalten besser zu verstehen wurden Konzentrationsstudien an $CePt_3B_{1-x}Si_x$ sowie an $Nb_{1-y}Fe_{2+y}$ und $Ta(Fe_{1-x}V_x)_2$ durchgeführt. Hierzu wurden Experimente auf makroskopischer Skala wie Untersuchungen der Magnetisierung, des elektrischen Widerstands und der spezifischen Wärme, sowie Techniken auf mikroskopischer Skala wie der Myon-Spin-Rotation (μSR) und der ^{57}Fe Mössbauerspektroskopie angewandt. Diese experimentelle Vielfalt liefert umfassende Einblicke in die statischen als auch dynamischen magnetischen Eigenschaften und ermöglicht uns die Erarbeitung der magnetischen Phasendiagramme.

Die magnetischen Grundzustandseigenschaften des nicht-zentrosymmetrischen Systems $CePt_3B_{1-x}Si_x$ ähneln im Bereich geringer Silicium-Konzentrationen denen von $CePt_3B$, welches einen antiferromagnetischen Zustand und für tiefere Temperaturen einen weiteren schwach ferromagnetischen Zustand aufweist. Mit Erhöhung der Si-Konzentration bis zu $CePt_3Si$, einem Schwer-Fermion-System, wird der antiferromagnetische Zustand in Form einer kontinuierlichen Abnahme der Übergangstemperatur geschwächt. Die schwach ferromagnetische Ordnung wird ab einer

kritischen Konzentration $x_c \geq 0,8$ vollständig unterdrückt. Eine vollständige Substitution von Bor durch Silicium führt zu einer zusätzlichen unkonventionellen supraleitenden Phase.

Des Weiteren werden in dieser Arbeit die magnetischen Grundzustandseigenschaften der isostrukturellen C14 Laves Phasen $Nb_{1-y}Fe_{2+y}$ und $Ta(Fe_{1-x}V_x)_2$ untersucht. Bereits geringe Konzentrationsänderungen führen in beiden Systemen zu komplexen Phasendiagrammen mit Hinweisen auf quantenkritisches Verhalten im Übergang von einer ferromagnetischen Phase zu einer modulierten Spindichtewellen-Phase. Für $Nb_{1-y}Fe_{2+y}$ wird im Rahmen dieser Arbeit erstmalig eine modulierte Spindichtewellen-Phase im Bereich von $-0,006 \leq y \leq 0,02$ mittels μSR-Messungen bestätigt, welche von ferromagnetischen Phasen umgeben ist. Zudem werden die magnetischen Eigenschaften in μSR-Messungen für kritische Konzentrationen $-0,006 \leq y_c \leq -0,015$ in der Nähe des quantenkritischen Verhaltens beobachtet.

Ebenfalls diskutiert wird $Ta(Fe_{1-x}V_x)_2$ als ein System mit einem ferromagnetisch quantenkritischen Punkt nahe einer modulierten Spindichtewellen-Phase. Studien der ^{57}Fe Mössbauerspektroskopie identifizieren in $Ta(Fe_{1-x}V_x)_2$ eine modulierte Spindichtewellen-Ordnung ähnlich wie für $Nb_{1-y}Fe_{2+y}$. Weiterhin wird anhand von Magnetisierungsstudien für $x = 0,02$ ferromagnetische Instabilität beobachtet, die in Analogie zu $Nb_{1-y}Fe_{2+y}$ ebenfalls auf solch ein quantenkritisches Verhalten deutet.

Contents

1 Introduction

The rapid development of technology characterizes our daily life, illustrated for example by computer storage media, which are diminishing in size while memory capacities increase. The necessary scientific knowledge for such developments is provided by fundamental research. Especially electronic and magnetic properties of metals are important fields of basic research. In this context, in particular, the search for new materials with unique physical behavior is one of the most important aspects of solid state physics. Identifying new crystal structures and combining such observations with studies of the corresponding characteristic physical properties allows a deep understanding of how new materials may affect physical, chemical or biological processes. Thus, this type of research in solid state physics on experimental and theoretical level can clarify many previously not understood physical properties.

For many decades, in the field of solid state physics, electronic and magnetic correlations caused by interacting electrons in metallic compounds have been explained by the Landau Fermi liquid theory [1–3]. Regarding this issue, Landau found a way to express the complex interactions between electrons by a comparatively simple model of interacting non-scattering quasiparticles, which describes the interaction of ions and electrons as in simple metals. As a result, the existence of well-defined quasiparticles and their excitations with Fermi-Dirac statistics characterizes the electronic properties in very many metals qualitatively as well as quantitatively correct. However, in recent years metallic compounds have been discovered where the validity of the Fermi liquid model is not given. Representative materials are highly correlated electron systems such as

high-temperature superconductors, heavy fermion systems or certain intermetallic d-electron compounds. Over the years it has been found that such intermetallic f- and d-electron metals may exhibit extraordinary physical properties, which are caused by the interaction of localized f- and d-electrons with the conduction electrons. d-electron systems can be localized by discrete bonds between metallic atoms or delocalized over an extended bond system. In contrast, f-electrons usually are localized by the metallic atom which leads to a high magnetic moments in many cases.

Some of these systems exhibit special order phenomena such as unconventional superconductivity and unusual types of magnetic order, which hitherto are not (fully) understood. At present, quantum phase transitions, which arise at absolute zero temperature, are in the focus of investigations. In contrast to typical classical phase transitions like for instance the melting of ice or the vaporization of water, which are caused by thermal fluctuations as a result of heat supply, quantum phase transitions are driven by quantum fluctuations. As these phase transitions occur at the absolute zero temperature, thermal fluctuations do not exist. Instead, quantum fluctuations occur because of the Heisenberg uncertainty principle [4] of quantum mechanics, which implies that even at zero temperature the energy of particles is not absolutely zero. Quantum phase transitions can be driven by non-thermal control parameters like pressure, magnetic fields or chemical composition, and are identified as deviations of temperature dependent thermodynamic properties from Landau Fermi liquid behavior. The strong electronic correlations produce a complex quantum mechanical ground state at the quantum critical point at $T = 0$ K, and also affect the electronic properties in a so-called non-Fermi liquid regime in its vicinity. As by today, quantum critical behavior can not be explained by a single standard model, but depends on various details of the system considered.

Therefore, quantum phase transitions of heavy fermion systems for instance of cerium and ytterbium compounds are examined in detail [5, 6]. Heavy fermion systems e.g. $CePd_2Si_2$ [7], $CeCu_2Si_2$ [8] and $YbRh_2Si_2$ [9] are characterized by an increased effective electron mass,

which is attributed to interactions of the localized $4f$-electrons with electrons of the conduction band. These correlations between the $4f$-electrons and the conduction electrons cause a strongly increased density of states at the Fermi level. At the quantum critical point the magnetic collective excitations become soft and therefore the interaction between the quasiparticles induce a non-Fermi liquid (NFL) behavior [10–12]. In this context the possible occurrence of unconventional superconductivity under suppression of magnetism are explored, e.g. on $CeCu_2Si_2$. Furthermore, in transition-metallic compounds like $ZrZn_2$ [13] and MnSi [14] similar fundamental questions arise about the quantum critical character and its effect on the physical ground state properties of these materials. Latest experiments for instance on MnSi indicate the existence of a non-Fermi liquid phase with partial order and an unusual helical spin arrangement in the magnetically ordered state.

In this thesis studies on various $4f$- and $3d$-electron systems are presented, which were investigated by macroscopic and microscopic measurement techniques, while the non-thermal control parameters chemical concentration and pressure are used to change their physical properties. **Chapter 2** describes – after a brief outline of the Fermi liquid theory – the physical principles of f- and d-electron systems which are important for the understanding of the presented studies. This section is followed by a short introduction into the topic of quantum phase transitions, including a distinction with respect to antiferromagnetic and ferromagnetic quantum critical points.

The main focus of this work lies on the study of local magnetic properties by microscopic experiments. **Chapter 3** presents an overview of the experimental techniques of muon spin relaxation and Mössbauer spectroscopy which were used to investigate local magnetic states of the f-electron system $CePt_3B_{1-x}Si_x$ and the d-electron systems $Nb_{1-y}Fe_{2+y}$ and $Ta(Fe_{1-x}V_x)_2$. Both magnetic resonance techniques provide information on the local environment of the microscopically probing element,

and allow to determine static and dynamic magnetic fields as well as the magnetic moments caused by the electronic interaction with the nuclei.

Chapter 4 examines the non-centrosymmetric system $CePt_3B_{1-x}Si_x$, $0.0 \leq x \leq 1.0$, by means of thermal and transport measurements, via a pressure study up to pressures $p \leq 5.5$ GPa and in μSR spectroscopy experiments. $CePt_3Si$ is the first heavy fermion superconductor ($T_c = 0.75$ K) with a lack of inversion symmetry in the crystallographic structure in coexistence with a long-range antiferromagnetically ordered state ($T_N = 2.2$ K) [15]. The isostructural material $CePt_3B$ undergoes two magnetic transitions at low temperatures, from a paramagnetic state to antiferromagnetic ordering ($T_N = 7.8$ K) and one into a weakly ferromagnetic signature ($T_C \sim 5$ K), and does neither show superconductivity nor heavy fermion behavior [16]. The usage of the control parameter of chemical composition by replacing silicon with boron allows to analyze a possible correlation between the ferromagnetic ground state in one region of the phase diagram and the development of unconventional superconductivity.

Quantum critical behavior has also been discovered in transition metals of the class of Laves phases systems, e.g. in $ZrZn_2$ [13]. Therefore, in the next two chapters two intermetallic d-electron systems belonging to the C14-Laves systems are studied. In **chapter 5** the system $Nb_{1-y}Fe_{2+y}$ is discussed, which has been examined for many years due to its complex magnetic phase diagram containing a number of different magnetic regions: two ferromagnetic regions and a presumed spin density wave modulated state [17–19]. Moreover, at only 1.5% niobium excess a quantum critical point is observed. Microscopic experiments of muon spin relaxation and Mössbauer spectroscopy confirm the magnetic phase diagram, especially the existence of the spin density wave modulated state.

Chapter 6 presents for the first time the properties of the system $Ta(Fe_{2-x}V_x)_2$ studied by Mössbauer spectroscopy. $TaFe_2$ is an isoelectronic Laves system to $NbFe_2$, but with a slightly smaller mean atomic volume ($\sim 13.25\,\text{Å}^3$) than $NbFe_2$ ($\sim 13.35\,\text{Å}^3$). Hence, $TaFe_2$ could be

expected to be closer to a quantum critical point than $NbFe_2$, due to the fact that magnetic properties in $NbFe_2$ can be tuned from a ferromagnetic via a spin density wave modulated state to a quantum critical point by changing the composition within a narrow homogeneity range or by applying hydrostatic pressure [17, 19–21]. Stoichiometric $TaFe_2$ exhibits a paramagnetic ground state, while substitution of iron by vanadium produces an itinerant antiferromagnet in the range of $0.05 \leq x \leq 0.25$. Mössbauer spectroscopy indicates magnetic fluctuations in $Ta(Fe_{2-x}V_x)_2$, which also causes a spin-density wave modulated state as in $Nb_{1-y}Fe_{2+y}$.

Conclusively, **chapter 7** summarizes the results of this thesis and brings an outlook regarding further investigations that might help to resolve the scientific issues discussed here.

2 Theoretical background

A large number of important physical properties of a solid is generated on the basis of a quasi-free electron model. Correspondingly, there are many theories developed in solid state physics to describe the behavior of electrons within the boundaries of this assumption. Here, one of the most important models is the Landau Fermi-liquid theory, which is introduced in this chapter. In addition, the essential theoretical concepts to describe the materials relevant to this thesis, *i.e.*, heavy fermion and Laves phase systems, will be presented in detail. As a last point, the models which are important for the interpretation of the experimentally determined results will be described in the context of non-Fermi-liquid behavior (thus, for cases beyond Fermi-liquid theory) at a quantum critical point.

2.1 Fermi liquid theory of Landau

Conventional metals such as copper or aluminum can be described in terms of non-interacting free electrons. Such electrons are thus only scattered by atomic defects or phonons. Then, free electrons in metals can be described as a Fermi gas within the Drude-Sommerfeld model. This model is valid for an ensemble of electrons, which obey the Fermi-Dirac statistics. These fermions occupy distinct energy levels due to the Pauli exclusion principle, where only one electron (neglecting spin) is allowed per quantum mechanical eigenstate. With the large number of electrons in solids, energy bands are formed which are occupied up to the Fermi energy E_F.
Now, in real materials there will always be (residual) interactions between electrons. The effect may be small for simple metals as a result of the Pauli exclusion principle, the Fermi-Dirac statistics and the free electron

picture. When the density of states at the Fermi energy $N(E_F)$ is high, for instance in the case of narrow energy bands or reduced spatial dimensions, the electron interactions are more important and thus can not be neglected anymore.

In 1957 L. D. Landau developed Fermi liquid theory (LFF) to take account of such electron-electron interactions [1–3], which originally was used to describe the properties of ^{3}He liquids. These days, it has been realized that the theory can be used to explain the ground state properties of various interacting fermionic systems. The basic assumption is that the interaction between fermions can be turned on adiabatically, implying a similar behavior between the single-particle excitations of the non-interacting and those of the interacting systems. Then, the interacting system shows a one-to-one correspondence with the free Fermi gas spectrum for low energies. The excitations, which are called quasiparticles, exhibit the same quantum number (momentum $\boldsymbol{k}$ and spin state σ) as fermions. They still obey the Pauli exclusion principle, but they now obtain an effective mass m^* that is not equal to the mass of free electrons m_e. The effect of interactions with other quasiparticles may be expressed in terms of a Fermi-liquid interaction function $f_{\boldsymbol{k}\sigma,\boldsymbol{k'}\sigma'}$:

$$f_{\boldsymbol{k}\sigma,\boldsymbol{k'}\sigma'} = \frac{1}{2N_0}\sum_{l=0}^{\infty} P_l\left(\widehat{\boldsymbol{k}}\cdot\widehat{\boldsymbol{k'}}\right)\left[F_l^s + F_l^a\sigma\sigma'\right], \tag{2.1}$$

with $\widehat{\boldsymbol{k}} = \boldsymbol{k}/|\boldsymbol{k}|$, $\sigma = \pm 1$, the Legendre polynomials $P_l(x)$, and the dimensionless spin-symmetric F_l^s and spin-antisymmetric F_l^a Landau parameters [22]. The total energy of a system of weakly excited quasiparticle states with respect to various occupation numbers of states is given by

$$E = E_g + \sum_{\boldsymbol{k},\sigma}\epsilon(\boldsymbol{k})\delta n_{\boldsymbol{k}\sigma} + \sum_{\boldsymbol{k}\sigma,\boldsymbol{k'}\sigma'} f_{\boldsymbol{k}\sigma,\boldsymbol{k'}\sigma'}\delta n_{\boldsymbol{k}\sigma}\delta n_{\boldsymbol{k'}\sigma'}, \tag{2.2}$$

with ground state energy E_g and a quasiparticle dispersion $\epsilon(\boldsymbol{k}) \approx \boldsymbol{v_F}(\boldsymbol{k} - \boldsymbol{k_F})$ (Fermi velocity $\boldsymbol{v_F}$, Fermi wave vector $\boldsymbol{k_F}$), which is parametrized by

$\boldsymbol{v_F} = \hbar \boldsymbol{k_F}/m^*$. The last term in Eq. (2.2) incorporates the self-interaction among the quasiparticles, while the first term represents the energy of a single quasiparticle.

The difference between the effective mass m^* and the mass of free electrons m_e due to interaction effects can be calculated from a microscopic theory of the system. Considering a Galilean invariant system where all particles have an additional infinitesimal pulse $\hbar \boldsymbol{q}$ and comparing the changes in energy in Eq. (2.2) of the system and a single particle, we obtain the following relation of m^*:

$$m^* = m_e \left(1 + \frac{F_1^S}{3}\right). \tag{2.3}$$

Thus, in heavy fermion systems m^* can reach values up to $10^3\, m_e$ due to strong interactions. Landau's concept allows to derive the equilibrium thermodynamic properties at low temperatures like the specific heat capacity C and the Pauli susceptibility χ analogous to the considerations in the non-interacting problem. They are given by

$$C|_{T\to 0} = \frac{m^*}{m_e}\gamma T \tag{2.4}$$

$$\chi|_{T\to 0} = \frac{m^*}{m_e}\frac{1}{1+F_0^a}\chi_0. \tag{2.5}$$

The concept of scattering of quasiparticles is limited in its applicability range, mainly due to the lifetime of the quasiparticle. At finite temperatures T quasiparticles in a range of $k_B T$ around the Fermi energy E_F, where $\epsilon(\boldsymbol{k})$ is small, are well-defined. The lifetime of a quasiparticle, $\frac{1}{\tau} \propto (\epsilon(\boldsymbol{k}) - E_F)^2$, increases for wave vectors close to $\boldsymbol{k_F}$ more than the inverse excitation energy. Far from E_F (large $\epsilon(\boldsymbol{k})$) the adiabatic continuity will break down since quasiparticles will decay before interaction can be completely established [22]. In practice, this means that Landau's theory is useful for phenomena at energy scales much smaller than the Fermi energy, but inapplicable otherwise.

For most metals we find that $E_F \approx 3 \ldots 5$ eV according to that they can be described very well by the Fermi-liquid model in the normal state [23]. However, in recent years more and more f- and d-electron systems have been found that show a non-fermi liquid (NFL) behavior as result of a quantum phase transition, which exists close to absolute zero temperature [6]. In this situation, deviations from the Fermi-liquid theory as described above are seen in various physical bulk properties. Up to now, a general model are not existing that allows to describe this type of NFL behavior completely.

2.2 Basics of f-electron systems: Heavy fermion systems

A special class of f-electron systems are intermetallic materials composed of rare earth (Ce, Yb) or actinide (U, Np, Pu) elements. These systems often exhibit a very remarkable physical behavior at low temperatures, which involves partially filled $4f$- or $5f$-electron orbitals. These orbitals are strongly coupled to the conduction electron bands, with the consequence that the interaction between the electrons can not be neglected as in the free electron gas model. As result of the strong electronic interactions heavy fermionic quasiparticles are formed, with effective masses typically of about 100 to 1000 times larger than the mass of free electrons m_e [24] (in the view of the materials band structure, there are narrow electronic bands with a correspondingly strong enhancement of the effective band mass m^*). Because of this observation regarding the effective electron mass, these strongly coupled electron systems are called *heavy fermion systems* (HF).

The strongly enhanced quasiparticle mass m^* can also be understood within a picture of electronic hybridization, which results from the overlap of partially filled and well-localized f-orbitals with itinerant conduction electrons with energies close to the Fermi level. Within this approach, it is seen that heavy fermion systems can have different electronic ground states depending on the competition between the Kondo and Ruderman-

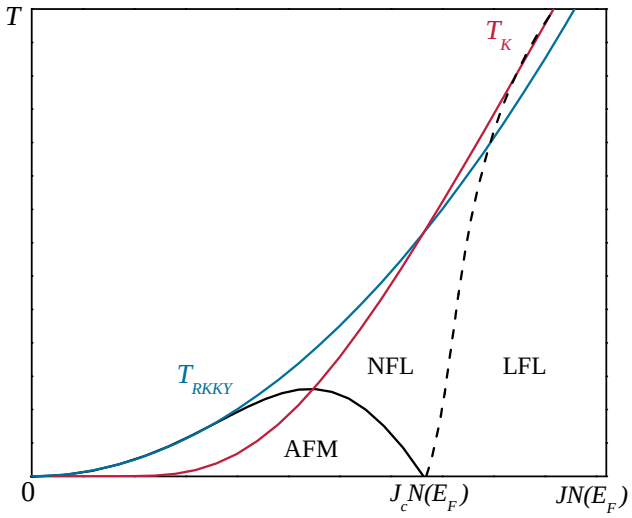

Fig. 2.1: The Doniach phase diagram, illustrating the evolution of the Kondo temperature T_K (red line) and the RKKY coupling temperature T_{RKKY} (blue line) as function of the exchange interaction J between f-electrons and conduction electrons and the density of states at the Fermi level $N(E_F)$ [25, 26]; for details see text.

Kittel-Kasuya-Yosida (RKKY) interaction. This is illustrated in the so-called Doniach diagram [25], see Fig. 2.1.

The essential parameter in this model is the hybridization strength J between localized f- and delocalized conduction electrons. Qualitatively, for relatively weak hybridization ($J < J_C$) an RKKY-mediated antiferromagnetic (AFM) state will form (see section 2.2.2). In contrast, for relatively large hybridization ($J > J_C$) there is a non-magnetic ground state as a result from the Kondo interaction (2.2.1), which can be described by the Landau Fermi liquid (LFL) model. Because of the regular arrangement of Kondo scattering centers, the term "Kondo lattice" has been coined for this state. For an even larger hybridization strength the local f-electron is "absorbed" in the conduction electron band, effectively leading to mixed valence behavior. In the intermediate regime close to a critical hybridization strength J_c, where RKKY- and Kondo interaction

are similar in strength, the antiferromagnetic transition temperature is suppressed to $T_N \to 0$. Thus, there is a quantum critical phase transition (*viz.*, a phase transition happening at $T = 0\,\mathrm{K}$). Associated to this, various new physical phenomena appear such as non-Fermi liquid (NFL) behavior (e.g. $CeCu_{6-x}Au_x$ [27], $YbRh_2Si_2$ [28]) or unconventional superconductivity (e.g. $CeCu_2Si_2$ [8], UPt_3 [5]).

The class of heavy fermion materials is found in the range close to J_c. The enhanced effective mass m^* is reflected in a strongly increased contribution of the electronic specific heat C at low temperatures, which is accounted for a non-magnetic ground state by a term of electronic ($\sim T$) and lattice ($\sim T^3$) contributions:

$$C = \gamma T + AT^3. \tag{2.6}$$

Here, the Sommerfeld parameter γ (within the limit of the free electron model) is proportional to the effective electron mass m^*:

$$\gamma = \frac{\pi^2 k_B^2 N(E_F)}{3} = \frac{k_B^2 \boldsymbol{k_F}^2 m^*}{3\hbar^2}. \tag{2.7}$$

Experimentally, γ is determined by extrapolation of the specific heat $\lim_{T\to 0} \frac{C}{T} \sim N(E_F) \sim m^*$, because the phonon contribution is negligible for $T \to 0$. Historically, this observation of a largely contribution of enhanced electronic specific heat prompted the labeling "heavy fermions" [8].

2.2.1 The Kondo effect

Placing a small number of magnetic ions in the host lattice of a non-magnetic material causes an increase of the electrical resistivity ρ with lowering temperature, a behavior distinctly different to the behavior of the pure metal at low temperatures. This effect has been explained for the first time by J. Kondo [29] in 1964. Conceptually, at high temperatures the electrical resistivity of most metallic materials is dominated by

the electron-phonon scattering. Therefore, upon lowering the temperature the electrical resistivity decreases, since the number of phonons decreases as well. The temperature dependence of the resistivity is controlled by the number of phonons and thus by the temperature factor of the Bose-Einstein statistics. In consequence, the electrical resistivity is proportional to T at temperatures of the order or higher than the Debye temperature Θ_D of the phonons, and proportional to T^5 at temperatures $T \ll \Theta_D$.

In contrast to this simple metallic resistivity, in magnetically diluted metals the scattering of the conduction electrons with the magnetic ions is dominated by a spin-spin interaction below a characteristic temperature. According to the Kondo model, the conduction electrons effectively form a cloud with a spin polarization opposite to that of the local magnetic moment. Thus, the local magnetic moment is screened at low temperatures, resulting in a non-magnetic ground state of the system, *viz.*, the Kondo effect destroys magnetic ordering. The screening electrons enhance the electronic scattering rate by polarization causing the electrical resistivity to increase with decreasing temperature. Experimentally, this is given in a logarithmic temperature dependence of the resistivity with a characteristic minimum. The energy which is required to destroy the Kondo singlet state (the Kondo energy) follows

$$E_K = k_B T_K \propto \frac{1}{N(E_F)} \exp\left(-\frac{1}{JN(E_F)}\right), \tag{2.8}$$

with the Kondo temperature T_K, exchange interaction parameter J and the density of states at the Fermi level $N(E_F)$.

In Kondo systems with small distances between the magnetic atoms (which is achieved for example by increasing the concentration of the magnetic scattering centers) the screening clouds of single magnetic atoms can overlap. If the magnetic ions reside on a translationally invariant sublattice, the clouds become phase coherent below the coherence temperature T_{coh}. Such a state is called a Kondo lattice. Are the Kondo clouds spatially periodic like the lattice in the limit $T \to 0$, they form Bloch like

states which do not contribute to the resistivity, but only to the formation of energy bands with corresponding effective masses. With the large scattering cross section of the clouds the energy bands are flat and m^* is correspondingly very high [30]. Altogether, experimentally as a result of this formation of the Kondo lattice a pronounced maximum in ρ is observed typically at the coherence temperature T_{coh}. Coming from high temperatures, and with decreasing T, the increase of ρ upon approaching T_{coh} reflects incoherent Kondo scattering. With the Kondo lattice forming below T_{coh} the resistivity becomes metallic again. As the dominant scattering process is between electrons, sufficiently far below T_{coh} a temperature dependence

$$\rho = \rho_0 + AT^2 \tag{2.9}$$

is observed, with a constant residual resistivity ρ_0 and a quasiparticle scattering amplitude $A \sim (m^*)^2$ reflecting the mass enhancement of the electrons.

2.2.2 The RKKY interaction

In contrast to well-separated magnetic impurities in a metal (considered in the single ion Kondo problem above), in a HF system the magnetic rare earth ions are arranged on a periodic lattice. Then, the Kondo interaction leading to the screening of the local moments, competes with an interaction between localized magnetic ions due to the polarization of the conduction electrons. This interaction is called the RKKY interaction (abbreviation for Ruderman, Kittel, Kasuya and Yosida [31, 32]).

In the vicinity of a local magnetic moment, its spin polarizes the surrounding conduction electron cloud through the exchange interaction J_{RKKY}. It leads to a damped oscillation of the conduction electron spin polarization, which in turn couples to an adjoining local magnetic moment at a distance r. Thus, via the spin polarization of the conduction electrons and depending on the distance r, the two local magnetic moments are ferro- or antiferromagnetically coupled to each other. The coupling strength is

given by

$$J_{RKKY} \propto \frac{\cos(2\boldsymbol{k_F}r)}{r^3}, \tag{2.10}$$

according to this the spatial oscillation of the spin polarization occurs at a wave length $\pi/\boldsymbol{k_F}$.
As for the Kondo effect, the RKKY interaction gives rise to a characteristic energy scale for magnetic order. This energy scale E_{RKKY} due to the RKKY coupling with the critical temperature T_{RKKY} is defined by

$$E_{RKKY} = k_B T_{RKKY} \propto J^2 N(E_F). \tag{2.11}$$

Now, the exchange interaction J can be controlled by external pressure, chemical substitution or applied magnetic fields. It governs both the coupling strength between magnetic ions as well as between a magnetic ion and the surrounding Kondo screening cloud. Then, within the Doniach model the competition between Kondo effect and the RKKY interaction leads to the HF behavior, the magnetic or non-magnetic ground states, Fermi- or non-Fermi liquid states and the occurrence of quantum phase transitions.

2.2.3 Unconventional superconductivity in heavy fermion compounds

Unconventional superconductivity is observed for various material classes: heavy fermions (e.g. $CeCu_2Si_2$ [8], UPd_2Al_3 [33]), high-temperature superconductors (e.g. $(La,Sr)_2CuO_4$, $YBa_2Cu_3O_7$ [34]) and related oxide materials (e.g. Sr_2RuO_4 [35]), the class of organic superconductors (e.g. $(TMTSF)_2X$, with X = PF_6 or ClO_4 [36, 37]), and most recently the Fe based superconductors (e.g. LaFeOAs [38], FeSe [39]). In contrast to conventional superconductivity as described by Bardeen, Cooper and Schrieffer (BCS theory) [40], in unconventional superconductors the process of Cooper pair formation and/or the symmetry of the superconducting wave function do not adhere to predictions of BCS theory. For conventional superconductivity two electrons with opposite spin form

a Cooper pair with an angular momentum of zero, this is mediated by an electron-phonon coupling mechanism. In consequence, the superconducting state is characterized by an s-wave pair function, which is a spin singlet due to fermion antisymmetry, and an energy gap of the density of states for quasiparticles which are almost independent of the wave vector $\boldsymbol{k}$ of electrons.

In HF systems, the large effective mass of quasiparticles arises from interactions between conduction electrons and localized magnetic moments on the f-orbitals. The magnetic interactions are essential for superconductivity in these compounds, while the electron-phonon coupling is not effective as a pairing mechanism. A heavy quasiparticle, assuming that it has caused a local lattice distortion like in conventional superconductors, can not be removed quickly enough to reduce the Coulomb repulsion with its partner required in BCS theory.

A major difference to the phonon induced pairing mechanism is the vector character of the electron spins and local magnetic moment, which is preferably parallel or antiparallel to the polarized electron spin. In consequence, symmetric or antisymmetric pair wave function of paired electrons generates spin singlet ($\boldsymbol{L} = \text{even}, \boldsymbol{S} = 0$) or spin triplet ($\boldsymbol{L} = \text{uneven}, \boldsymbol{S} = 1$) superconducting states. The pairing interaction is a consequence of the anti-ferromagnetic (spin singlet) or ferromagnetic (spin triplet) spin excitation. In either case it causes the disappearance of the energy gap Δ_0 of the Fermi energy in distinct directions [41–43].

For a long time it was assumed that superconductivity is not possible in magnetic compounds lack inversion symmetry. The discovery of superconductivity in $CeCu_2Si_2$ [8] and other heavy fermion systems in the vicinity of a magnetic instability such as UBe_{13} [45], UPt_3 [5] or $CePd_2Si_2$ [7] was surprising. The low kinetic energy of the heavy quasiparticles are extremely unfavorable to form Cooper pairs. In such systems the magnetism excludes spin singlet coupling because of the lack of time-reversal symmetry, and the crystal structure excludes spin triplet coupling through the absence of inversion symmetry. In these materials a strong

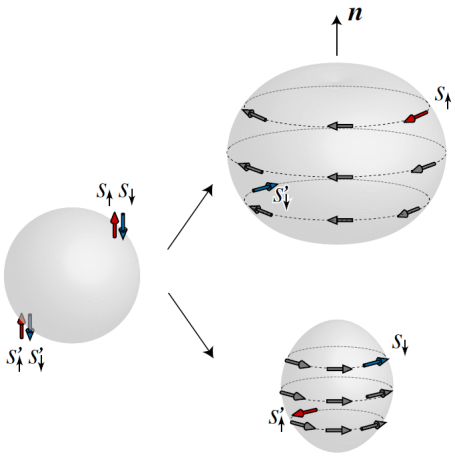

Fig. 2.2: Schematical illustration of the split Fermi surface in non-centrosymmetric materials (from Ref. [44]); for details see text.

spin-orbit coupling leads to an additional splitting of electronic energy bands. Therefore, the Fermi surface splits into two surfaces with an energy separation of $10 - 1000$ K, which are characterized by a different chirality as it is schematically illustrated in Fig. 2.2. These two Fermi surface sheets are different in volume but very similar to each other in terms of their topology, which reflects the antisymmetric spin-orbit interaction arising from the non-centrosymmetric crystal structure. These Fermi surface features give rise to a number of new phenomena with respect to the magnetic and superconducting properties of such materials.

By now, there exists a significant number of established non-centrosymmetric superconductors, which has initiated intensive research on a new aspect of unconventional superconductivity. Several new non-centrosymmetric HF superconductors with unique physical properties have been identified such as $CePt_3Si$ [15], $CeRhSi_3$ [46] and $CeIrSi_3$ [47]. These compounds are antiferromagnetic HF systems, and it is suspected that there is a magnetic coupling mechanism to superconductivity. Further, typical for all of these materials are a competition between superconduc-

tivity and long range magnetic order, with an assumed superconducting order parameter as a mixture of spin singlet and spin triplet configuration, as it is seen for instance in pressure or substitutional experiments [48–51].

2.3 Basics of d-electron systems: Laves phase systems

The Laves phases are one of the most widespread groups of intermetallic compounds named after F. Laves [52]. These phases of a general composition AB_2, where the larger atom A usually stands for $3d$-, $4d$-, $5d$-metals and $4f$-rare-earth elements and the smaller atom B for $3d$-transition metals, are common types of tetrahedrally close-packed structures. So far, more than 1400 binary Laves phases exist [53, 54], which are further categorized into three structural subclasses. The typical structure types are known as the $MgZn_2$ (hexagonal, C14, $Z = 4$ formula units per cell), the $MgCu_2$ (cubic, C15, $Z = 8$) and the $MgNi_2$ type (hexagonal, C36, $Z = 8$), see Fig 2.3. The $MgNi_2$ type is a double hexagonal structure of the C14 phase with the same symmetry, but structurally has been considered a mixture of the $MgZn_2$ and $MgCu_2$ lattices. The crystal structures of the Laves phases contain only two kinds of polyhedra with coordination numbers (CN) of 12 and 16 [55]. The Frank-Kasper polyhedron [57, 58] with CN $= 16$ surrounding the A atoms has 4 six-fold A vertices and 12 five-fold B vertices, whereas the icosahedron (CN $= 12$) surrounding the B atoms has 6 five-fold A and 6 five-fold B vertices (Fig. 2.4). The structural differences between the three Laves phase types arise from the way in which these tetrahedra are connected to each other, while the cavities for the A atoms are always of similar size and shape in each case. Thus, the Laves phases can be understood as a stacking of variants of atom layers in planes perpendicular to the crystallographic c axis.

Laves phases have been studied intensely to understand the fundamental aspects of phase stability and physical properties (e.g. magnetism). Hence, the question about the origin of the homogeneity and the relevance of disorder have to be proven. However, some factors of geometric and elec-

tronic (valence electron concentration and electronegativity difference) nature are helpful to predict stable Laves phases [55, 59]. For geometric reasons, tetrahedrally close-packed structures based on a hard-sphere model are compared to the ideal ratio of radii $(r_A/r_B)_{ideal} = (3/2)^{1/2} \approx 1.225$ [52, 60], which is the major factor controlling the formation of Laves phases. r_A and r_B are the radii of the metal atoms in the ordered phase AB_2. Experimentally it is found that the ratio of radii for the two types of spheres A and B ranges typically from 1.05 to 1.67 and there is obviously no correlation between the size ratio and the structure type that is formed [61]. In addition, the stability of Laves phases also depends on electronic factors. On the one hand there is the difference in electronegativity of a Laves phase AB_2 between atoms A and B, which affect the contraction due to the attractive interaction between the A and B atoms. On the other hand the valence electron concentration plays a major role, which induces a change in the crystal structure. For a number of Mg-based

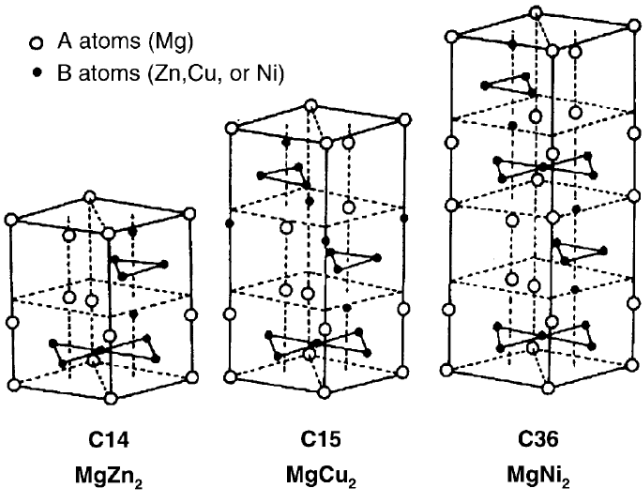

Fig. 2.3: The three Laves phase structure types $MgZn_2$ (C14), $MgCu_2$ (C15) and $MgNi_2$ (C38) (left to right) in a hexagonal setting, as taken from Ref. [55].

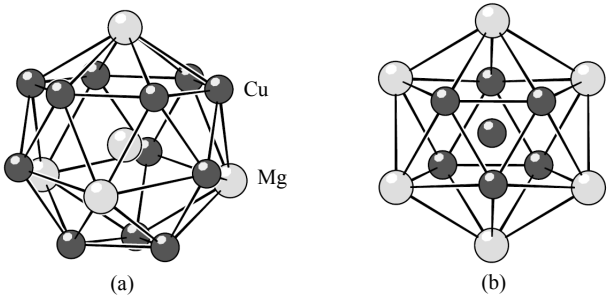

Fig. 2.4: Frank-Kasper polyhedron in $MgCu_2$. The polyhedron with CN $= 16$ surrounding the Mg atoms (a) stretch by 4 six-fold Mg vertices a tetrahedron and by 12 five-fold Cu vertices, forming 4 triangles. The icosahedron around a Cu atom (b) with CN $= 12$ surrounding the Cu atoms has 6 five-fold Mg and 6 five-fold Cu vertices; as taken from Ref. [56].

ternary Laves phases and transition metal Laves phases stable homogeneity ranges of Laves phase structure types are predicted in terms of the number of valence electrons per atom e/a. For example, in Mg-based Laves phases, the C15 phase is stabilized at $e/a < 1.8$, while the C14 phase is stabilized at higher electron concentrations. In transition-element Laves phases, the C15 phase is the most stable structure ($e/a > 2.3$) and the C14 phase is stabilized at very low electron concentrations ($e/a < 0.73$) [55, 62].

Various transition-metal Laves phases (Tab. 2.1) and closely related rare-earth Laves phases (e.g. TbB_2, SmB_2, UB_2) show interesting magnetic properties, which are affected by the stability of the crystal structure [13, 63–66]. The magnetic properties and the crystal structure are both influenced by the A atoms. Considering AFe_2 Laves phase compounds the width of the Fe d-band changes slightly according to the A atom. Depending on the number of the d-electrons of the A atom the lattice spacing decreases and the width of the Fe d-band increases, whereas the d-level of Fe becomes closer to the d-level of the A atom and the mixing between both d-bands becomes strong. This slight variation of the width of the Fe d-band has a strong effect on the magnetism [67]. In the fol-

lowing a brief overview is given about Laves phases of transition metal compounds, which usually exhibit magnetism of itinerant nature carried by the B atoms, while the A atoms are non-magnetic. Among these Laves phases the magnetic compounds of the AFe_2 series possess the most interesting magnetic properties in the C14 and C15 structure, while most of the other compounds are paramagnetic, see Tab. 2.1. C15 cubic compounds like $ZrFe_2$ and $HfFe_2$ exhibit both ferromagnetic behavior with large Curie temperatures and large spontaneous moments [13, 68, 69]. In contrast, members of the C14 hexagonal structure like $TiFe_2$, $NbFe_2$ and $TaFe_2$ [17, 70, 71] present different types of magnetic behavior (antiferromagnetism, spin density wave and paramagnetism with strongly enhanced ferromagnetic fluctuations). In this thesis the focus will lie on the C14 systems $Nb_{1+y}Fe_{2-y}$ and $Ta(Fe_{1-x}V_x)_2$, and subsequently their structural properties will be explained in more detail.

A \ B	Cr	Mn	Fe	Co	Ni
Sc		C14 PM	C14 FM	C15 PM	C15 PM
Ti	C15 - C14 PM	C14 PM	C14 AFM	C15 AFM	
Zr	C15 - C14 PM	C14 PM	C15 FM	C15 PM	C15
Nb	C15 - C14 PM	C14 PM	C14 SDW	C15 PM	
Hf			C15 FM	C15 PM	
Ta	C15 - C14 PM	C14 PM	C14 PM	C15 PM	
Ta		C15 AFM	C15 FM	C15	C15

Tab. 2.1: An overview of crystal structures of $MgZn_2$ (C14) and $MgCu_2$ (C15) type Laves phases AB_2 and their basic magnetic properties (PM – paramagnetic, AFM – antiferromagnetic, FM – ferromagnetic and SDW – spin density wave modulated phase) of transition-metal Laves phase compounds [13, 65, 66].

2.3.1 C14 Laves phases: Structure and magnetism

In the chapters 5 and 6 of this thesis extensive studies of $NbFe_2$ and $TaFe_2$, which belong to the hexagonal C14 Lave phase systems, will be presented. The C14 Laves structure (space group $P6_3/mmc$) has 12 atoms per unit cell. Each Nb or Ta (A) atom is surrounded by 12 nearest neighbors (NN) of Fe (B) atoms and 4 next nearest neighbors (NNN) Nb or Ta atoms. In this case, the Fe atoms on the B sites have two distinct positions within the unit cell labeled Fe($6h$) and Fe($2a$) sites. The Fe($6h$) sites form a planar Kagomé net of equilateral triangles and regular hexagons, while the Fe($2a$) sites lie midway between these planes, so that they form regular tetrahedra, joined at the vertices, with the triangles of the Kagomé net. Each Fe($2a$) atom only arrange every second triangle of the Fe($6h$) Kagomé structure (Fig. 2.5), which leads to different bonding between the pairs of Fe($6h$) atoms in the Kagomé layers. Fig. 2.5 illustrates the crystal structure along the c-axis in combination with the calculated charge density, where color coding is used to distinguish between upper and lower Kagomé layers of Fe($6h$) atoms. According to total-energy calculations, the Fe($2a$) sites draw away the charge density towards the out of plane Fe($2a$)-Fe($6h$) bonds and thus form Kagomé triangles with significant variation of the bonding between Fe($6h$) sites.The interatomic bond distances among the

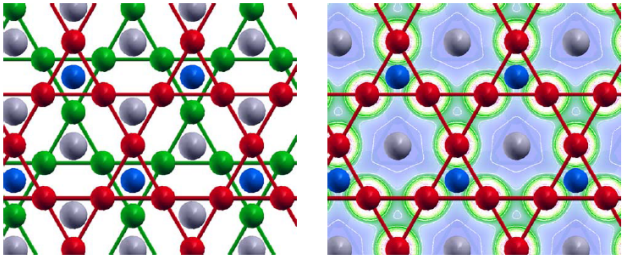

Fig. 2.5: The left figure displays a view of the crystal structure of $NbFe_2$ and $TaFe_2$ along the c-axis with the upper Kagomé layer of Fe($6h$) (red), the lower Kagomé layer of Fe($6h$) (green), Fe($2a$) (blue) and Nb/Ta (gray). In the right figure the charge density contours in the upper Kagomé plane are depicted; as taken from Ref. [19].

Fe sites for stoichiometric $NbFe_2$ are calculated to a distance of 2.42 Å for the sites of Fe($2a$)-Fe($6h$), 2.37 Å for Fe($6h$)-Fe($6h$) and 3.95 Å for Fe($2a$)-Fe($2a$). Significantly, the nearest-neighbor distances from Fe($2a$) and Fe($6h$) sites are similar [19]. However, the Fe atoms on both sites have 6 NN and 6 NNN in an ideal radii ratio of $\sqrt{8/3}$, *i. e.*, the volume available around both sites is nearly the same. Therefore, in an alloyed study, the dopants choice of position in the lattice should not depend on volume effects. Rather, it will be determined by the energetics of the resulting electronic structure. For $NbFe_2$, recent numerical calculations suggest that the Fe($6h$)-site is more favorable for A doping than the Fe($2a$)-site (see Ref. [19]), implying that in such a concentration study an excessive occupation of A atoms will take place within the Kagomé nets.

With respect to magnetic properties, a large number of C14 binary compounds are paramagnets (cf. Tab. 2.1), and only a small number exhibit long-range magnetic order (e.g., $NbFe_2$ [17], $TiFe_2$ [70]). In contrast to C15 structure types the magnetic properties in C14 Laves compounds are reflected in the density of states at the Fermi level of two types of B atoms, the B($2a$) and B($6h$) density of states, whereas in the C15 structure only one kind of B atom contributes. While in most cases the Fe($2a$) sites are believed to be non-magnetic (e.g. $TiFe_2$ [70]), the competition of ferromagnetic and antiferromagnetic ground states of Fe($6h$) Kagomé sites are discussed in the context of strong geometric frustration [72–75]. In the vicinity of a quantum critical point frustrated antiferromagnets on a triangular lattice (e.g. for two dimensional Kagomé structures) have been investigated for many years [76, 77]. Hence, it is speculated that geometric frustration and magnetic instability of the iron moments in Laves phases might go hand in hand. In addition the nature of magnetism can changed as a function of external parameters such as concentration, pressure or temperature with a first order phase transition (e.g. $Hf_{1-x}Ta_xFe_2$ for $x \geq 0.3$ [78]) or a second order phase transition (e.g. $Sc_{1-x}Ti_xFe_2$ for $x > 0.7$ [79]).

2.4 Classical phase transitions

Phase transitions play an essential role in our daily life, most prominently as an example the transformation of water into ice, liquid or vapor. Hence, the understanding of phase transition is of prime importance to physics. In everyday life we observe phase transitions at finite temperatures T, which are driven by thermal fluctuations and are called *classical phase transitions* [80, 81]. Ehrenfest classified these transitions by considering the free enthalpy G of a thermodynamic system [82],

$$G = U - TS, \tag{2.12}$$

with the internal energy U of the microscopic particles, the entropy $S = k_B \ln(\Omega)$, and the microscopic multiplicity of the macroscopic state Ω. Then, the phase transitions are distinguished with respect to their behavior in the partial derivative of $G(T, p, N)$, with the natural variables temperature T, pressure p and particle number N. A phase transition from a phase 1 into a phase 2 is labeled "first order" in the case of a discontinuity in the first derivative $\partial G/\partial(T, p, N)$ of the two phases at the point of transition. For example, the phase transition from liquid to solid at the melting temperature T_c is associated by a latent heat $dQ = T_c dS$. Then, the first derivative is discontinuous with $S = (\partial F/\partial T)_V$.

In contrast, "second-order" transitions exhibit continuity in the first derivatives of G, thus there is no latent heat at the transition. Only for the second derivatives of G there are discontinuities at the transition. Second-order phase transitions are classified as continuous transitions, which are of particular interest since the typical length and time scales of the thermal fluctuations of the characteristic property of the transition diverge at the transition point [83].

As continuous phase transitions are characterized by a divergence of fluctuations, the resulting singularities at the transition point are called critical point. The phase transition can be characterized by an order parameter, a concept formalized for instance by Ginzburg-Landau theory. In the dis-

ordered phase the order parameter is zero in the thermodynamic average, while its fluctuation (*i.e.*, the variations of the average at a distinct time or place) are nonzero. The typical length scale of the fluctuations, the correlation length ξ, increases while approaching the critical point from the disordered side. Close to the critical point it diverges as

$$\xi \propto t^{-\nu}, \tag{2.13}$$

where ν is critical exponent of ξ and t is a dimensionless distance to the critical point. If the transition occurs at a nonzero temperature, t can be defined as $t = |T - T_{coh}|/T_{coh}$. In addition to the correlation in space there are analogous correlations of the order parameter fluctuations in time. The typical time scale for the decay of fluctuations is the correlation time τ_c. Close to the critical point τ_c diverges as

$$\tau_c \propto \xi^z \propto t^{-\nu z}, \tag{2.14}$$

with a dynamical critical exponent z. These divergences are responsible for the different critical phenomena. At the critical point there exist fluctuations on all length and time scales, hence, the system is "scale-invariant". Microscopic details of certain configurations of the system are unimportant due to the large correlation length. In consequence, all physical properties depend via power law functions on external parameters. Then, the critical exponents are identical for entire classes of phase transitions that may occur in different physical systems. Here, the critical exponents are rather dependent on the dimensionality of the system, their interactions, symmetry and distance then on microscopic details [80, 84].

2.5 Quantum critical phase transitions

In recent years a different class of continuous phase transitions, the so-called *quantum critical phase transitions*, have been observed. These transitions occur at zero temperature and are therefore not thermally driven.

Instead, a non-thermal control parameter (e.g., pressure, chemical concentration, magnetic field) is varied to produce the transition from one phase into another. Then, the question about the influence of quantum mechanical effects on such continuous phase transitions arises.

Quantum physics is the essential aspect of such phase transitions. On the one hand, the ordered phases appearing in conjunction with quantum phase transitions can often be only understand by means of quantum mechanics (e.g., in the case of (unconventional) superconductivity). On the other hand, the critical behavior linked to the phase transition is not only affected by thermal fluctuations, but even more so by quantum fluctuations. These different types of fluctuations have to be distinguished by the typical scales of thermal energy $k_B T$ and quantum energy $\hbar\omega_c$, respectively. Approaching the critical point the typical fluctuation time scale τ_c diverges (cf. section 2.4). Correspondingly, the frequency scale ω_c approaches to zero with the typical energy (measured in reduced temperature):

$$\hbar\omega_c \propto \frac{1}{\tau_c} \propto |t|^{\nu z}. \tag{2.15}$$

In consequence, for a phase transition at finite temperatures ($T_{coh} \neq 0$) quantum mechanics become unimportant for $|t| < t_x$ with a crossover distance $t_x \propto T_{coh}^{1/\nu z}$. These thermal fluctuations dominate on a macroscopic scale, while quantum fluctuations can only be relevant on a microscopic scale. Thus at finite temperatures the transitions are called classical phase transitions. In contrast, phase transitions at zero temperature ($T_{coh} = 0$) as a function of a non-thermal control parameter δ (e.g., pressure, concentration etc.) dominate quantum critical fluctuations, since with the crossover distance $t_x = 0$ the condition $|t| < t_x$ is never fulfilled. Thus, a so-called quantum phase transition (QPT) occurs [80, 85].

The competition between thermal and quantum critical fluctuations leads to a schematic phase diagram (Fig. 2.6) close to the quantum critical point (QCP), which is divided into different regions dependent on the dominant type of order parameter or critical fluctuation. At zero temperature the critical control parameter δ_c defines the QCP. In the *quantum disordered*

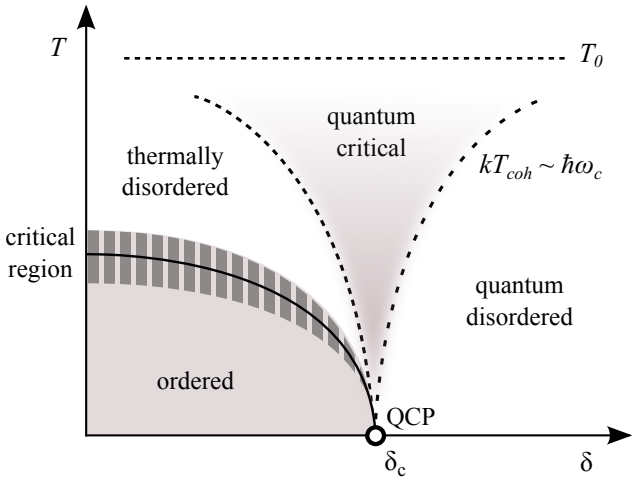

Fig. 2.6: The schematic phase diagram of a material residing in the vicinity of a quantum critical point, as taken from Ref. [84]; for details see text. T_{coh} is a microscopic temperature scale e.g. a Fermi temperature.

region ($\delta > \delta_c$) the dominating quantum fluctuations lead to a Landau-Fermi liquid behavior in metallic systems. In contrast, thermal (classical) fluctuation dominate in the *thermally disordered* region above the long-range ordered phase ($\delta < \delta_c$). The classical critical region close to the phase transition becomes narrower with decreasing temperature. Between the thermally and quantum disordered regions there exists a quantum critical region close to δ_c, where both kinds of fluctuations are important. Here, the behavior is determined by thermal excitations of the quantum critical ground state, $k_B T > \hbar\omega_c \propto |\delta - \delta_c|$, where often non-Fermi liquid behavior, unconventional power laws, etc. prevail. Such universal behavior is only observed close to a QCP, if the correlation length of the quantum fluctuations is significantly larger than the microscopic length scale [6, 10, 80, 85].

The comparison of classical and quantum critical magnetic systems reveals different relations between the static and dynamic magnetic behavior. In quantum critical systems spatial and temporal fluctuations interact,

whereas in purely classical systems both are uncorrelated. This implies a correlation between classical and quantum mechanic behavior. The *effective dimensionality* for a system near a quantum phase transition increases, $d_{eff} = d + z$, with the spatial dimensionality d and dynamical scaling exponent z. In result, this allows a mapping of quantum critical systems to classical phase transitions and by applying d_{eff} provides scaling laws for the characteristic behavior close to a QCP. The identification of the specific nature of a QCP relies on the findings of such scaling behavior in the temperature dependence of thermodynamic and transport properties. Correspondingly, different theories with varying proposed scaling to account for NFL behavior have been put forth by Hertz, Millis, Moriya and Lonzarich [6, 10, 86].

Nowadays, different models of quantum critical behavior exist for heavy fermion systems (e.g. $CeCu_2Si_2$ [8], $YbRh_2Si_2$ [28]) and for itinerant transition-metal magnets (e.g. MnSi [87], $ZrZn_2$ [88]), respectively. Therefore, different kinds of QCPs are distinguished, a ferromagnetic and an antiferromagnetic one. These are considered in more detail in the following sections.

2.5.1 The antiferromagnetic quantum critical point

Antiferromagnetic heavy fermion metals are model systems to study quantum criticality, where the occurrence of QCPs are caused by the competition between local Kondo and non-local RKKY interactions (cf. section 2.2). Studies on the interplay of these two phenomena have revealed different types of antiferromagentic (AFM) QCPs depending on the behavior of the Kondo singlet, *viz.*, the spin density wave (SDW) or Kondo breakdown scenario. The most prominent examples of quantum critical HF metals are $CeCu_{6-x}Au_x$ [89], $YbRh_2Si_2$ [28], $CeCu_2Si_2$ [8] and $CePd_2Si_2$ [90].

The traditional picture described in terms of a SDW state is related to a mean-field type of quantum critical behavior [6, 91]. In this case an antiferromagnetic QCP can be treated as a continuous classical phase tran-

sition in an effective dimensionality of the order-parameter fluctuations $d_{eff} \geq 4$ with $z = 2$ ($z = 3$ for a ferromagnetic QCP). In this scenario, as worked out by Hertz, Millis and Moriya [92–94], the quasiparticles retain the itinerant antiferromagnetic character. These quasiparticles occur at the quantum mechanic disordered LFL region as well as in the magnetically ordered state, where the itinerant antiferromagnetism of conduction electrons is generated by a spontaneous spatial modulation of the spin of the charge carriers [11].

More recently theoretical concepts have noticed that the description of quantum critical fluctuations by an order parameter is insufficient and an additional quantum critical mode has to be emerged. For HF metals these modes are characterized by a critical breakdown of the local Kondo singlets at the $T = 0$ AFM transition [11, 95, 96]. This approach qualitatively differs from the standard theory of a SDW transition, where the screened local moments are assumed to exist at the QCP. This critical destruction of the Kondo effect decouples the conduction electrons from the local f-electrons carrying the magnetic order at the QCP, where the local problem becomes critical. Therefore two kinds of critical degrees of freedom coexist: long-wavelength fluctuations of the order parameter and local fluctuations formed of local moments. This picture leads to a number of distinct properties, e.g., a large reconstruction of the Fermi surface. Across the QCP the Kondo entanglement is destroyed as the system orders magnetically. Thus, the f-electrons contribute to the Fermi surface only in the paramagnetic phase, because of their hybridization with the conduction electrons. In contrast, on the long-range ordered side the f-electrons has a local character and does not contribute to the Fermi surface volume, resulting in a small Fermi surface here [10, 11, 97, 98].

Both QCP types, illustrated in Fig. 2.7, depend on the competition between the Kondo interaction and the AFM RKKY coupling among the local moments at low temperatures. In each case the tuning parameter δ is the ratio of the RKKY interaction to the Kondo temperature. At some critical value $\delta = \delta_c$ an AFM QCP is expected, separating a paramagnetic

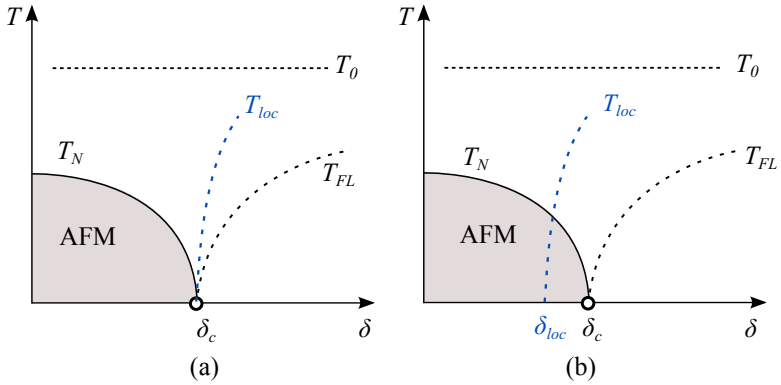

Fig. 2.7: Two schematic types of quantum critical points illustrating (a) a local quantum criticality with critical Kondo destruction and (b) a spin density wave type QCP, where the Kondo breakdown does not occur up to the region of AFM order. T_0 is a crossover temperature scale at which Kondo screening initially sets in Ref. [11, 95].

metal ($\delta < \delta_c$) from an antiferromagnetic metal ($\delta > \delta_c$). Approaching to the magnetic side the strength of the Kondo effect is reduced due to the development of antiferromagnetic correlations among the local moments. Therefore, at a critical value δloc the screening of local moments by the conduction electrons is completely destroyed. Hence, a line associated with the energy scale E_{loc} or temperature scale T_{loc} separates the localized moments carrying the AFM RKKY interaction from the heavy quasiparticles arising from interacting f-electrons and conduction electrons with Kondo interaction (Fig. 2.7(a)). This means that the magnetic ordering transition becomes critical precisely at the same point as the local problem, $\delta_c = \delta_{loc}$. Additionally, T_{loc} marks the crossover from the small Fermi surface regime to the large Fermi surface [11, 95, 97, 99, 100].

In contrast, in the universal class of the SDW type quantum phase transition the energy scale T_{loc} is independent of the magnetic ordering (Fig. 2.7(b)). Here, the quasiparticles arising out of the conduction electrons and local moments are present on both sides of the AFM QCP and form an itinerant magnetically ordered phase in the form of a SDW modu-

lated state. The breakdown of quasiparticles, which changes the character of the magnetic order, are distanced from the quantum critical phase transition, $\delta_c \neq \delta_{loc}$. In this picture, an antiferromagnetically ordered heavy fermion metal arises from an RKKY interaction induced SDW instability of the heavy quasiparticles near their Fermi surface. Likewise, heavy fermion superconductors are considered in terms of the Cooper pairing instability of the same quasiparticles [11, 95, 99, 100].
Si *et al.* [95] proposed that the itinerant SDW picture should be applied for magnetically three-dimensional systems without frustration, while two dimensional spin fluctuations should be described by a locally quantum-critical picture. Experimentally, a suitable method to identify the existence and nature of a QCP in HF systems is to determine the magnetic Grüneisen parameter $\Gamma(T)$ by measuring thermal expansion $\beta(T)$ and specific heat $C_p(T)$, which leads to a divergence of $\Gamma(T)$ at the QCP. The Grüneisen parameter $\Gamma(T)$ is defined as

$$\Gamma(T) \sim \frac{\beta(T)}{C_p(T)} = -\frac{1}{V_{mol}} \frac{(\partial S/\partial p)_r}{T(\partial S/\partial T)_p} \longrightarrow \infty \text{ at QCP}, \tag{2.16}$$

where S is the entropy and V_{mol} the molar volume. Within itinerant theory [101] the Grüneisen parameter at the QCP follows a power law $\Gamma(T) \sim T^{-1/\nu z}$, with the correlation length ν and the dynamic exponent z [11]. For instance, in $CeNi_2Ge_2$ a value $\nu z = 1$ indicates a three dimensional SDW scenario for the QCP, while $YbRh_2Si_2$ possesses $\nu z \sim 0.7$ with an unconventional quantum critical behavior [102].

2.5.2 The ferromagnetic quantum critical point

For a long time a paramagnetic-to-ferromagnetic transition is well-known as a second order phase transition at the Curie temperature T_C, e.g., for the elements Fe, Ni and Co. For materials with high T_C ferromagnetic (FM) transitions are experimentally and theoretically well established. In contrast, recent experimental studies established that for ferromagnetic materials with much lower T_C the transitions into FM phases are of first

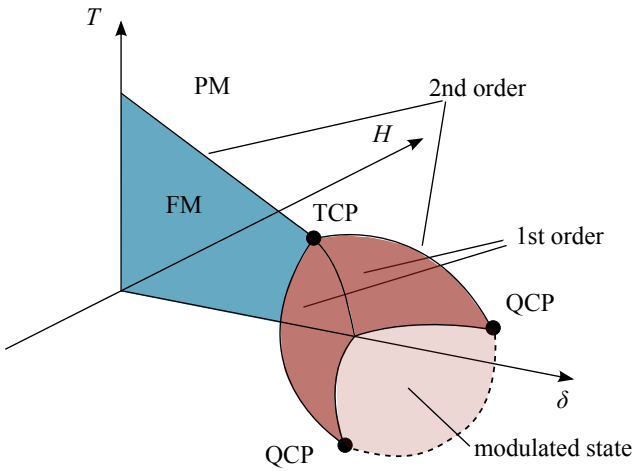

Fig. 2.8: The schematic phase diagram in the vicinity of a ferromagnetic quantum critical point (QCP) with first and second order transition together with the tricritical point (TCP), Ref. [103]; for details see text.

order. In weak itinerant ferromagnets, such as $ZrZn_2$ [88], UGe_2 [104], URhGe [105] and CoS_2 [106], the transition can been tuned to different T_C by applying a non-thermal control parameter δ, e.g. pressure or magnetic fields. Interestingly, at low temperature the FM transition of for instance MnSi, which shows a long-wavelength helical magnetic structure, was found to be of first order, while at higher transition temperatures it is of second order.

A possible explanation of itinerant electron systems at $T = 0$ was developed by Belitz *et al.* [107], which treats the fact that particle-hole excitations are typical for systems with a Fermi surface coupled to the magnetic order parameter fluctuations. Such ferromagnetic (FM) QCPs are generally discontinuous or of first order in the absence of quenched disorder in spatial dimensions $d = 2$ and $d = 3$ [103], in contrast to the Hertz theory for second order transitions [92]. For this reason, FM phase transitions have to be distinguished qualitatively by their Curie temperatures T_C. For rather low values of T_C (*viz.*, close to complete suppression of FM order) first order transitions are found, while at higher T_C values the

transition is of second order (see Fig. 2.8 for a schematic illustration of this observation). Necessarily, the two types of transitions connect at a tricritical point (TCP). By a non-thermal control parameter the second order transition can be suppressed to first order at $T = 0$, if soft modes couple with order parameter fluctuations. At a FM QCP soft modes are fermionic particle-hole excitations that are massless at $T = 0$. With increasing temperature, $T > 0$, the first order transition diminishes and the soft modes acquire a mass. Taking into account an additional small magnetic field H the first order transition splits into magnetic field surfaces or so-called tricritical wings. These wings are bounded by lines of second order and end in a pair of two FM QCPs in the zero temperature plane [86, 103, 107].

In addition to such long-range FM QCPs Belitz *et al.* [103] have shown that this phase diagram also applies for any system with a nonzero homogeneous magnetization, such as metallic ferrimagnets or canted ferromagnets.

Latest theoretical studies identified first order phase transitions with spin modulated phases arising beyond the tricritical points. Here, quantum fluctuations reconstruct the magnetic phase diagram, leading possibly to spiral or nematic phases [108] as schematically indicated in Fig. 2.8 by the area within the dashed line. Experimentally, all these proposed features associated to the FM QCP have not proven yet. In this situation, an important representative itinerant ferromagnetic system with an expected three dimensional FM QCP is $NbFe_2$ [17], which is assumed to undergo a transition into a SDW (*i.e.*, a modulated) magnetic structure at low temperatures.

Various magnetically unstable f- and d-electronic metals are typically located close to AFM/FM quantum critical points. By non-thermal control parameters, e.g. concentration, applied pressure or magnetic fields, a lot of such systems can be driven to quantum critical behavior, which is typically identified by unusual physical properties in the resistivity, magnetism or specific heat. In many cases very low magnetic moments are

responsible for magnetic instabilities as in $CePt_3B_{1-x}Si_x$, $Nb_{1-y}Fe_{2+y}$ and $Ta(Fe_{1-x}V_x)_2$. All three systems show weak FM/AFM fluctuations which are investigated in this thesis regarding their concentration dependency.

3 Experimental methods

For the investigation of (itinerant) magnetism in correlated electron systems, it is essential to carry out experiments at low temperatures. Especially, as set out in the preceding chapter, for systems exhibiting effects, such as quantum fluctuations, close to a quantum critical point it is very important to suppress thermal effects. Therefore, to investigate the physical properties, and in particular the magnetic properties, of - as in the present case - quantum critical alloying systems there are a number of well-established experimental methods. Hence, during the elaboration of this thesis bulk properties of the observed materials such as magnetization, resistivity and specific heat are measured in different cryogenic systems (mostly He^4 and He^3 range) in very high magnetic fields down to low temperatures were studied here [30, 109–114]. Moreover, for specific material cases also the magnetic behavior is studied using high pressure techniques with two different pressure cells and employing a commercial SQUID magnetometer. All these types of experiments have been described in the literature extensively, therefore they will not be covered further in this chapter.

Furthermore, to characterize the static and dynamic magnetic behavior on a microscopic scale of systems close to quantum criticality as function of temperature and/or external fields they can be investigated by different additional experimental techniques such as electron spin resonance ESR, nuclear magnetic resonance NMR, muon spin rotation/relaxation μSR, neutron scattering, as well as Mössbauer spectroscopy [115–122]. Each of these techniques has its own typical experimental measuring time window, which in turn implies that each technique probes a given quantum

critical system in a unique time and energy interval. Combining these different experimental tools, and including the results derived from bulk experimental techniques, yields extensive insights into static and dynamic magnetic properties of the examined materials. In this chapter, two of the microscopic experimental methods performed within this investigation are explained in detail: the muon spin rotation/relaxation μSR and the Mössbauer spectroscopy. Here, the common abbreviation μSR is used for both, the study of *muon spin rotation* and *muon spin relaxation*, as both phenomena are observed throughout the same muon decay process.

3.1 The principles of muon spin rotation spectroscopy

The story of μSR begins with a subtle revolution in theoretical physics. In 1956 and 1957, Lee and Yang predicted that any process governed by the weak nuclear interaction might not have a corresponding "mirror image" process of equal probability [123]. At almost the same time, Garwin, Lederman and Weinrich [124] and Friedman and Telegdi [125] have shown a dramatic effect in the weak interaction decay of pions to muons with a maximal parity violation of pions, generating perfectly spin polarized muons. This was the starting point of μSR spectroscopy. In short, μSR spectroscopy uses muons implanted into a material to probe the magnetic and electronic properties of matter at the microscopic level. As for the other charged leptonic particle/antiparticle pairs, muons exist in two different charge states, the negative muon μ^- and the positive antimuon μ^+. Embedded in a solid state system, the μ^- behaves like an electron, and can even form bound states in the potential of the atomic nuclei. In contrast, the μ^+ are pushed away from the atomic nuclei, and because of the positive charge the antimuon stops on interstitial sites. Here, the muon spin couples to the local magnetic field and performs a precession movement in this field. After a short life time the antimuon decays under emission of a positron in the predominantly direction of its spin orientation. These positrons are detected as function of their direction, and this information is

stored together with the time of the muon decay. In this way, in solid state physics the time and angular dependent spectra of the μ^+ spin relaxation are determined and used.
The following sections (3.1.1 - 3.1.5) provide a short description of the fundamental properties of muons and the principle of μSR experiments with positive muons. Only those aspects which are relevant to this work will be discussed in detail. For an elaborate description of the technique it is referred to the books of A. Schenck [126], G. Schatz and A. Weidinger [116] and the review articles in the Refs. [122, 127, 128].

3.1.1 Production, decay and implantation of the muons

High energy protons, which can be generated in a particle accelerator, interact with protons or neutrons of the nuclei of a given target (e.g. graphite in many experiments) to produce positively charged pions (π^+) via the possible reactions:

$$p + p \longrightarrow p + n + \pi^+ \tag{3.1}$$

$$p + n \longrightarrow n + n + \pi^+. \tag{3.2}$$

The unstable pions decay after a life time of 26 ns into antimuons and muon neutrinos:

$$\pi^+ \longrightarrow \mu^+ + \nu_\mu. \tag{3.3}$$

Since the pion is spinless and the neutrino has a negative helicity $h = -1$, both the neutrino and the μ^+ are ejected with spin anti-parallel to their linear momentum in the pion rest frame. In effect, this allows the production of a nearly 100% spin polarized μ^+-beam. After a mean lifetime of 2.2 μs the antimuon decays in a process according to:

$$\mu^+ \longrightarrow e^+ + \nu_e + \overline{\nu}_\mu. \tag{3.4}$$

Now, the positrons are emitted preferentially along the direction of the μ^+

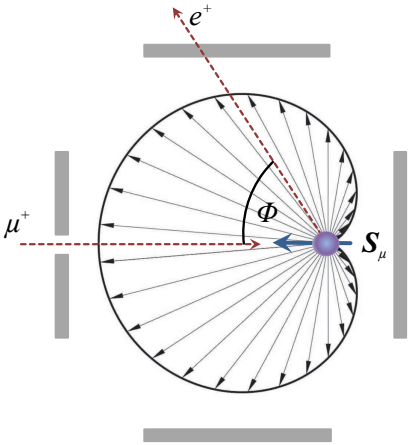

Fig. 3.1: Picture of the angular distribution of positrons emitted via muon decay with the asymmetry parameter $A = 1/3$ as a result of integration over all positron energies, relative to the surrounding detector banks drawn schematically.

spins in the moment of the decay due to this parity violating decay. In turn, by measuring the direction of positron emission it allows a determination of the spin polarization of a μ^+ ensemble at the time of decay, and therefore to investigate the time evolution of the muon spin polarization.

The energy of the emitted positrons varies continuously between zero and 52.83 MeV, depending on the angles ϕ between the momentum vectors. The anisotropy of the direction of the positron emission probability with respect to the muon spin at the decay time is given by

$$W(\phi) = 1 + A\cos(\phi), \tag{3.5}$$

with the angle ϕ between the μ^+ spin direction $\boldsymbol{S}_\mu$ and the positron momentum $\boldsymbol{p}_{e^+}$. The asymmetry parameter A depends on the polarization of the muon beam and the energy of the emitted positron. For a maximal positron energy it is found that $A = 1$, while for integration over all positron energies it is $A = 1/3$, cf. Fig. 3.1. Accordingly, on average

the positrons are predominantly emitted in the direction of the μ^+ spin. For reference, the important properties of the μ^+ for the use in solid state physics are listed in Tab. 4.1.

mass m_μ	$206.769\, m_e \sim 1.88 \cdot 10^{-28}$ kg
charge	+e
spin S_μ	1/2
magnetic moment μ_μ	$3.18\, \mu_p$
average life time $\tau_\mu = t_{1/2} ln 2$	$2.197 \cdot 10^{-6}$ s
gyromagnetic ratio γ_μ	$2\pi \cdot 135.54$ MHz/T

Tab. 3.1: Main physical properties of the positive muon μ^+, with the values taken from the Refs. [116, 126]. μ_p labels the magnetic moment of a proton.

Experimentally, the muons are implanted into the sample of interest, where they lose their energy very quickly and come to rest. This way, the μ^+ penetrates a few μm to mm into the sample and stops generally at interstitial sites. This process takes place within $10^{-10} - 10^{-9}$ s. Then, an influence of the local fields, that are passed by the muon on its way through the sample can be neglected. Further, the sample is located in a cryostat and is surrounded by the positron detectors and Helmholtz coils for generating an external field (see section 3.1.3).

3.1.2 Technique of the μSR measurement

As soon as the muon is located at the interstitial site, the muon spin $\boldsymbol{S}_\mu$ precesses in the local magnetic field B with a Larmor frequency ω_μ given by

$$\omega_\mu = \gamma_\mu B, \tag{3.6}$$

where γ_μ is the gyromagnetic ratio for the muon (cf. Tab 4.1). If the implanted μ^+ are subject to magnetic interactions, their polarization becomes time dependent, $\boldsymbol{P}_\mu(t)$. The time evolution of $\boldsymbol{P}_\mu(t)$ can be deduced by measuring the angular positron distribution as a function of time. A schematic setup of a μSR spectrometer for such an experiment is shown in Fig. 3.3. As the positron is emitted after the decay of the muon along

the axis of its spin, several detectors are placed around the sample in order to register the positron. Usually there are six positron detectors, which are named according to their position (Backward, Forward, Right, Left, Up and Down).

In the time-differential μSR technique, repeated measurements ($\sim 10^7$) are made of the time interval between the μ^+-implantation into the sample and the detection of the emitted positron in a particular direction. The μSR histogram (Fig. 3.2(a)) shows the corresponding signal oscillation as a result of the spin precession, together with the exponential decay. The histogram of positron counts $N(t)$ for each detector are given by:

$$N_{e^+}(t) = N_{backgr} + N_0 \exp(-t/\tau_\mu) \left[1 + A\, G(t)\right], \tag{3.7}$$

where N_{backgr} is a time-independent background (e.g., mostly from an Ag plate which serves as sample holder), N_0 is a normalization constant and the exponential function accounts for the time distribution of μ^+ decay times with average τ_μ. Further, $G(t)$ describes the time dependence of the μ^+-polarization $P_\mu(t)$, which can be identified as the projection of $\boldsymbol{P}_\mu(t)$ along the direction of the initial polarization $\boldsymbol{P}_\mu(0)$, i.e., $P_\mu(t) = \boldsymbol{P}_\mu(t) \cdot \boldsymbol{P}_\mu(0)/P_\mu(0) = G(t)P_\mu(0)$. $G(t)$ reflects the normalized μ^+-spin auto-correlation function

$$G(t) = \frac{\langle \boldsymbol{S}_\mu(t) \cdot \boldsymbol{S}_\mu(0) \rangle}{\boldsymbol{S}_\mu(0)^2}, \tag{3.8}$$

which depends on the average value, distribution, and time evolution of the internal magnetic fields and therefore contains all the physics of the magnetic interaction of the μ^+ inside the sample. The time evolution of the muon spin polarization $\boldsymbol{P}_\mu(t)$ is given by the classical Bloch equation:

$$\frac{d\boldsymbol{P}_\mu(t)}{dt} = \gamma_\mu \boldsymbol{P}_\mu(t) \times \boldsymbol{B}, \tag{3.9}$$

which describes the Larmor precession of $\boldsymbol{P}_\mu(t)$ around $\boldsymbol{B}$. The local magnetic field $\boldsymbol{B}$ is the superposition of an internal field $\boldsymbol{B}_{int}$ and a possi-

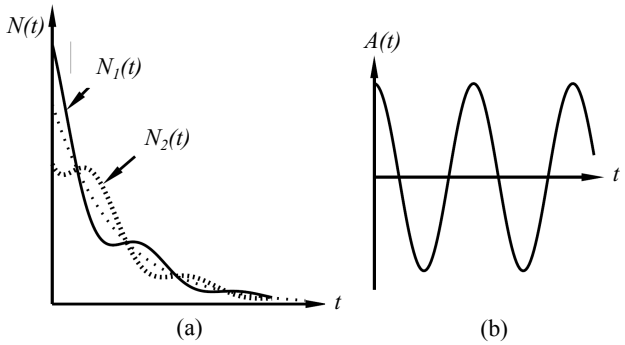

Fig. 3.2: Schematic illustration of (a) the number of positrons detected in the forward $N_2(t)$ and backward $N_1(t)$ detectors and (b) the resulting asymmetry function $A(t)$ in μSR experiments [122].

ble external applied magnetic field $\boldsymbol{B}_{ext}$. Internal fields can originate from dipolar fields $\boldsymbol{B}_{dip}$ of localized magnetic moments acting on the μ^+ spin and from the Fermi contact interaction $\boldsymbol{B}_{Fermi}$ of polarized conduction electrons with μ^+. In addition, the demagnetization $\boldsymbol{B}_{dem}$ and Lorentz $\boldsymbol{B}_L$ fields, which can be calculated from the bulk magnetization and demagnetization tensor need to be taken into account (see Ref. [126]):

$$\boldsymbol{B} = \boldsymbol{B}_{ext} + \boldsymbol{B}_{dip} + \boldsymbol{B}_{Fermi} + \boldsymbol{B}_{dem} + \boldsymbol{B}_L. \tag{3.10}$$

$\boldsymbol{B}_L$ originate from macroscopic magnetization of the investigated sample contribution to the local magnetic field.

The depiction, as shown in Fig. 3.2(b), of the product $A\,G(t)$ versus t is often called μSR signal or asymmetry spectrum with an envelope of $G(t)$. Therefore, two raw data sets $N(t)$ of opposite detectors 1 and 2 are used to derive the asymmetry spectrum:

$$A\,G(t) = \frac{N_1(t) - \alpha N_2(t)}{N_1(t) + \alpha N_2(t)}. \tag{3.11}$$

This way, the background noise and the exponential decay of the spectra are averaged, and only the information, which is relevant for the evaluation

of magnetic signal component of the spectra, is derived. Experimentally, in general the efficiency of the different detectors differs and we have to use a coefficient α to compensate this, usually α is close to 1. The exact value can be determined by fitting the data in transverse field μSR, where the relaxation is distinctly shorter than the time window [129]. Thus, the final spectrum is composed of the initial asymmetry, that remains the same for all further measurements with a given detector constellation and the time evolution of the polarization of the muon spins:

$$A(t) = AG(t). \tag{3.12}$$

Both quantities $A(t)$ and $G(t)$ contain now all the information about the interaction of the muon with its environment and thus the interesting physical aspects of the system studied. In an idealized case the asymmetry parameter is $A = 1/3$ (see Eq. (3.5)), while in praxis values of $A \cong 0.20 - 0.25$ are obtained.

In the case of static local magnetic fields $\boldsymbol{B}$ at the μ^+-site, $G(t)$ is given by

$$G(t) = \int f(\boldsymbol{B}) \left[\cos^2(\phi) + \sin^2(\phi) cos(\gamma_\mu \boldsymbol{B} t)\right] d\boldsymbol{B}, \tag{3.13}$$

where $f(\boldsymbol{B})$ is the magnetic field distribution, ϕ the angle between the local field $\boldsymbol{B}$ ($B = |\boldsymbol{B}|$) and the initial polarization $\boldsymbol{P}_\mu(0)$. The expression within the square brackets describes the Larmor precession with frequency $\omega = \gamma_\mu B$ of the μ^+ spin along the field direction. Only the component of the μ^+ spin perpendicular to the internal field ($sin^2(\phi)$) precesses.

The possible presence of different magnetic environments, i.e., different μ^+-stopping sites or domains with different types of ground states, may be identified by different components in the spin auto-correlation functions

$$G(t) = \sum_i a_i G_i(t). \tag{3.14}$$

Since the μ^+ are uniformly implanted in the sample, the amplitudes a_i

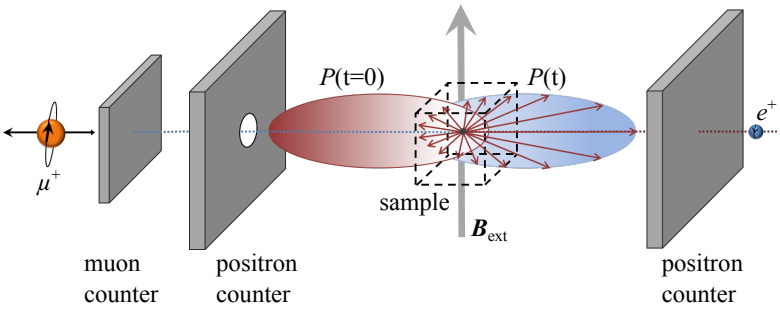

Fig. 3.3: Schematic illustration of the μSR technique with the example of a setup for a transverse field experiment; for a detailed description see text and Ref. [126].

($\sum_i a_i = A$) of the associated volume fractions of different domains are measured.

All measurements presented in this work were performed at the Paul Scherrer Institute (PSI), Villigen, Switzerland. Here, the time-differential (TD) μSR with a continuous muon beam is used. For the time measurement, a "clock" starts when the first detector in Fig. 3.3 (the muon counter) is passed by the muon, and stops in one of the detectors after decay of the muon. Also, if two decay events are registered after one entrance event these will be discarded.

In the present work we are mainly interested in the determination of magnetic hyperfine fields at the muon site. These fields are either produced by magnetic moments within the investigated compound or by externally applied magnetic fields. In weak transverse fields, zero fields and longitudinal fields μSR experiments are used to study the magnetic behavior, subsequently these experimental approaches will be introduced.

3.1.3 Weak transverse field μSR measurements

In a weak transverse field (wTF) experiment a magnetic field (of the order of 10 mT) is applied perpendicular to the initial muon polarization $\boldsymbol{P}_\mu$

(i.e. with a muon spin in z-direction). Then, for all muon spins a magnetic field component perpendicular to their orientation exists, even if the internal field is parallel to the muon spins. For a specific material, wTF measurements are mostly used in non-magnetic regimes, i.e. in paramagnetic states. In contrast, for magnetically ordered phases $\boldsymbol{B}_{int}$ is typically much smaller than $\boldsymbol{B}_{ext}$, and thus zero field measurements are more suitable (see section 3.1.4). Hence, in the paramagnetic state the depolarization function $G(t)$ can be analyzed with simple mathematical models (for e.g. damped harmonic oscillation).

Since in wTF experiments, the external magnetic fields are usually much larger than any internal fields, only the field inhomogeneity along the direction of $\boldsymbol{B}_{ext}$, i.e. along the x-axis, has to be considered ($\boldsymbol{B}_{ext} >> \sigma/\gamma_\mu$). In this case Eq. (3.13) can be simplified and leads typically to two different models depending on the magnetic field distribution. For an inhomogeneous field distribution caused by static nuclear or electronic dipole fields, the muons located at different sites detect as well slightly different fields. Such isotropic field distribution results in a loss of polarization by dephasing of the muons, corresponding in a Gaussian distribution with a damping cosine signal:

$$G_x(t) = \exp(-\frac{1}{2}\sigma^2 t^2)\cos(\omega_\mu t + \phi), \tag{3.15}$$

where $\sigma^2 = \gamma_\mu^2 M_2$, with the second moment M_2 of the corresponding field distribution along the direction of $\boldsymbol{B}_{ext}$, the frequency ω_μ of the local field at μ^+ and the phase shift ϕ. If the field distribution is caused by nuclear dipole fields, M_2 can be easily calculated and will usually depend on the direction of $\boldsymbol{B}_{ext}$. Hence, the comparison of the angular dependence of the observed depolarization rate σ with the calculated M_2 will provide an additional test for the determination of the μ^+ site [127].

Analogously, homogeneous field distribution caused by fluctuating internal fields leads to an exponential loss of polarization of the precessing

muon spins. The depolarization function is given by:

$$G_x(t) = \exp(-\lambda_x t)\cos(\omega_\mu t + \phi), \tag{3.16}$$

where the damping rate $\lambda_x = \sigma^2/\nu$ is the half width at half maximum of the Lorentzian distribution function and ν the single fluctuation rate [128]. In particular, further TF experiments are suitable, i.e., for investigations of magnetic field distributions in type II superconductors or Knight shifts $K = -\Delta B/B_{ext}$. However these are no subjects in this thesis.

3.1.4 Zero field μSR measurements

Zero field (ZF) μSR is a very sensitive method to detect internal magnetic fields, which are either of electronic origin or caused by nuclear magnetic moments of the host lattice atoms. The local magnetic fields stem either from ordered magnetic moments within the sample, or there are random fields that are static or fluctuating with time. The large magnetic moment of the muon ($\mu_\mu = 8.9\,\mu_N$with the magnetic moment μ_N of a neutron) makes the μSR sensitive for extremely small internal magnetic fields e.g. due to nuclear dipoles.

Static fields

Static magnetic fields are caused by magnetic order in a given material. Here, the muon spin autocorrelation function $G(t)$ depends sensitively on the details of the magnetic structure and on the interstitial positions of the muon. In the simplest case an ordered arrangement of magnetic moments produces a local hyperfine field of well-defined magnitude $\boldsymbol{B}$ and direction at the μ^+ site. If there is an angle ϕ between $\boldsymbol{B}$ and the initial muon-spin direction, the muon spin will precess around a cone of a semi-angle ϕ at the local magnetic field. For a single-domain mono-crystalline sample with a well-defined internal magnetic field B. The magnetic field distribution $f(B)$ is corresponding to a δ-function and simplifies Eq. (3.13). Hence,

$G(t)$ is given by

$$G(t) = \cos^2(\phi) + \sin^2(\phi)\cos(\omega_\mu t), \tag{3.17}$$

with the Larmor frequency $\omega_\mu = \gamma_\mu B$, where $B = |\boldsymbol{B}|$.

Further, for the case of zero applied magnetic field it is not ensured that all muons implanted into the sample are influenced by a magnetic field component perpendicular to their spin, for instance because of multiple domains or in case of a polycrystalline sample. Then, on average, $1/3$ of all muon spins are parallel to the local internal fields and do not precess along the field direction (cf. Eq. (3.5) and Fig. 3.1). In this case the μSR spectra present oscillation of about $1/3$ corresponding to the internal magnetic field at μ^+ site. Hence, for polycrystalline structures an average of the angular dependence yields

$$G(t) = \frac{1}{3} + \frac{2}{3}\cos(\omega_\mu t + \phi). \tag{3.18}$$

The second term represents the spontaneous μ^+ Larmor precession in the internal field. The precession signal becomes only maximal for $\boldsymbol{B} \perp \boldsymbol{P}_\mu$.

For real materials the situation is often even more complicated, thus certain field distributions are considered. Such distributions may arise from disorder, dynamic behavior or additional internal fields as for instance from static nuclear or electronic dipole fields. In that case, a more complex time evolution of the depolarization function $G(t)$ is generated.

Due to nuclear magnetic moments or to randomly frozen electronic spins the strength of the local internal magnetic field is depended from a Gaussian distribution of width Δ/γ_μ. Hence, the field distribution is centered around zero and no spontaneous frequency is observed. $G_{KT}(t)$ is given by the static Kubo-Toyabe function:

$$G_{KT}(t) = \frac{1}{3} + \frac{2}{3}\left(1 - \Delta^2 t^2\right)\exp(-\frac{1}{2}\Delta^2 t^2). \tag{3.19}$$

where the width Δ^2/γ_μ^2 represents the second moment of the local field

distribution at the muon site. Such a depolarization function is characteristic for a paramagnetic state where the muon depolarization is only depending on the dipolar fields from the nuclear moments which appear randomly oriented and static within the μ^+ lifetime. The origin of the function shows two characteristics, first $G_{KT}(t)$ decrease from unity to a minimum with $G_{KT}(t) \cong \exp(-\Delta^2 t^2)$ at the beginning times ($t << \Delta^{-1}$) and then recover to an average value of one-third after a short relaxation time.

In another case, a material with an incommensurate magnetic structure (described by one $\boldsymbol{q}$ wavevector) exhibits a sinusoidal distribution of the internal field, given by a strongly damped oscillation of the Bessel function j_0 [127, 130–132]:

$$G_{Bssl}(t) = \frac{1}{3} + \frac{2}{3} j_0 \left(\omega_{\mu,max} t + \phi\right), \tag{3.20}$$

where $\omega_{\mu,max} = \gamma_\mu B_{max}$ represents the cutoff field of the local field distribution at the μ^+ site. Therefore, incommensurate spin modulation structures are well described by $G_{Bssl}(t)$ (e.g. UNi_2Al_3, $CeCu_{6-x}Au_x$ [127]). Again the $1/3$ term of the magnetic component is caused by the fraction of the muon ensemble for which the static internal field at the μ^+ site is parallel to the initial μ^+ polarization. The term containing the Bessel function describes the muons precessing in a modulated internal field. In contrast, commensurate magnetic structures reveal a sharp local-field distribution at the μ^+ site.

Fluctuating fields

The μSR spectra taken in non-magnetic regimes are determined by dynamics caused by the fluctuations of magnetic moments producing the local magnetic fields and eventually in addition by muon diffusion. The latter phenomenon is of no relevance to the experiments presented here and therefore is not considered further.

For the analysis of magnetic fluctuations, first of all it is to be noted that electronic and nuclear moments fluctuate on rather different time scales

(ν_{spin}; ν_{nuc}). Commonly, at high temperatures, in non-magnetic regions, the fluctuations of electronic dipolar moments are very fast with the effect that the fields they produce at the muon site are negligible on average.

In the following the most common case of time dependence of the Gaussian distribution of internal fields are discussed. In fluctuating fields the static Kubo-Toyabe function $G_{KT}(t)$ of the Gaussian distribution (for disordered quasi static nuclear moments) is modified to the so called dynamical Kubo-Toyabe function $G_{KT}^{dyn}(t)$ to account for fluctuations from electronic spins in magnetically disordered regions, which with the exception of some limiting cases, cannot be expressed analytically. Numerical results for $G_{KT}^{dyn}(t)$ are available in form of tables that are automatically used for fittings of experimental data. Nevertheless using for calculating of the strong collisions model [129] implies that every fluctuation destroys the correlation between the field distribution before and after the event completely. However, for different approximations of fluctuation $G_{KT}^{dyn}(t)$ can be specified. For fast fluctuations ($\nu/\Delta >> 1$) muons interact with the spin fluctuations and the depolarization function is characterized by a weak decreasing exponential function:

$$G_{fast}(t) = \exp(-2\Delta^2 t/\nu) \equiv \exp(-\lambda t), \tag{3.21}$$

where ν characterize the fluctuation rate. The depolarization rate describes the spin-lattice relaxation ($2\Delta^2/\nu = \lambda$) and involves spin-flip transitions induced by the fluctuating magnetic fields with components perpendicular to $\boldsymbol{P}_\mu(0)$.

On the other hand, in the case of $T \to 0$ slow fluctuations ($\nu/\Delta << 1$) are given by the static Kubo-Toyabe function $G_{KT}(t)$ with an additional damping in the $1/3$ term at longer times:

$$G(t) = \frac{1}{3}\exp(-\frac{2}{3}\nu t) + \frac{2}{3}(1-\Delta^2 t^2)\exp(-\frac{1}{2}\Delta^2 t^2). \tag{3.22}$$

In contrast, for the analysis of magnetic fluctuations ($T \to T_C$) slow fluctuations lead to a oscillation (not symmetrical) in the μSR spectra around

$1/3$ with an additional damping of the signal, given by

$$G_{mag}(t) = \frac{1}{3}\exp(-\lambda_L t) + \frac{2}{3}\cos(\omega_\mu t + \phi)\exp(-\lambda_T t), \qquad (3.23)$$

with a longitudinal damping λ_L, which describes the dynamics of magnetic moments in the muon region, and a transversal damping λ_T, which comes from the dynamics of neighbor moments and the field distribution of the μ^+ site of local disorder in the long-range magnetic order. Thus applies: $\lambda_L \sim \nu_{spin}$ and $\lambda_T >> \lambda_L$. Therefore, a very small λ_T indicates static magnetic order.

3.1.5 Longitudinal field μSR measurements

Muon depolarization can arise from either static or fluctuating field distributions, because of some intrinsic properties of the sample, of the μ^+ position, or of muon diffusion. In zero field μSR experiments it is not possible to distinguish between these possibilities. However, this can be accomplished by a set-up of longitudinal field (LF) μSR measurements, applying external fields $\boldsymbol{B}_{\mathrm{LF}}$ parallel to the initial muon spin polarization $\boldsymbol{P}_\mu(0)$. By choosing $\boldsymbol{B}_{\mathrm{LF}}$ to be much stronger than internal fields ($\gamma_\mu B_{LF}/\Delta >> 1$) some decoupling of the μ^+ spins from the randomly oriented internal static fields occurs, i.e. any static distribution of the internal fields will not affect the time evolution of the μ^+-polarization. For internal fields that are Gaussian distributed, the depolarization function $G^{stat}_{KT,LF}(t, B_{LF})$ [129] as function of an applied field is given by

$$\begin{aligned} G^{stat}_{KT,LF}(t, B_{LF}) &= 1 - \frac{2\Delta^2}{\gamma_\mu^2 B_{LF}^2}\left[1 - \exp(-\frac{1}{2}\Delta^2 t^2)\cos(\gamma_\mu B_{LF} t)\right] \\ &\quad + \frac{2\Delta^4}{\gamma_\mu^3 B_{LF}^3}\int_0^t \exp(-\frac{1}{2}\Delta^2\tau^2)\sin(\gamma_\mu B_{LF}\tau)d\tau, \end{aligned} \qquad (3.24)$$

where the width Δ represents the Gaussian field distribution and ν the fluctuating rate. It has to be considered that this calculation assumes that

the external field does not reorient the dipoles which give rise to the internal fields at the μ^+ sites. For strong B_{LF} the depolarization function vanishes, i.e. $G^{stat}_{KT,LF}$ stays constant at ~ 1. Analogous to the very fast dynamics, the muon spin does not precess and remains in its μ^+ implantation position. In analogous form the Lorentzian function describes the field distribution for dilute dipole moments, whilst Gaussian field distributions are applicable for concentrated dipole moments.

Internal field dynamics, resulting either from the muon hopping (with a hopping rate Γ) between different interstitial sites or from internal fluctuating fields, can be accounted within the strong collision approximation [129]. Assuming that the local field changes its direction at a time t and that the internal field after such a "collision" is chosen randomly from the distribution and is entirely uncorrelated with the field before the collision distribution. Hence, the total muon polarization is a superposition of the polarization function $g^{(n)}(t)$ of each muon under consideration of the experienced field change at time t, given by:

$$\begin{aligned} G^{dyn}_{KT,LF}(t) &= \sum_{0}^{\infty} g^{(n)}(t) \\ &= g^{(0)}(t) + \sum_{0} \infty\nu \int_0^t g^{(n-1)}(t-t')g^{(0)}(t')dt' \\ &= g^{(0)}(t) + \nu \int_0^t G^{dyn}_{KT}(t-t')g^{(0)}(t')dt' \end{aligned} \tag{3.25}$$

where $g^{(0)}(t) = g(t)\exp(-\nu t)$ characterizes the field distribution without an experienced field change at time t. This expression can be evaluated by numerical integration for any internal field distribution (i.e. Gaussian or Lorentzian) with an applied external field similar to the one observed in zero field (Eqs. (3.21)-(3.23)). For fast fluctuations of the internal fields, i.e., in the spin-lattice relaxation regime, induced irreversible spin-flip transitions will lead to a depolarization with $\lambda = (2\Delta^2/\nu)/(1 + (\gamma_\mu B_{LF}/\nu)^2)$ [127, 129, 133, 134].

Hence, using LF μSR, the dynamic contributions to the internal fields can

be separated from static sources and is approached in different cases in dependence of the correlation time.

3.2 Mössbauer spectroscopy

In 1957, Rudolf L. Mößbauer discovered the recoilless nuclear resonance absorption and emission of γ-quanta [135]. After its discoverer this effect is called the *Mössbauer effect*. Nowadays, the experimental technique developed to utilize this effect, the Mössbauer spectroscopy, is one of the most sensitive nondestructive techniques for analyzing the chemical bonding, hyperfine magnetic splitting and local crystallographic symmetry of a probe nuclei embedded in a solid state material.

The Mössbauer effect can be observed in an experimental arrangement of specific γ-rays directed onto an absorber material, with a γ-detector either in transmission or reflection to measure the absorption signal. For the specific case of ^{57}Fe Mössbauer spectroscopy ^{57}Co serves as γ-ray source. (The amount of the isotop ^{57}Fe in natural iron is only about $2\,\%$.) In the formed radioactive decay of the nuclide ^{57}Co the excited state of the Mössbauer nucleus ^{57}Fe is formed after electron capture from the atomic shell. The ^{57}Fe nucleus, under transition from the excited state $(3/2)^-$ into the ground state $(1/2)^-$, emits a γ-quantum with an energy of 14.4 keV and a life time $\tau = 98$ ns. To adjust for resonance absorption in the absorber, the energy of the γ-quantum emitted at the source is controlled by moving source and absorber with respect to each other, this way making use of the γ-quantum energy shift via Doppler effect. The γ-radiation passing the absorber is detected by a γ-detector behind the absorber in case of transmission spectroscopy, this way yielding the sample specific Mössbauer spectrum.

The hyperfine structure of such Mössbauer spectra yields information about the observed nucleus (e.g. nuclear magnetic moments, electric quadrupole moments) and the electronic properties of the local atomic environment. In the following section 3.2.1 the Mössbauer effect will be

explained in detail. Subsequently, the experimental information obtainable by Mössbauer spectroscopy is reviewed. For further reviews of the technique it is referred to the books of H. Wegener [136], P. Gütlich [137], D. Barb [138] and G. Schatz [116].

3.2.1 Mössbauer effect

The Mössbauer effect is a recoilless absorption and emission process of γ-rays by atomic nuclei embedded in a solid. In principle, for a transition of a certain nucleus from an excited energy level E_a into a lower energy state, *viz.*, the ground state E_g, with the accompanying emission of γ-rays, this emission generally causes a recoil of the nucleus. However, Mössbauer discovered the possiblity to have such transitions in which the recoil is absorbed by the whole crystal the emitting nucleus is bound into. γ-rays are a type of radioactive radiation resulting from a transition of a nucleus from an excited high-energy state to a lower energy state. The energy of the emitted γ-ray E_γ corresponds to the energy difference of the two nuclear states, E_0, minus the energy E_R that is lost as recoil to the emitting atom and a velocity dependent Doppler energy shift E_D [116]. For a source moving with the velocity v, the frequency of the observed quantum shifts in the direction of movement via the Doppler effect in accordance with $\omega \rightarrow \omega_0(1 + v/c)$:

$$\begin{aligned} E_\gamma = \hbar\omega &= \hbar\omega_0 - \frac{\hbar^2 \boldsymbol{k}^2}{2M} + \hbar(\boldsymbol{k} \cdot \boldsymbol{v}) \\ &= E_0 - E_R + E_D. \end{aligned} \tag{3.26}$$

An energy state of the nucleus with mean life time τ_N has an energy uncertainty $\Gamma = \hbar/\tau_N$ with a natural line width Γ. Correspondingly, the line spectrum of the emitted γ-rays leads to a Lorentz distribution around the energy E_0 with full width at half maximum (FWHM) $\Gamma/\hbar$:

$$I(E) = \frac{const}{(E - E_0)^2 + (\frac{\Gamma}{2})^2} \tag{3.27}$$

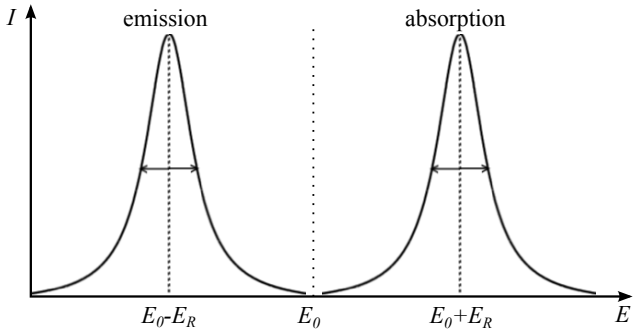

Fig. 3.4: The energy shift between absorption and emission lines after recoil of γ-quanta with a transition energy ΔE, cf. Refs. [116, 137].

For example, ^{57}Fe has a line width Γ of $4.7 \cdot 10^{-9}$ eV with a transition energy of $E_0 = 14.4$ keV and a life time $\tau_N = 1.41 \cdot 10^{-7}$ s. This transition energy leads to a large recoil with a rather large life time and in turn a very small line width. Correspondingly, the effective line width, which composed out of the natural and the Doppler line width, is also very small. Consequently, if there is recoil to be taken into account for emission and absorption of these ^{57}Fe γ-photons, the emission and absorption lines do not overlap, and thus there is no reabsorption of γ-radiation in the ensemble of Fe nuclei (see Fig. 3.4).

Qualitatively, in solid materials the situation is different. Here, the nuclei are strongly bound into a crystal lattice and do not recoil in the same way. The recoil energy is negligible because of the large lattice mass M on which the recoil acts ($E_R \sim 1/M$). In effect, there is (almost) no energy shift between the emission and absorption lines, and a reabsorption of γ-photons by the same type of nuclei is possible.

More precisely, the recoil energy is absorbed by lattice vibrations. The energy of these vibrations is quantized in units known as phonons. At low enough temperatures there is only a finite probability of a phonon to be excited. In the case that no phonons are excited, the Mössbauer effect occurs. Now, the non-shifted emission line becomes rather narrow without a broadening of the Doppler effect. The recoil-free fraction of γ-emission

is denoted by the *Debye-Waller Factor* $f_D(T)$. In these cases, since the recoil energy is negligible, the emitted gamma rays have the appropriate energy and resonance absorption can occur. With the approximation of a harmonic oscillator for the potential, in which an atomic nucleus is residing, this factor becomes

$$f_D = \exp\left(-\boldsymbol{k}^2 \left\langle x^2 \right\rangle\right), \tag{3.28}$$

with $\left\langle x^2 \right\rangle$ the mean square oscillation amplitude of the nuclei in γ-ray direction.

The exact form of $\left\langle x^2 \right\rangle$ depends on the phonon density of states for a given crystal lattice. For real solids, the phonon frequency spectrum often is approximated by the Debye model. It describes the lattice oscillations in a solid as a continuous phonon spectrum with a density of states of $Z(\Omega) = 9N\hbar^3\Omega^2/k_B^3\Theta_D^3$, the Debye frequency $\Omega_D = k_B\Theta_D/\hbar$ and the material specific Debye temperature Θ_D. The Debye temperature depends on strength of bounding from a nuclei into the crystal lattice, e.g. in case of pure iron $\Theta_D(Fe) = 470$ K. After all, at low temperatures $T << \Theta_D$ it leads to a T^2 dependency of $\left\langle x^2 \right\rangle$, which transforms into a linear dependency at high temperatures $T >> \Theta_D$. At low temperatures the Debye-Waller factor follows

$$f_D(T) = \exp\left\{-\frac{\hbar^2\boldsymbol{k}^2}{2M}\frac{3}{2k_B\Theta_D}\left[1 + \frac{2\pi^2}{3}\left(\frac{T}{\Theta_D}\right)^2\right]\right\}. \tag{3.29}$$

For the detection of the Mössbauer effect, the factor $f_D(T)$ should be as large as possible. This can be achieved by a small recoil energy E_γ, with measurements at low temperatures T and for a Debye temperature Θ_D [116].

3.2.2 Second order doppler shift

An additional shift of the emission and absorption lines with respect to each other for a given nucleus in Mössbauer spectroscopy is caused by a

relativistic effect, the second order Doppler effect. It induces a frequency shift of the emitted γ-rays because of thermal oscillations of the atoms. The second order Doppler shift derived from

$$\omega = \omega_0 \sqrt{1 - \frac{v^2}{c^2}} + \boldsymbol{k} \cdot \boldsymbol{v} = \omega_0 + \boldsymbol{k} \cdot \boldsymbol{v} - \frac{\omega_0^2 v^2}{2c^2} + \cdots , \tag{3.30}$$

with the wave vector $\boldsymbol{k}$ and the frequency ω in the rest frame of the observer and the frequency ω_0 in the rest frame of the emitter. In contrast to the first term linear in v (the linear Doppler effect), the second term, the second order Doppler shift, is independent of the velocity direction. On average, the mean velocity $< v >$ of the nucleus (by averaging over the velocity of an oscillation during the emission time) is zero. However, the mean square velocity $< v^2 >$ is not necessarily zero and can shift the Mössbauer lines as function of experimental parameters. The second order Doppler shift is dependent on variations of i.e. temperature, pressure or Debye-temperature.

Mössbauer spectra of real materials consist of one or more resonance lines. The number and positions of these lines with respect to the relative velocity between source and absorber are the result of interactions between atomic nuclei and local electric and/or magnetic fields. These interactions result in the isomer shift of resonance lines, the occurrence of a quadrupolar splitting and a magnetic splitting of the resonance lines.

3.2.3 Isomer shift

The isomeric shift is a shift of atomic spectral lines as a result of the replacement of one nuclear isomer by another. The isomeric shift provides important information about the nuclear structure and the physical and chemical environment of atoms. Specifically, in Mössbauer spectroscopy it is due to the combined effect of the recoil-free Mössbauer transition occurring in different local environments during emission and absorption of the γ quanta.

The isomeric shift depends on different excited nuclear states with differ-

ent radii. The enlarged nucleus exhibits, due to the electrostatic interaction between nucleus and electron shell a monopole energy E_I at the nucleus:

$$E_I = \frac{Ze^2}{6\epsilon_0} \left|\psi(0)\right|^2 \left\langle r^2 \right\rangle \tag{3.31}$$

with a mean quadratic radius $\left\langle r^2 \right\rangle$, a electric charge Ze and a probability density of the electrons at the nucleus $\left|\psi(\boldsymbol{x} = \mathbf{0})\right|^2$.
In the experimental arrangement of Mössbauer experiments the isomeric shift occurs between the different local environment in the source compared to the absorber (see Fig. 3.5 as an example of ^{57}Fe). At the transition of an excited state a to the ground state g, the radius of the nucleus changes. This leads to a change in the charge distribution and an altered electrostatic interaction energy between the nucleus and the electron shell. In addition, a different probability of the presence of s-electrons in the source $|\psi(0)|^2_Q$ and in the absorber $|\psi(0)|^2_A$ contributes to the isomeric shift:

$$\delta E_I = \frac{Ze^2}{6\epsilon_0} \left(\left|\psi(0)_A\right|^2 - \left|\psi(0)_Q\right|^2\right) \left(\left\langle r^2 \right\rangle_a - \left\langle r^2 \right\rangle_g\right). \tag{3.32}$$

For the experimental arrangement of the Mössbauer effect, where the source is moved with respect to the absorber, leading to an energy shift between source and absorber because of the Doppler effect, the isomer shift is then written in terms of the velocity of the source at resonance:

$$v_{iso} = \frac{Ze^2 c}{6\epsilon_0 \hbar\omega_0} \left(\left|\psi(0)_A\right|^2 - \left|\psi(0)_Q\right|^2\right) \left(\left\langle r^2 \right\rangle_a - \left\langle r^2 \right\rangle_g\right) \tag{3.33}$$

3.2.4 Electric quadrupole splitting

If the Mössbauer nucleus has a quadrupole moment Q, it leads to a quadrupole splitting if there is an electric field gradient at the site of the nucleus. A nucleus that has a spin quantum number $I > 1/2$ has a non-spherical charge distribution with a splitting of the energy states of the nucleus into $(I + 1/2)$ sublevels, cf. Fig. 3.5. These sublevels are charac-

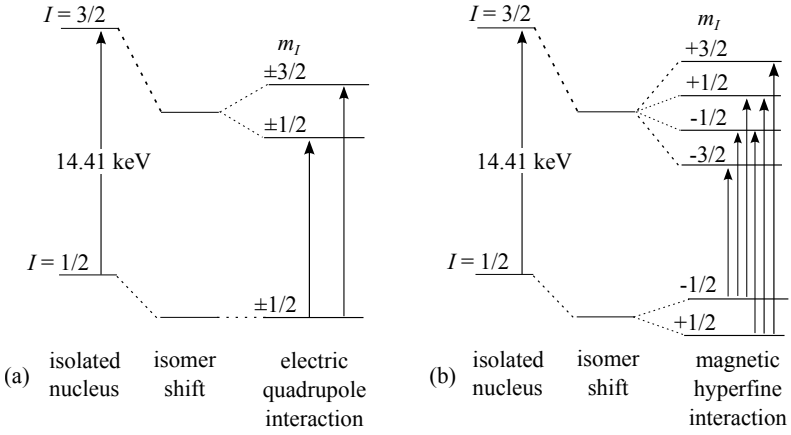

Fig. 3.5: Energy level diagrams for ^{57}Fe with an isomer shift and an additional electrical quadrupole interaction (a) or magnetic hyperfine field (b) [137]. The case of simultaneously observing an electrical quadrupole interaction and an additional magnetic hyperfine field is much more complicated and not depicted.

terized by the magnetic spin quantum number m_I.

The electric quadrupole interaction between nuclear moments and the electrical field gradient ($\nabla E_{ij} = -\frac{\partial^2 V}{\partial x_i x_j} = -V_{ij}$) gives rise to a splitting of the nuclear energy levels. Here, V_{ij} are components for a traceless tensor of the electric field gradient. For V_{ij} contribute only charges, which are not located at the nucleus. The asymmetry parameter η is defined as

$$\eta = \left(\frac{V_{xx} - V_{yy}}{V_{zz}} \right) \tag{3.34}$$

with $|V_{xx}| \leq |V_{yy}| \leq |V_{zz}|$ (and thus $0 \leq \eta \leq 1$) in a suitable coordinate system. Now, the electric field gradient can be specified by the two parameters V_{zz} and η. For the energy of the quadrupole splitting it follows

$$E_Q = \frac{eQV_{zz}}{4I(2I-1)} \left[3m_I^2 - I(I+1) \right] \left(1 + \frac{\eta^2}{3} \right)^{\frac{1}{2}} . \tag{3.35}$$

In principle, for an exact calculation the components V_{ij} have to be de-

termined based on the contributions of lattice ions, of the valence electrons and conduction electrons. The determination of the spatial distribution of the conduction electrons is quite difficult, and essentially requires band structure calculations in non-cubic solids. Instead, and simplified, the point charge model is often used as an approximate approach, with

$$V_{zz} = (1 - \gamma_\infty)V_{zz}(lat) + (1 - R)V_{zz}(elec), \tag{3.36}$$

as superposition of an electric field gradient of the lattice $V_{zz}(lat)$ and of the valence electrons $V_{zz}(elec)$. The polarization of the atomic shell by electric fields of valence electrons and the crystal lattice are taken into account by the Sternheimer factor R and γ.

$V_{zz}(lat)$ can be easily calculated within the point charge model as all contributions of the lattice are added and the point of origin is assumed to be in the center of the nucleus. Hence, the total electric field gradient is determined as

$$V_{ij}(lat) = \frac{Ze}{4\pi\epsilon_0} \sum_{\alpha \neq 0} \frac{1}{\boldsymbol{r}_\alpha^5} \begin{pmatrix} 3x_\alpha^2 - \boldsymbol{r}_\alpha^2 & 3x_\alpha y_\alpha & 3x_\alpha z_\alpha \\ 3x_\alpha y_\alpha & 3y_\alpha^2 - \boldsymbol{r}_\alpha^2 & 3y_\alpha z_\alpha \\ 3x_\alpha z_\alpha & 3y_\alpha z_\alpha & 3z_\alpha^2 - \boldsymbol{r}_\alpha^2 \end{pmatrix}, \tag{3.37}$$

with the vector $\boldsymbol{r}_\alpha = \left(x_\alpha^2 + y_\alpha^2 + z_\alpha^2\right)^{1/2}$ of the point charge α.

Experimentally, in Mössbauer spectroscopy the electric quadrupole interaction shows up as a symmetric splitting of resonance lines around the isomer shift v_{iso} (see Fig. 3.5). In result, the quadrupole transition energy ΔE_Q of an excited level ($I = \pm 3/2$ and $m_I = \pm 3/2, \pm 1/2$) to the ground level ($I = \pm 1/2$ and $m_I = \pm 1/2$) of, in this case ^{57}Fe, amounts to

$$\Delta E_Q = \frac{eQV_{zz}}{2} \left(1 + \frac{\eta^2}{3}\right)^{\frac{1}{2}}. \tag{3.38}$$

This in turn leads in terms of the Doppler shifted energy of the source

measured as velocity to a Mössbauer line splitting of

$$\Delta v = eQV_{zz}c/2\hbar\omega_0. \tag{3.39}$$

3.2.5 Hyperfine splitting in magnetic fields

Magnetic hyperfine splitting can be described by a dipole interaction between a nuclear magnetic moment $\boldsymbol{\mu}$ and a magnetic field $\boldsymbol{B}$. The magnetic field may either stem from local magnetic moments or from externally applied magnetic fields. The magnetic field leads to a Zeemann splitting of the energy levels of the nucleus into $(2I+1)$ hyperfine levels (cf. Fig. 3.5):

$$E = -\boldsymbol{\mu} \cdot \boldsymbol{B} = \mu B \frac{m_I}{I}. \tag{3.40}$$

In the absence of quadrupolar splitting, a resonance spectrum of six different lines can be observed for ^{57}Fe. Under consideration of the selection rule $|m_a - m_g| \leq 1$ for the excited state (m_a) and the ground state (m_g), the six lines correspond to transitions with changes of the magnetic quantum number $m_I = 0, \pm 1$ (Fig. 3.5). This in turn leads to a transition energy from the excited (a) to the ground state (g) as

$$\begin{aligned} \Delta E &= \left(E_a - \mu_a \boldsymbol{B}\frac{m_a}{I_a}\right) - \left(E_g - \mu_g \boldsymbol{B}\frac{m_g}{I_g}\right) \\ &= \hbar\omega_0 - \boldsymbol{B}\left(\mu_a \frac{m_a}{I_a} - \mu_g \frac{m_g}{I_g}\right). \end{aligned} \tag{3.41}$$

In terms of the source velocity it causes a splitting

$$v = \frac{c}{\hbar\omega_0}\left(m_g \frac{\mu_g}{I_g} - m_a \frac{\mu_a}{I_a}\right)\boldsymbol{B}. \tag{3.42}$$

Microscopically, the magnetic field at the nucleus is a superposition of a constant nuclear term and a variable magnetic term, which is influenced by the details of the electronic structure. The total effective magnetic field

is given by

$$\boldsymbol{B} = \boldsymbol{B}_{contact} + \boldsymbol{B}_{orbital} + \boldsymbol{B}_{dipolar} + \boldsymbol{B}_{extern}. \tag{3.43}$$

Here, the main contribution is provided by the Fermi contact field $B_{contact}$, which arises from s-electrons with either spin $\uparrow$ or spin $\downarrow$ at the nucleus as a consequence of spin polarization of the inner filled s-shells by spin-polarized partially filled outer shells. This polarization is due to unpaired electrons in the d- or f-orbitals causing a different probability density of s-electrons with spin $\uparrow$ and spin $\downarrow$ at the nucleus. This can be expressed as

$$B_{contact} = -\frac{8\pi}{3}\mu_0\mu_B \left(|\psi_{s\uparrow}(0)|^2 - |\psi_{s\downarrow}(0)|^2\right) \tag{3.44}$$

Furthermore, a contribution $B_{orbital}$ arises from the orbital motion of valence electrons with the orbital momentum quantum number $\boldsymbol{L}$:

$$B_{orbital} = \frac{2\mu_0\mu_B}{4\pi}\langle r^{-3}\rangle\langle \boldsymbol{L}\rangle. \tag{3.45}$$

In transition metals $\boldsymbol{L}$ is usually quenched by interactions with the crystal field, but it can be substantial in rare earth ions.

The spin-dipolar field $B_{dipolar}$ arises from dipolar interactions between the nucleus and the total electron spin moment $\boldsymbol{S}$ of for instance the $3d$- or $4f$-electrons. $B_{dipolar}$ can be expressed as

$$B_{dipolar} = -2\mu_B\langle \boldsymbol{S}\rangle\langle r^{-3}\rangle\langle 3\cos^2\theta - 1\rangle. \tag{3.46}$$

Again, in transition metal compounds the magnitude are zero in consequence of cubic symmetry this field, but it can be substantial in rare earth materials.

For an arbitrary material, all contributions may have an effect and add to the total internal effective magnetic field $B_{int} = B_{contact} + B_{orbital} + B_{dipolar}$. By applying an external

magnetic field of known size and direction, the size and the direction of the internal effective magnetic field B_{int} of the investigated material can be determined.

For example, in pure α-iron metal the Fermi contact at ^{57}Fe field supplies the largest contribution of $B_{contact} = -47$ T, which is reduced from spin-polarized s-electrons due to the $3d$-electrons. However, the remaining magnetic fields add a value of $\sim +14$ T. This yields to a total magnetic hyperfine field at the nucleus of about -33 T with a magnetic momentum of the excited state of $\mu_a = -0.1534\,\mu_N$ oriented against the alignment of the external magnetization [116, 136].

4 Non-centrosymmetric heavy fermions: $CePt_3B_{1-x}Si_x$

In this chapter a series of experiments by means of various bulk and microscopic measurements of an alloyed series of the non-centrosymmetric system $CePt_3B_{1-x}Si_x$ for $0 \leq x \leq 1$ is presented. More specifically, the magnetic phases of the heavy fermion superconductor $CePt_3Si$ and the isostructural $CePt_3B$ are investigated by replacing boron by silicon. The increasing electron correlations with replacement of B by Si leads to the disappearance of one magnetic phase of $CePt_3B$, while a second magnetic state seems to persist. Thus, the aim of this chapter is to characterize the magnetic phase diagram in $CePt_3B_{1-x}Si_x$ and to explore the correlation between magnetic order and unconventional superconductivity in $CePt_3Si$.

4.1 Basic properties of $CePt_3Si$ and $CePt_3B$

Throughout the past three decades topics of prime interest in the field of studies on heavy fermion superconductors are the mechanisms of the pairing and the symmetry of the superconducting state [139, 140]. For conventional superconductors with a spin singlet state, it is predicted by the Bardeen-Cooper-Schrieffer (BCS) theory that an electron-phonon mediated process produces pairing of electrons to Cooper pairs. In contrast, for the spin triplet state in unconventional superconductors there are strong arguments that the binding of electrons to Cooper pairs occurs via spin fluctuations [7].

In this context, $CePt_3Si$ is the first heavy fermion superconductor with a

lack of inversion symmetry of its crystallographic lattice [15], cf. section 2.2.3. This causes a spin-orbit splitting of the Fermi surface, which might generate chiral spin states [141]. A pure spin triplet pairing in such a non-centrosymmetric system is excluded because of fundamental symmetry arguments [142]. However, $CePt_3Si$ exhibits an anomalously large superconducting upper critical field $H_{c2} \approx 5$ T [15]. To resolve this conflict, nowadays the common view is that the superconducting pairing involves an admixture of a spin-singlet and triplet state. Still, up to now, a comprehensive explanation of superconductivity in these non-centrosymmetric systems is lacking.

Therefore, $CePt_3Si$ has been the focus of very intensive research efforts in recent years [15, 51, 144–150]. This system exhibits an unconventional heavy fermion superconducting ground state ($\gamma = 0.39$ J/mole K^2) below $T_c = 0.75$ K (0.45 K in a high quality single crystal [147]; discrepancy has not been resolved so far). This superconducting state coexists with a long-range antiferromagnetically ordered state, with an ordering wave vector $\boldsymbol{q} = (0, 0, 0.5)$ of strongly reduced moments $\mu_{ord} = 0.16\,\mu_B$/Ce atom being detected below the Néel temperature $T_N = 2.2$ K (see Fig. 4.1(b) for the spin structure) [143, 151, 152].

By contrast, the isostructural system $CePt_3B$ does not show superconductivity at low temperatures and no heavy fermion behavior [16]. Both $CePt_3Si$ and $CePt_3B$ crystallize in the tetragonal non-centrosymmetric $CePt_3B$ structure (space group $P4mm$) at ambient pressure with lattice parameters $a = 4.072/4.003$ Å and $c = 5.442/5.075$ Å for the Si/B compound, respectively (Fig. 4.1(a)) [15, 16, 146]. With these much smaller lattice parameters of $CePt_3B$, compared to $CePt_3Si$, it might be argued that chemical pressure effects take place here, that in some sense $CePt_3B$ would represent a high pressure variant of $CePt_3Si$. However, with the replacement of silicon by boron the electron count is lower by one electron in $CePt_3B$. Naively, one could argue that this should tend to weaken the hybridization strength because of a lower electron density corresponding to a reduced chemical pressure. Thus, from hand-waiving it is not obvious

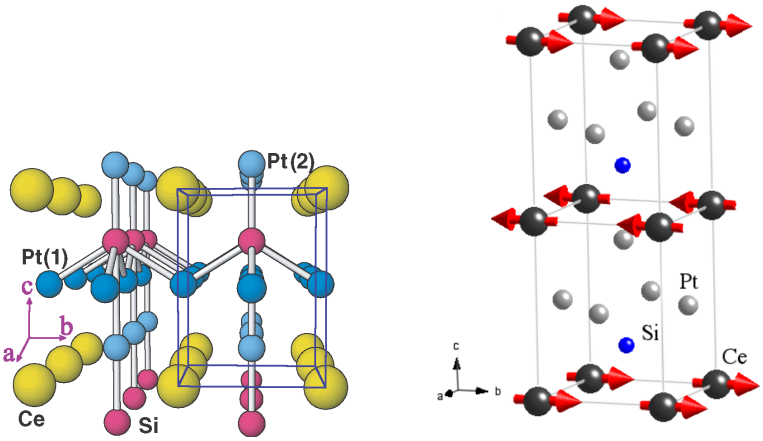

Fig. 4.1: (a) The crystal structure of $CePt_3Si$ and $CePt_3B$ [15] and (b) the magnetic structure of $CePt_3Si$ below the Néel temperature T_N [143]; for details see text.

if $CePt_3B$ should be considered a high or low pressure variant of $CePt_3Si$. Effectively, the experimentally observed physical properties of $CePt_3B$ appear to lead to the conclusion that this material is a local moment magnet with much weaker electronic correlations than $CePt_3Si$. Based on thermodynamic and transport experiments it has been established that $CePt_3B$ undergoes two magnetic transitions at low temperatures, the first one into a state of essentially antiferromagnetic (AFM) nature below $T_N = 7.8$ K, the latter one into a state with a weakly ferromagnetic (FM) signature below $T_C \sim 4.5 - 6$ K [16, 146]. To account for the two magnetic phases in $CePt_3B$ one would argue that there is a transition of large magnetic moments (order of magnitude $\sim \mu_B$) into an antiferromagnetic structure below T_N, which transforms into a weakly ferromagnetic state below T_C through canting of the magnetic moments. Within this line of thought, the canting might be a consequence of the lacking inversion symmetry, as this would give rise to an additional magnetic exchange term, the Dzyahloshinskii-Moriya (DM) interaction [153, 154]. In addition to

the magnetic coupling according to the Heisenberg model,

$$\hat{H}_H = \sum_{i,j} J_{i,j} \boldsymbol{S_i} \cdot \boldsymbol{S_j}, \tag{4.1}$$

with the magnetic coupling constant $J_{i,j}$ and i, j next neighbor spins $\boldsymbol{S_{i,j}}$, in non-centrosymetric systems the DM interaction contributes to the coupling by a term

$$\hat{H}_{DM} = \sum_{i,j} \boldsymbol{D_{ij}} (\boldsymbol{S_i} \times \boldsymbol{S_j}), \tag{4.2}$$

with $\boldsymbol{D_{ij}}$ the DM coupling vector. In non-centrosymmetric systems $\boldsymbol{D_{ij}}$ will aligned perpendicular or parallel to the connecting line of the two spins, depending on the symmetry. Therefore the spins are trying to adjust themselves at right angles in a plane perpendicular to the vector $\boldsymbol{D_{ij}}$. In combination with an antiferromagnetic Heisenberg exchange, this often leads to a canting of spins at a small angle. This in turn creates a weak ferromagnetic moment from the canting, which is perpendicular to the spin axis of the antiferromagnet [115]. Overall, here in $CePt_3B$, a combination of ferro-, antiferromagnetic or orthogonal couplings in the lattice might produces complex magnetic states such as for instances canted or helical structures [155–157].

Surprisingly, in a recent study of the magnetically ordered phases of $CePt_3B$ by means of neutron scattering and μSR this scenario could not be verified [158]. On the one hand, in μSR experiments both transitions T_N and T_C have been identified in agreement to bulk measurements. As well, the muon precession frequency suggests the presence of a fairly large ordered magnetic moment ($\sim 1\mu_B$/Ce atom) in both phases. On the other hand, in neutron powder diffraction no additional intensity from scattering in the magnetically ordered phase has been observed. As yet, this failure to detect magnetic intensity in neutron scattering is not understood.

Given that $CePt_3Si$ and $CePt_3B$ are isostructural, the question if there is a relationship between the magnetically ordered phases in both compounds arises. One possible route to study this topic is the alloying and pressure

experiments on the series of the materials $CePt_3B_{1-x}Si_x$ for $0 \leq x \leq 1$, which will be presented below.

4.2 Sample preparation and structural analysis

The polycrystalline samples of the series $CePt_3B_{1-x}Si_x$, $0 \leq x \leq 1$, studied here have been prepared by E. Bauer, TU Vienna, by means of high frequency melting of the constituents in stoichiometric ratio under argon atmosphere in a water-cooled copper crucible.

Subsequently the samples have been annealed at 880°C for 14 days in evacuated quartz tubes. Metallurgically, the materials have been characterized by means of powder x-ray diffraction. All samples crystallize in a tetragonal lattice with the space group *P4mm*, in agreement with the Refs. [15, 16, 159]. Within experimental resolution ($\sim$ 10 vol.%) no secondary phases have been detected in the diffraction spectra. The lattice

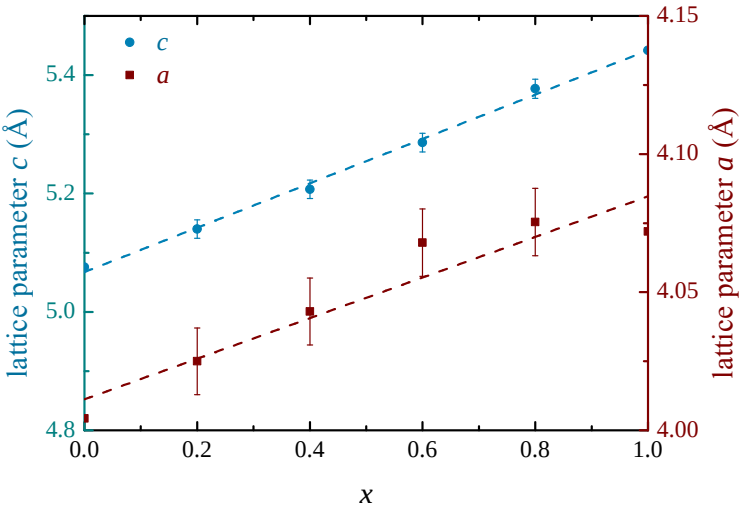

Fig. 4.2: The tetragonal lattice parameters a and c versus silicon concentration x for $CePt_3B_{1-x}Si_x$, $0 \leq x \leq 1$, under inclusion of the data for $CePt_3B$ taken from Ref. [146] and $CePt_3Si$ from Ref. [15].

x	0.0 [146]	0.2	0.4	0.6	0.8	1.0 [15]
a (Å)	4.004	4.025	4.043	4.068	4.075	4.072
c (Å)	5.075	5.140	5.207	5.286	5.377	5.442
V (Å^3)	81.36	83.27	85.11	87.48	89.29	90.23

Tab. 4.1: Tetragonal lattice parameters a and c, together with the unit cell volume V of $CePt_3B_{1-x}Si_x$ for $0 \leq x \leq 1$ (space group *P4mm*).

parameters a and c as determined from x-ray diffraction are summarized in Tab. 4.1.

Further, Fig. 4.2 visualizes the significant increase of the lattice parameters upon replacing boron by silicon, with a basically linear evolution of the lattice parameters in accordance with Vegard's law [160]. Overall, replacing boron by silicon leads to an increase of the unit cell volume by about 10% (Tab. 4.1). This increase of the unit cell volume V corresponds to a negative chemical pressure of about 16 GPa using the bulk modulus of 162 GPa of $CePt_3Si$ [161]. Notably, the change of the c lattice parameter is much larger (about 7% from $CePt_3B$ to $CePt_3Si$) than the a lattice parameter (less than 2%), which indicates some anisotropy of this chemically exerted pressure.

4.3 Magnetic behavior of $CePt_3B_{1-x}Si_x$

The DC susceptibility and magnetization of $CePt_3B_{1-x}Si_x$ for $0 \leq x < 1$ were measured employing a commercial SQUID magnetometer, at temperatures ranging from 1.8 to 300 K in magnetic fields up to 5 T. For the following analysis of the phase diagram the data measured for $CePt_3B_{1-x}Si_x$ with $x = 0.2$ and 0.4 is included. This data is taken from the PhD thesis of M. Bleckmann [162].

In ordinary metals, the spins of the free conduction electrons give rise to the Pauli paramagnetism. In an applied magnetic field the electron band is spin-split into two sub-bands, one with spin-up, the other with spin-down.

Then, the almost temperature independent Pauli susceptibility is given by

$$\chi_P = \frac{\mu_0 M}{B} = \mu_0 \mu_B^2 N(E_F), \tag{4.3}$$

with the density of states at the Fermi energy $N(E_F)$. Correspondingly, since $\chi_P \propto N(E_F) \propto m^*$ with the effective mass m^* of the electronic quasiparticles, the Pauli susceptibility is a measure for the mass enhancement of the electrons. Thus, for heavy fermion materials a largely enhanced Pauli susceptibility is observed.

In addition, due to the localized $4f$- or $5f$-moments, heavy fermion systems exhibit a Curie-Weiss-like behavior in the susceptibility at high temperatures. Altogether, in heavy fermions a crossover from high temperature Curie-Weiss-like to low temperature Pauli-paramagnetic behavior occurs on a material specific temperature scale labeled T^*. The properties of the strongly correlated electron system at temperatures $T < T^*$ can usually be explained by the Fermi-liquid theory, cf. chapter 2.1. Regarding the sample series $CePt_3B_{1-x}Si_x$ one would naively expect an increasing susceptibility with increasing x at low temperatures, which reflects an enhancement of electronic correlations. We will see in this chapter that this is not the case, cf. Fig. 4.3.

In Fig. 4.3 the temperature dependence of the magnetic susceptibility $\chi(T)$ and inverse susceptibility $\chi^{-1}(T)$ in a field $B = 1$ T are depicted. At high temperatures a paramagnetic Curie-Weiss behavior is observed. The effective Ce moments μ_{eff} are derived from fits of the data between 50 and 300 K using the Curie-Weiss law

$$\chi = [C/(T - \Theta_{CW})] + \chi_0, \tag{4.4}$$

with the Curie constant $C \propto \mu_{eff}^2$ and Curie-Weiss temperature Θ_{CW} (summarized in Tab. 4.2). The correction χ_0 to the Curie-Weiss law is minor, with χ_0 up to max. 5 % of χ_{300K}(T). This data indicates a stable Ce^{3+} state at high temperatures for all compositions of $CePt_3B_{1-x}Si_x$. Further, the Curie-Weiss temperatures Θ_{CW} indicate predominant antiferromag-

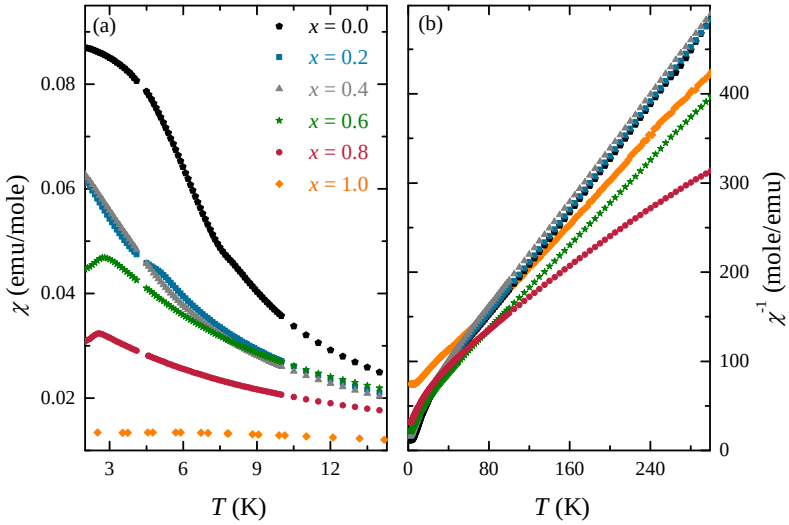

Fig. 4.3: Temperature dependency of (a) the susceptibility $\chi(T)$ and (b) inverse susceptibility $\chi^{-1}(T)$ of $CePt_3B_{1-x}Si_x$ for $0 \leq x \leq 1$ in a magnetic field of $B = 1$ T. The data for $CePt_3B_{1-x}Si_x$, $x = 0.2; 0.4$, is taken from Ref. [162] and for $CePt_3Si$ from Ref. [163].

netic interactions, which increase with silicon concentration x. Moreover, also the Kondo temperature T_K depends on the magnetic coupling strength $J \propto \Theta_{CW}$, which thus increases as well.

As demonstrated in Fig. 4.3(a), at low temperatures deviations from Curie-Weiss behavior become apparent, denoting the transitions into long-range ordered states. Transition temperatures are determined as anomalies in

x	0.0	0.2	0.4	0.6	0.8	1.0
T_N (K)	8.1	5.6	4.3	2.9	2.2	2.2
T_C (K)	5.6	2.4	2.0	-	-	-
Θ_{CW} (K)	-26	-28	-29	-31	-44	-46
μ_{eff} (μ_B)	2.39	2.39	2.34	2.56	2.58	2.54

Tab. 4.2: Magnetic transition temperatures and characteristic physical parameters of $CePt_3B_{1-x}Si_x$, as determined from susceptibility χ. Values for $CePt_3B$ and $CePt_3Si$ are taken from the Refs. [15, 16, 146].

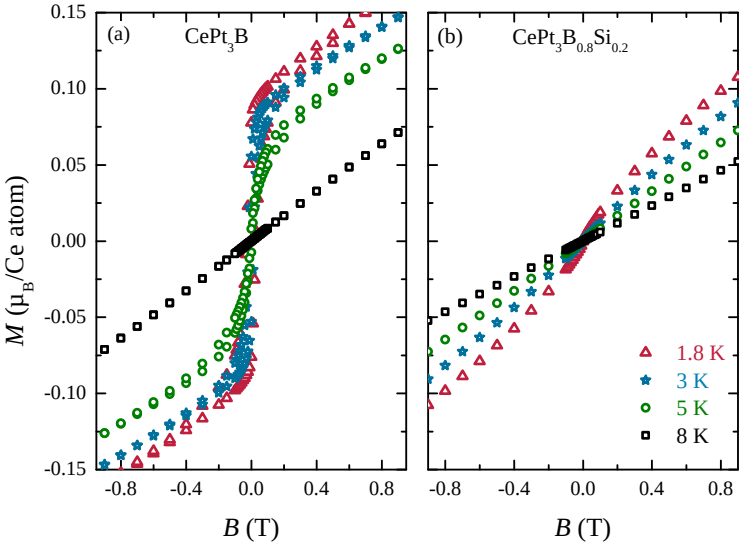

Fig. 4.4: Magnetic field dependency of the magnetization of $CePt_3B_{1-x}Si_x$ for $x = 0.0$ (a) and 0.2 (b); the data of $x = 0.2$ is taken from Ref. [162].

plots χT vs. T, with T_C identified as maximum of χT, and T_N as inflection point. In this way, the transition temperatures for $CePt_3B$ are determined as $T_N = 8.1$ K and $T_C = 5.6$ K, in good agreement with the Refs. [16, 146]. For x up to 0.4 two magnetic phase transitions, an antiferromagnetic and a ferromagnetic one, are identified. In contrast, for a larger silicon amount x the ferromagnetic transition seems to disappear, while the antiferromagnetic transition persists for all x, with T_N decreasing to 2.2 K in $CePt_3Si$. The values T_N and T_C as determined from the susceptibility are also summarized in Tab. 4.2.

Furthermore, magnetization measurements at low temperatures have been carried out on $CePt_3B_{1-x}Si_x$ for $0 \leq x \leq 0.8$, see Fig. 4.5. $CePt_3B$ exhibits weak ferromagnetic hysteresis below T_C (extrapolated remanent ferromagnetic moment for $T \to 0$ K: 0.09 μ_B/Ce atom), in good agreement with Ref. [16] (Fig. 4.5(a)). Conversely, for all alloyed samples $CePt_3B_{1-x}Si_x$, $x \neq 0$, no ferromagnetic hysteresis is observed. How-

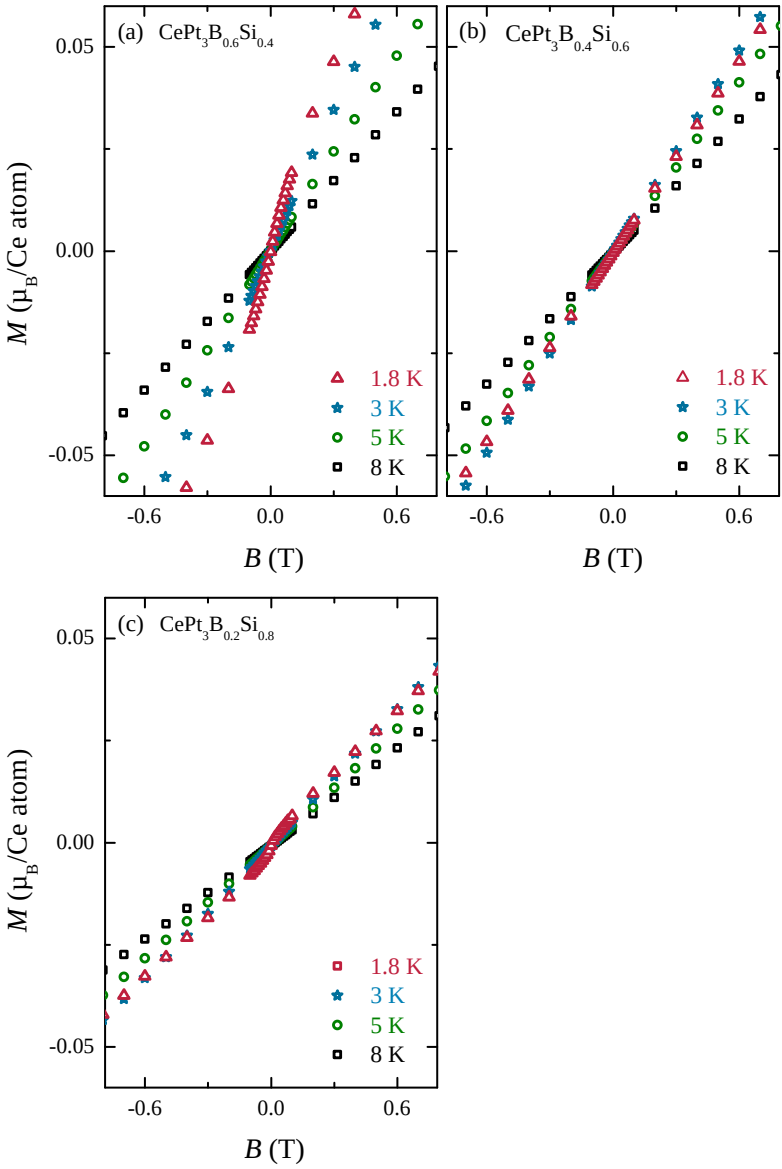

Fig. 4.5: Magnetic field dependency of the magnetization of $CePt_3B_{1-x}Si_x$ for $x = 0.4$ (a), $x = 0.6$ (b) and $x = 0.8$ (c); the data of $x = 0.4$ is taken from Ref. [162].

ever, the samples $x = 0.2$ and 0.4 both display a weakly ferromagnetic shape of the magnetization curve at 1.8 K, consistent with the observation of a second phase transition in the χ measurements. An extrapolation of the temperature dependency of the remanent magnetization yields for both ($x = 0.2$ and 0.4) a residual ferromagnetic moment at 1.8 K of $\mu \sim 0.02\ \mu_B$/Ce atom. While the samples $x = 0.6$ and 0.8 show a much smaller, barely visible, weakly ferromagnetic shape of the magnetization curve at 1.8 K.

All in all, increasing silicon concentration leads to a smaller χ at low temperatures, although electronic correlations become stronger. This seems to contradict to the strong ferromagnetic fluctuations on the boron-rich side of $CePt_3B_{1-x}Si_x$, which become weaker with increasing x.

4.4 Resistivity of $CePt_3B_{1-x}Si_x$

Resistivity measurements of $CePt_3B_{1-x}Si_x$, $0 < x < 1$, were carried out using a standard ac four-point technique at temperatures from 1.8 to 300 K. To realize a full analysis of the x dependency of the resistivity the data of $CePt_3B_{1-x}Si_x$ for $x = 0.2$ and 0.4 from the PhD thesis of M. Bleckmann [162] is included.

In the context of heavy fermion systems, the electrical resistivity represents an experimental quantity which shows a number of characteristic properties that allow conclusions on the strength of correlation effects. In effect, heavy fermion systems exhibit a much more complex behavior regarding electronic transport than normal metals. The electrical resistivity ρ of normal metals is mainly determined by the scattering of the conduction electrons from phonons or impurities. In addition, magnetically ordering systems have a magnetic scattering component. Then the temperature dependency of the electrical resistivity is given by:

$$\rho(T) = \rho_0 + \rho_{ph}(T) + \rho_{mag}. \tag{4.5}$$

ρ_0 represents the residual resistivity from scattering with impurities,

ρ_{ph} denotes phonon scattering and ρ_{mag} the magnetic scattering component. Depending on the Debye temperature Θ_D the contribution of phonon scattering has a characteristic temperature dependency: $\rho_{ph} \propto T$ holds for $T >> \Theta_D$, while a characteristic dependency $\rho_{ph} \propto T^5$ is observed for $T << \Theta_D$. ρ_{mag} can not be specified in such a quantitative manner, as it depends on the specific type of the magnetic state or fluctuations.

In heavy fermion systems the electrical resistivity also derives from the Kondo scattering of the conduction electrons, the correlation effects at low temperatures and to crystal field effects typical for f-electron systems. After Kondo, the temperature-dependent resistance increases logarithmically with decreasing temperature [30],

$$\rho(T) \cong \rho_0 \left[1 - 4JN(E_F) \ln \frac{\Delta}{k_B T}\right], \tag{4.6}$$

with the exchange interaction J between the conduction electrons and the local f-electrons. Thereby just electrons in an energy window $\delta E < |E_F \pm k_B T|$, the density of states at the Fermi energy $N(E_F)$ and the width Δ of the conduction band are considered. Phenomenologically, conduction electron clouds are forming around the Kondo scattering center, which thus shield the localized moment. In a periodic heavy fermion lattice (Kondo lattice) these Kondo clouds are now arranged on a translationally invariant lattice. They form a coherent many-body state for temperatures below $T_{ko} \sim \mathcal{O}[T_K]$, in which the system can be described by the Fermi liquid theory (cf. section 2.1).

The temperature dependency of the electrical resistivity $\rho(T)$ and the normalized resistivity $\rho/\rho_{300K}(T)$ of $CePt_3B_{1-x}Si_x$, $0.2 \leq x \leq 0.8$ are depicted in Fig. 4.6, together with the resistivity data for $CePt_3B$ and $CePt_3Si$ taken from the Refs. [16, 163]. Overall, the absolute values of the resistivities $\rho(T)$ increase with silicon amounts up to $x = 0.6$. This behavior reflects the enhanced level of disorder from chemical alloying. Correspondingly, for larger x the disorder level and absolute values $\rho(T)$ decrease.

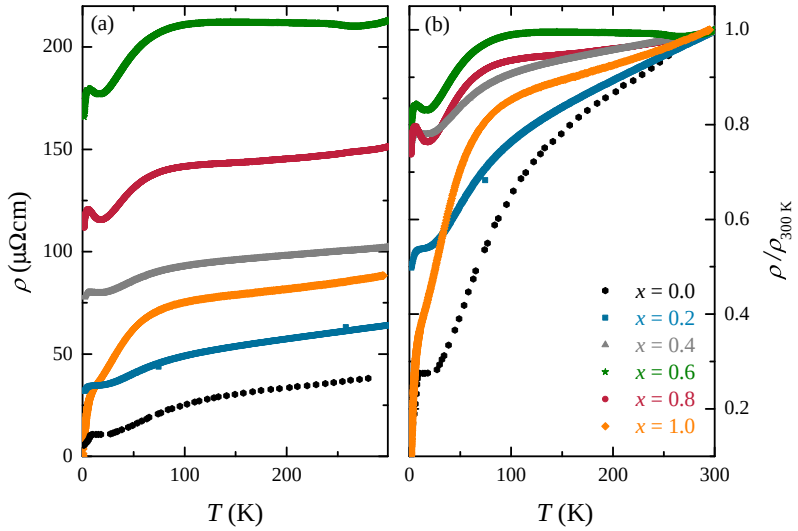

Fig. 4.6: Temperature dependence of (a) the electrical resistivity $\rho(T)$ and (b) the normalized resistivity $\rho/\rho_{300K}(T)$ of $CePt_3B_{1-x}Si_x$ for $0 \leq x \leq 1$; data for $x = 0$ and 1 taken from Refs. [16, 163].

At low temperatures (Fig. 4.7), the drops in $\rho(T)$ denote the transitions into antiferromagnetically ordered states. From the data of $\rho(T)$ the antiferromagnetic transition temperatures T_N are determined and included in Tab. 4.3. Consistent with the susceptibility, it is seen that T_N is suppressed with increasing silicon concentration. While the transition of $CePt_3B$ occurs as a rather sharp kink, the transitions in alloyed $CePt_3B_{1-x}Si_x$, $x \geq 0.2$, become broader due to chemical disorder. The transition into the weakly ferromagnetic state at T_C is not observable in the resistivity, in agreement with the conclusions from the Refs. [16, 146]. Such a behavior might be accounted for T_C a transition from a ordered magnetic state into another one, with no change of the size of the magnetic unit cell, and correspondingly no significant changes to the band structure or scattering cross sections.

Further, $\rho(T)$ of the alloying series exhibits a shallow resistive minimum for the intermediate silicon compositions $x = 0.4, 0.6$ and 0.8 at tem-

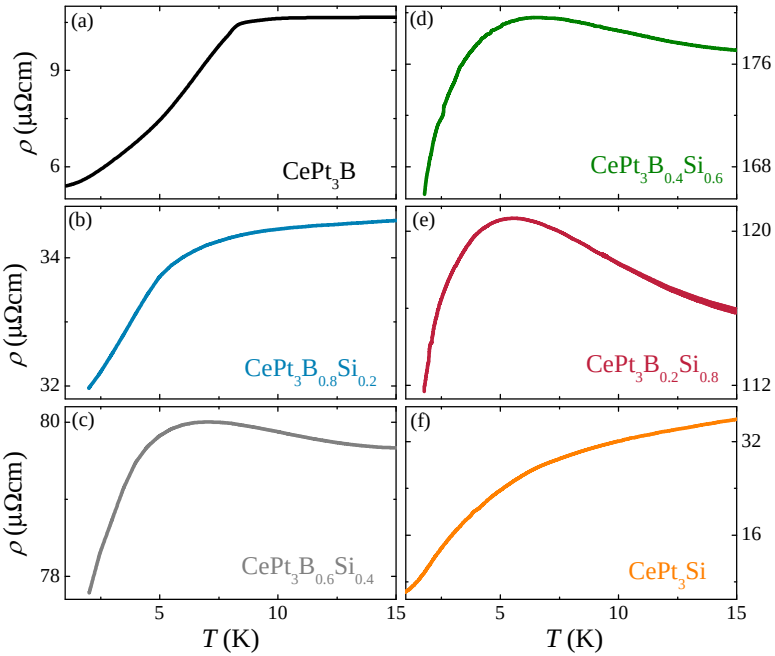

Fig. 4.7: Temperature dependence $T \leq 15$ K of the electrical resistivity $\rho(T)$ of $CePt_3B_{1-x}Si_x$ for $x = 0.0$ (a), 0.2 (b), 0.4 (c), 0.6 (d), 0.8 (e) and 1.0 (f); data for $x = 0.0$ and 1.0 taken from Refs. [16, 163].

peratures from $\sim$ 15 to 20 K. Likely, this behavior results from Kondo scattering at low temperatures [29]. Fits of the temperature range with a resistive upturn using $\rho - \rho_0 \propto ln(T)$ yield rough estimates for the Kondo temperatures and are included in Tab. 4.3. The order of magnitude of the Kondo temperatures is in agreement with the values given for $CePt_3B$ and $CePt_3Si$ (see Refs. [146, 163]), although regarding to the small temperature and resistive fitting range no firm conclusions about the x dependence of T_K can be drawn.

In an intermediate temperature range, a shoulder is observed in the (normalized) resistivity, denoting scattering from crystalline electric field (CEF) split levels. The position of the resistive shoulder can be estimated by determining the maximum of the second temperature derivative

x	0.0	0.2	0.4	0.6	0.8	1.0
T_N (K)	7.8	6.1	4.5	2.8	2.6	2.2
T_{CEF} (K)	150	143	140	130	131	119
T_K (K)	≈ 7	12	19	18	16	11

Tab. 4.3: Magnetic transition temperatures and characteristic physical parameters of $CePt_3B_{1-x}Si_x$, as determined from the resistivity ρ. Values for $CePt_3B$ and $CePt_3Si$ are taken from the Refs. [15, 16, 146].

$d^2\rho/dT^2$, T_{CEF}, which is a measure for the splitting of the low crystal field levels. The compositional dependency of this characteristic temperature T_{CEF} is summarized in Tab. 4.3, it decreases with increasing silicon composition. Previously, such crystal field effects have been attributed to a doublet-doublet splitting of the Ce^{3+} ground state [16, 146], with a level splitting of the order of magnitude of about 100 K for the different samples. The decrease of the splitting in $CePt_3B_{1-x}Si_x$ by about 20% with increasing x is consistent with the increase of the lattice parameter, leading to a weakening of the electric field strength on the silicon site.

4.5 Specific heat of $CePt_3B_{1-x}Si_x$

Specific heat experiments in zero magnetic field on $CePt_3B_{1-x}Si_x$, $0 < x < 1$, have been performed in a commercial calorimeter from 0.3 to 300 K at the Helmholtz Zentrum Berlin (Germany) and at the Brookhaven National Laboratory (USA).

The specific heat represents one of the most important physical quantities in the context of heavy fermion physics, as it is used to distinguish heavy fermions from "normal" metals. Heavy fermion systems exhibit an increased specific heat compared to normal metals, and in particular an increased electronic contribution C_{el}. Usually, the specific heat C can be separated into three terms:

$$C = C_{el} + C_{ph} + C_{mag}. \tag{4.7}$$

In addition to the electronic contribution C_{el} there exist the phonon contribution C_{ph} and the magnetic contribution C_{mag}. The specific heat at constant pressure C_p and volume C_v is usually not distinguished in solid state physics.

In this work we focus on the study of the magnetic properties. A substantial magnetic contribution C_{mag} to the specific heat can be observed in the vicinity of the phase transition $T \to T_C$, which is determined by the changes in the derivative of the magnetization, $\frac{\partial M^2}{\partial T}$. This gives rise to a sharp peak in the specific heat at the phase transition $T = T_C$ [164].

In the present context, the entropy S can be regarded as a measure for the size of the magnitude of magnetic moments. The entropy difference dS of a system is defined as

$$dS = \frac{dQ}{T} \Rightarrow S = \int \frac{C_p}{T} dT, \tag{4.8}$$

with the change of heat dQ and the temperature T. S can easily be calculated by integrating C_p/T from the experimental data. For a system with spin J in spin-wave approximation the maximum in the magnetic contribution to the entropy is achieved at high temperatures with a value $S = R\ln(2J+1)$. In the context of the Kondo effect, we deal with single electrons as Kondo scattering centers, and thus $J = S = 1/2$. Therefore, it is often convenient to measure the entropy of Kondo systems in units $R \cdot \ln 2$.

Fig. 4.8(b) depicts the characteristic temperature dependence of the dominant phonon contribution of the specific heat C_p for temperatures above 20 K, which follows the Debye model with T^3 up to 60 K. Below 20 K there is an overlap of electronic and magnetic specific heat contributions. In the following this low temperature behavior is analyzed in more detail by considering the specific heat divided by temperature, C_p/T, versus T below 10 K.

For $CePt_3B$ two magnetic phase transitions can be observed, the first as a peak in C_p/T for the antiferromagnetic transition at T_N, and the second as

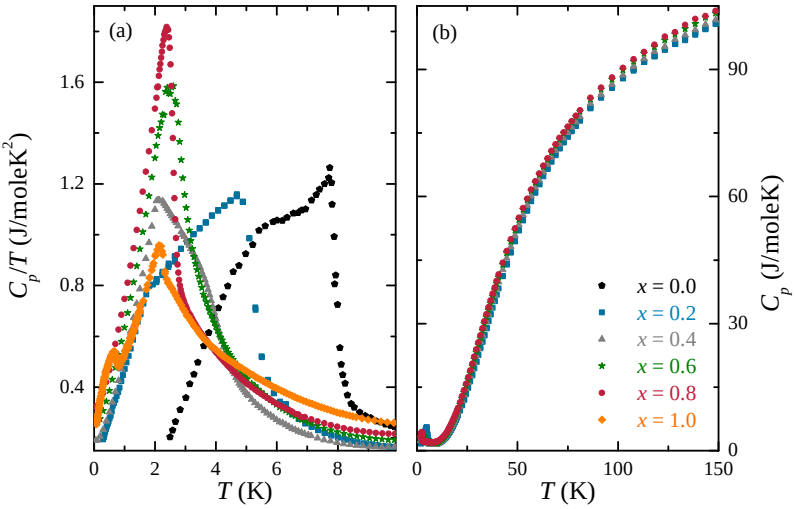

Fig. 4.8: Temperature dependence of the specific heat versus temperature C_p/T (a) and specific heat C_p (b) of $CePt_3B_{1-x}Si_x$ for $0 \leq x \leq 1$; data for $x = 0$ and 1 is taken from the Refs. [16, 163].

a shoulder for the weakly ferromagnetic transition at T_C. On a qualitative level, it is apparent that the main peak is moving to lower temperatures with increasing silicon composition. To determine the transition temperatures T_N an entropy balance model is used. For this, in a plot of the magnetic specific heat divided by temperature (C_{mag}/T) versus temperature T the transition temperatures are determined by a linear line construction with equal areas, as it is indicated in Fig. 4.9(a) for the data of the sample $x = 0.2$. The transition temperatures T_N as determined with this approach are summarized in Tab. 4.4.

In addition, the position of the specific heat shoulder at T_C is determined, which shifts to lower temperatures with increasing silicon amount. Qualitatively, the sample $x = 0.4$ has a different appearance than $x = 0.2$, with the maximum in C_p/T occurring at T_C rather than T_N. Apparently, this change of shape reflects that for this sample the entropy is shifted from the antiferromagnetic to the ferromagnetic phase, if compared to the sam-

x	0.0	0.2	0.4	0.6	0.8	1.0
T_N (K)	7.8	5.3	4.3	2.9	2.6	2.2
T_C (K)	≈ 4.5	1.8	1.7	1.6	-	-
γ (mJ/mole K^2)	57	151	295	337	349	390
$S_{mag}(T = T_N)$ $(R \ln 2)$	0.78	0.74	0.57	0.52	0.48	0.22

Tab. 4.4: Magnetic transition temperatures and characteristic physical parameters of $CePt_3B_{1-x}Si_x$, as determined from the specific heat C_p; the values for $CePt_3B$ and $CePt_3Si$ are taken from the Refs. [15, 16, 146].

ple $x = 0.2$. Ultimately, for $x > 0.6$ the weakly ferromagnetic phase is not perceivable anymore. Correspondingly, for $CePt_3Si$ two peaks are identified. The antiferromagnetic one and a second for superconductivity at $T_c = 0.7$ K, implying that ferromagnetism has disappeared for large values of silicon x.

Subsequently, the magnetic contribution C_{mag} from the experimental specific heat data is derived by subtracting the lattice contribution of isostructural, non-magnetic $LaPt_3B_{1-x}Si_x$. For this, the experimentally determined specific heat of $LaPt_3B$ and $LaPt_3Si$ (see Refs. [15, 146]) is used and the corresponding lattice contributions for alloyed $LaPt_3B_{1-x}Si_x$ are calculated from an interpolation of the specific heat of the two end points. This way, the magnetic specific heat contribution C_{mag} is obtained and plotted in Fig. 4.9(a) as C_{mag}/T versus temperature T. The plot displays clearly, that the shape of the specific heat is changing from a double-peak like structure for $x \leq 0.6$ to a single antiferromagnetic peak for $x \geq 0.8$. Previously, for $CePt_3B$ the magnetic specific heat contribution at low temperatures (in the antiferromagnetic state) was described in terms of spin wave excitations following the model of Continentino *et al.* [165],

$$C_{mag} = \frac{\delta \Delta^{7/2} \sqrt{T}}{\exp\left(\frac{\Delta}{T}\right)} \left[1 + \frac{39}{20}\left(\frac{T}{\Delta}\right) + \frac{51}{32}\left(\frac{T}{\Delta}\right)^2\right], \qquad (4.9)$$

with $\delta \propto 1/D^3$. Here, D is the spin wave velocity, while Δ represents the value of the antiferromagnetic spin wave dispersion gap. Moreover,

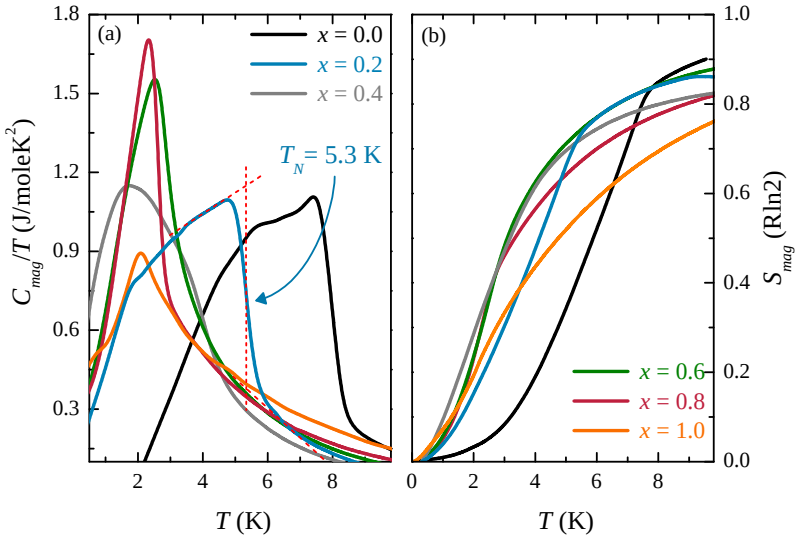

Fig. 4.9: (a) Temperature dependent magnetic contribution to the specific heat, C_{mag}, plotted as C_{mag}/T versus T and (b) temperature dependence of the magnetic entropy S_{mag} of $CePt_3B_{1-x}Si_x$ for $0 \leq x \leq 1$. The data for $x = 0.0$ and 1.0 is taken from the Refs. [16, 163], the line construction in (a) illustrates the entropy balance procedure to determine the transition temperature; for details see text.

the electronic contribution to the specific heat $C_{el} \propto \gamma T$ is also taken into account by the Sommerfeld coefficient γ. Fits of C_{mag}/T deliver a x-dependence of the Sommerfeld coefficient γ summarized in Tab. 4.4. Because of the rather complex fit of the low temperature specific heat there is an estimated uncertainty in the determination of γ of about 5 % resulting from parameter interdependence. Evidently, with increasing x the Sommerfeld coefficient and the effective electron mass m^* increase as well, thus reflecting a transition from a local moment antiferromagnet ($CePt_3B$) to a heavy fermion system ($CePt_3Si$) upon alloying.

With the magnetic specific heat extrapolated this way to $T = 0\,\mathrm{K}$ the magnetic entropy S_{mag} can be calculated (Fig. 4.9(b)). Consistent with the increasing Sommerfeld coefficient with x a suppression of the entropy

recovered at T_N, with S_{mag} at $T = T_N$, is measured in units $R \cdot \ln 2$ (summarized in Tab. 4.4). Commonly, the magnetic entropy S_{mag} is considered to scale with the size of the ordered magnetic moment. Therefore, the replacement of B by Si in $CePt_3B$ leads to a reduction of the magnetic entropy $S_{mag}(T = T_N)$ by a factor of four. This suggest that the ordered moment should be of the order of $0.6\,\mu_B$ per Ce atom for $CePt_3B$, considering for $CePt_3Si$ an ordered magnetic moment of $\mu_{ord} = 0.16\,\mu_B$ per Ce atom. This finding is consistent with our observations on the bulk properties of $CePt_3B_{1-x}Si_x$ as well as the results of muon spin rotation experiments from Ref. [158].

4.6 A pressure study on $CePt_3B$

A pressure study of the magnetic behavior of $CePt_3B$ is an alternative experimental approach to investigate the electronic ground state properties. Based on the data of the experimental bulk studies we consider $CePt_3B$ as a low pressure variant of $CePt_3Si$ (cf. sections 4.3 – 4.5). In addition, recent pressure studies $CePt_3Si$ reveal a suppression of the antiferromagnetic state at a pressure of about 0.6 GPa, while the superconductivity state persists up to a pressure of 1.5 GPa [168, 169]. Thus, for non-centrosymmetric $CePt_3Si$ the appearance of superconductivity is closely linked to the suppression of magnetic order, although quantum critical behavior has not been observed in the various physical properties. In this situation, $CePt_3B$ is investigated in a piston pressure cell (pressure $p \leq 1$ GPa) [170] and in a zirconia anvil pressure cell ($p \leq 5.5$ GPa) [167], see Fig. 4.10. Whereas, the magnetic susceptibility under pressure was measured with a commercial SQUID magnetometer. Experiments with the zirconia anvil cell for $CePt_3B$ have been performed in the laboratories of the VLT group of Prof. H. Amitsuka at the Hokkaido University, Sapporo, Japan.

Both cells consist mostly of the typical pressure cell materials, a copper-beryllium (CuBe) or copper-titanium (CuTi) composition with an extra

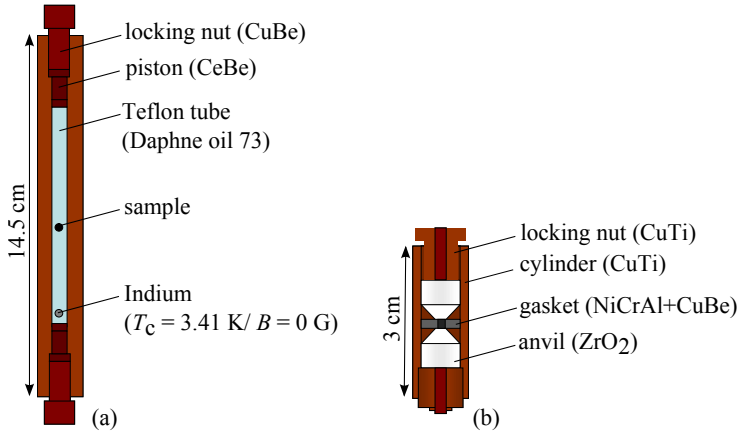

Fig. 4.10: Schematic drawings of the pressure cells used to study $CePt_3B$: (a) The piston pressure cell consists of a piston used to compress the Teflon tube with the sample inside (details shown in Ref. [166]). (b) The zirconia anvil pressure cell consist of anvils compressing the gasket with the sample inside (Tateiwa type [167]). Both cells are used for susceptibility measurements in commercial SQUID magnetometers.

high robustness, which can be easily increased by an additional tempering step of a few hours. The CuBe/CuTi composites provide an almost temperature independent magnetic signal, which in addition has a very low amplitude. This is a prerequisite to detect very small magnetic moments of the pressurized samples within the cells of about $\mu \sim 10^{-6}$ emu in a commercial SQUID magnetometer.

Commercial SQUID magnetometers have a sample chamber of about 9 mm internal diameter, which limits the pressure cells to an outer diameter of ~ 8 mm for being used in the SQUID. With this geometry, the highest possible pressure values and largest sample sizes are limited. In the piston pressure cell, where the sample resides in a Teflon tube of 1.9 mm internal diameter, a maximum pressure of 1.3 GPa can be obtained. In contrast, in the zirconia anvil pressure cell the sample dimensions are limited to $0.36 \times 0.26 \times 0.2$ mm^3 to fit into the gasket (0.5 mm internal diameter), in which besides of the sample also the pressure medium must

be incorporated.

In both pressure cell types the pressure is applied by an externally hydraulic press, whereas the pressure intensification of the samples in the two cell types is realized in different ways. For the piston pressure cell the pistons are used to transmit pressure onto a Teflon tube in the center of the cell. This tube contains the sample and indium (In) as pressure detecting medium, and is filled with the pressure medium "Daphne oil 7373". In contrast, in the zirconia anvil pressure cell two zirconia indenters are pressed onto a gasket of NiCrAl+CuBe, which contains the sample interior (filled with the sample, lead (Pb) as pressure detecting medium and also "Daphne oil 7373"). The sample chamber is much smaller, and therefore the achievable pressure is higher. Also, zirconia indenters are much harder than the CuBe piston, correspondingly a pressure of 5.5 GPa can be generated for the indenter cells as compared to a pressure of 1.3 GPa in a piston pressure cell.

The pressure in both pressure cell types is determined by the superconductivity transition temperature of In or Pb, which are also located within the pressurized volume (Teflon tub or gasket). Both, In and Pb, are type I superconductors with $T_c = 3.41$ and 7.2 K under ambient pressure and $B = 0$ G, respectively. The critical temperature T_c of indium is determined by using an ac-susceptibility set-up in a ^{4}He-crystat with a He pumping system, to achieve temperatures down to 1.5 K. The superconducting transition temperature T_c of In decreases with increasing pressure according to [171]:

$$p_{\text{In}}(\text{kbar}) = \left\{ 15.623 - \sqrt{244.077 - \frac{T_c(0) - T_c(p)}{0.0122}} \right\} \text{ kbar}. \quad (4.10)$$

In contrast, the superconducting temperature T_c of Pb is detected in a commercial SQUID magnetometer. Here, the field dependent T_c is measured for fields $-80 \leq H \leq 80$ Oe, whereas T_c as a function of the pressure can be defined at the intersection for the linear fits of the field dependent T_c for negative and positive field values, respectively. This critical temperature

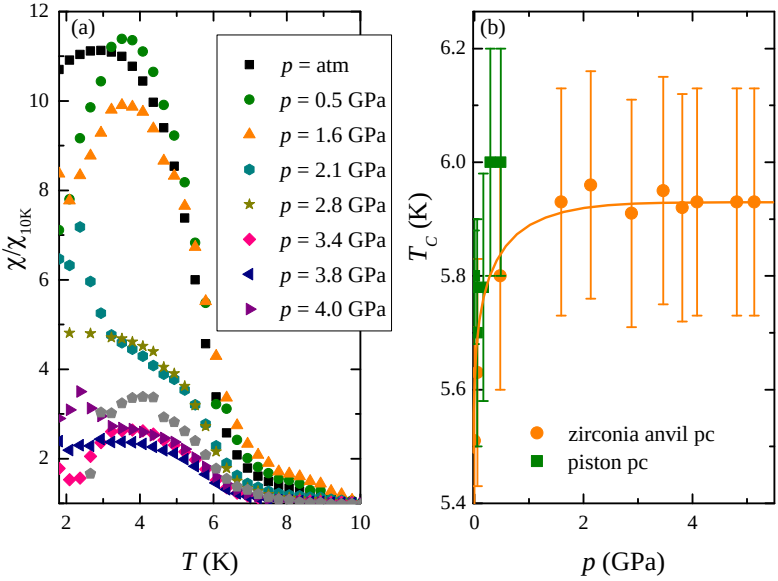

Fig. 4.11: (a) Temperature dependence up to 10 K of the susceptibility χ/χ_{10K} for various pressure values from the zirconia anvil pressure cell experiment on $CePt_3B$. (b) Pressure dependence up to $p = 5.5$ GPa of the ferromagnetic transition temperature T_C of $CePt_3B$ investigated at low temperatures in a piston pressure cell (green squares) and a zirconia anvil pressure cell (orange circles). The dashed line construction is a guide to the eye.

of Pb is related to the applied pressure via

$$p_{\mathrm{Pb}}(\mathrm{GPa}) = \left\{19.9924 - 2.81728 \cdot T_c(p) + 0.00494 \cdot T_c(p)^2\right\} \text{ GPa}. \tag{4.11}$$

As set out above, the antiferromagnetic state of $CePt_3B$ undergoes a transition producing a weakly ferromagnetic behavior for $T_C \leq 5.6$ K. In Fig. 4.11 (a) the accompanying typical ferromagnetic signature in the susceptibility χ is investigated by studying the pressure dependence up to 5.5 GPa. As in $CePt_3Si$ [169] it was observed, that overall χ of $CePt_3B$ decreases with pressure within the experimental error. The antiferromagnetic transition of $CePt_3B$ can not be determined in this experiment (cf.

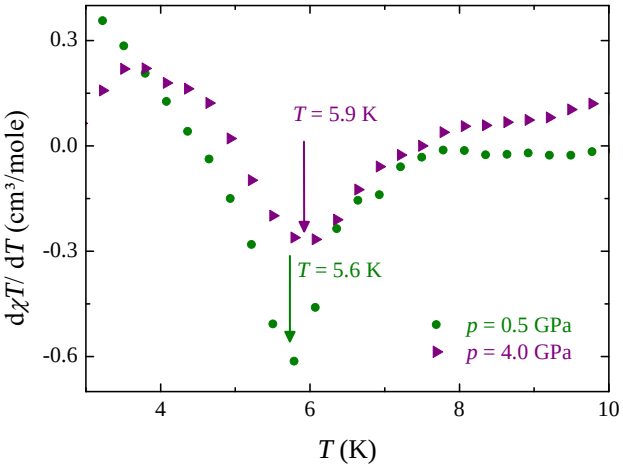

Fig. 4.12: The pressure dependence of the FM transition temperature (marked by arrows) for $CePt_3B$ can determined in the minimum of the derivative $d\chi T/dT$. Exemplary , $d\chi T/dT$ versus T are displayed for a pressure of $p = 0.5$ GPa (green circles) and $p = 4.0$ GPa (purple triangles).

section 4.3).

On the basis of the experimental data, the pressure dependence of the ferromagnetic transition temperature T_C is determined as the minimum of the derivative of χT (Fig. 4.12). This procedure gives a rather large experimental error as result of the small sample weight compared to the large background. In numbers, the zirconia anvil pressure cell gives rise to a magnetic background signal of about $\mu \sim 10^{-4}$ emu, therefore only ~ 5 % represent the sample signal of $CePt_3B$ with a mass of $m(CePt_3B) = 0.22$ mg. The overall evolution of the pressure dependence of T_C determined from both, the piston pressure cell and zirconia anvil pressure cell experiment, is depicted in Fig. 4.11 (b). Up to 0.55 GPa the transition temperature of the weakly ferromagnetic phase initially increases slightly with increasing pressure, and subsequently saturates at highest pressures. Such a behavior matches with the shape of the Doniach phase diagram in the regime of well defined local magnetic moments [25] (*viz.*, for relatively weak hybridization).

Our findings are fully consitent with the results of a resistivity study under pressure up to 1.85 GPa by Lackner *et al.* [146], who observed an increase of antiferromagnetic transition T_N by about 1 K in this pressure range. Altogether, these observations reflect that the weakly ferromagnetic phase, and correspondingly the antiferromagnetic one above T_C, are still in the local moment region of the Doniach phase diagram. Conversely, a much higher pressure would be required to drive the system into a range of strong electronic correlations and close to a magnetic instability.

4.7 μSR measurements on $CePt_3B_{1-x}Si_x$

In the previous part of this chapter the bulk properties of the alloying series $CePt_3B_{1-x}Si_x$ have been studied in detail, revealing the development of the antiferromagnetic and weakly ferromagnetic states with the replacement of boron by silicon. Now, as a next step, the magnetic properties of the sample series will be examined on a microscopic scale. For a start, we note that previous neutron diffraction experiments for $CePt_3B$ did not deliver information about the nature of the magnetic phases [158, 162]. Conversely, μSR measurements on $CePt_3B$ show a distinctive oscillatory signal below the magnetic transition temperatures, clearly indicating the presence of static magnetic fields.

Here, we extend the studies mentioned above by means of μSR experiments performed on $CePt_3B_{1-x}Si_x$ in weak transverse applied fields and zero fields using the general purpose surface-muon spectrometer (GPS) of the Swiss Muon Source at the Paul Scherrer Institute, Villigen, Switzerland. Additionally, further μSR experiments on $CePt_3B_{0.2}Si_{0.8}$ were carried out with the low temperature facility (LTF) instrument allowing to obtain temperatures between $0.019 - 1.6$ K. The samples $CePt_3B_{1-x}Si_x$ are available in polycrystalline form ($x = 0.2$ and 0.4) and as powder ($x = 0.6$ and 0.8).

4.7.1 Weak transverse field measurements

First, we present weak transverse field (wTF) μSR experiments on $CePt_3B_{1-x}Si_x$, $0.2 \leq x \leq 0.8$, in the temperature range of $1.6 - 300$ K using an external field of 3 mT applied at an angle of 90° relative to the polarized muon spin. Representative wTF asymmetry spectra are depicted in Fig. 4.13, which are recorded by forward–backward detectors. To illustrate the typical behavior, selected measurements in the paramagnetic regime (blue), close to the phase transition (green) and in the magnetically ordered state (red) are displayed for different temperatures. Qualitatively, all samples show a similar behavior. In the paramagnetic regime ($T > T_N$) the muon precession follows a harmonic oscillation (with the frequency $\nu \sim B_{ext}$) induced by the transverse external magnetic field, and in addition it is subjected to a weak damping. At the magnetic phase transition ($T \sim T_N$) the muons become influenced by an additional internal field from spontaneous magnetic ordering ($B_{int} >> B_{ext}$). This results in the observation of an initial damping of the muon oscillation in the asymmetry signal. Due to the polycrystalline nature of the investigated materials, the internal fields are oriented differently for each crystal grain. Consequently, the resulting fields at the muon site are inhomogeneous, which leads to an incoherent precession. In the long-range antiferromagnetically and weakly ferromagnetically ordered states ($T \ll T_N$) the muon oscillations from the external field is almost completely suppressed. The asymmetry spectra now acquire the character of an exponential decay function, while at a very low level paramagnetic oscillation persist.

The muon precession $A_{\mathrm{TF}}(t)$ can be described by a summation taking into account the paramagnetic signal (first term) and a magnetically ordered contribution (second term):

$$A_{\mathrm{TF}}(t) = a_1 \cos(\omega t + \phi) \exp(-\lambda_1 t) + a_2 \exp(-\lambda_2 t). \qquad (4.12)$$

The harmonic oscillation resulting from the external field in the paramagnetic state is given by a constant frequency $\nu = \omega/2\pi \sim 0.37$ MHz

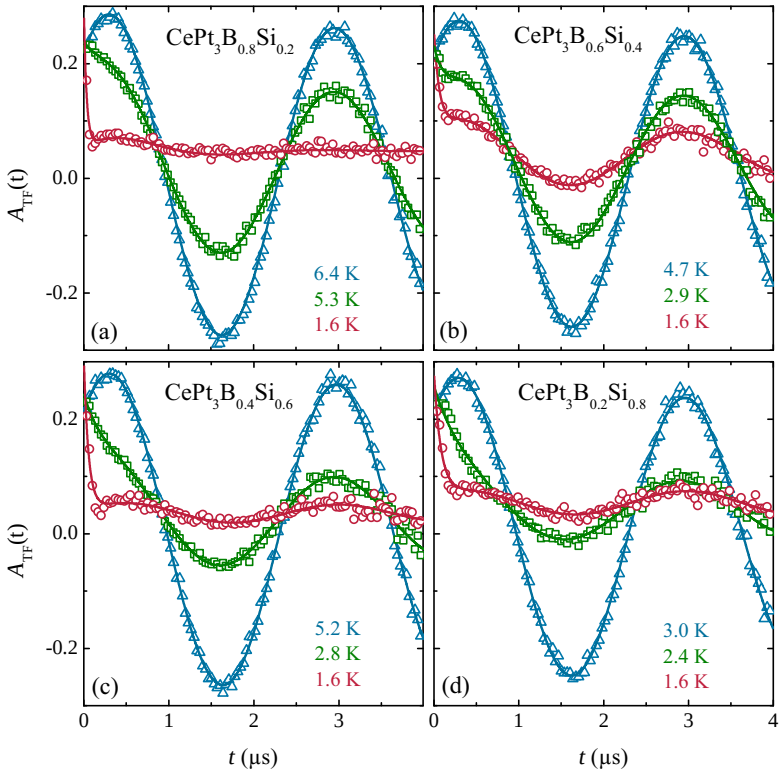

Fig. 4.13: Weak transverse field μSR asymmetry spectra at various temperatures in an external field of 3 mT of $CePt_3B_{1-x}Si_x$, $x = 0.2$ (a), 0.4 (b), 0.6 (c) and 0.8 (d). Solid lines are fits to the data, for details see text.

and a phase $\phi \sim 41°$ from a fit to the data for the full temperature range. The magnetic ordering manifests itself in an exponential decay with the decay parameter λ_2 for $T \leq T_N$. Finally, after full suppression of the paramagnetic oscillation an asymmetry signal offset of about $a_{res}/a_{tot} \sim 0.05 - 0.2$ can be identified in the magnetically ordered state, reflecting a signal contribution from the experimental device. The total asymmetry is determined to $a_{tot} = a_1 + a_2 + a_{res}$ with a varying ratio for each summand. Altogether, the time dependent asymmetry spectra from the wTF experiments are fitted with Eq. (4.12) and included as solid lines

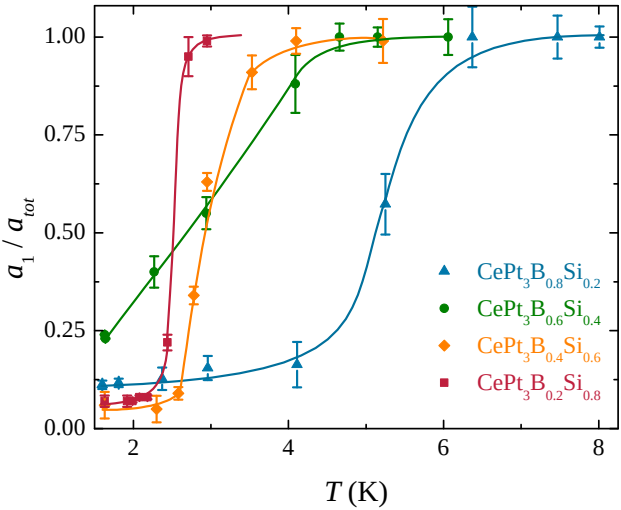

Fig. 4.14: Temperature dependence of the paramagnetic asymmetry parameter normalized to the total asymmetry a_1/a_{tot} obtained by fitting Eq. (4.12) to the wTF μSR data of $CePt_3B_{1-x}Si_x$, $0.2 \leq x \leq 0.8$, lines are guides to the eye.

in Fig. 4.14.

The transition from the paramagnetic regime, where $a_1/a_{tot} \cong 1$, into the magnetically ordered state is reflected in a temperature dependence of the asymmetry parameters, with a_2 increasing on behalf of a_1 upon transition into the magnetically ordered state. The amplitude of the oscillating signal component represented by a_1 is proportional to the paramagnetic volume fraction. Hence, a_1 serves as an indicator for the magnetically ordered volume fraction for each sample. Correspondingly, Fig. 4.14 depicts the temperature dependence of the normalized asymmetry parameter a_1/a_{tot}, as obtained from fits of Eq. (4.12) to the data. From this figure, the transition into the antiferromagnetic state can be determined from the onset of the decreasing shoulder of the temperature-dependent asymmetry parameter a_1/a_{tot} to $T_N = 6.1$ K in $CePt_3B_{0.8}Si_{0.2}$, 4.4 K in $CePt_3B_{0.6}Si_{0.4}$, 3.8 K in $CePt_3B_{0.4}Si_{0.6}$ and 2.7 K in $CePt_3B_{0.2}Si_{0.8}$, in good agreement with the results from the bulk studies described in the previous sections.

The samples $CePt_3B_{1-x}Si_x$, $x = 0.2$, 0.6 and 0.8 exhibit a fairly sharp transition with a decrease from $a_1/a_{tot} \cong 1$ in the paramagnetic regime to $a_1 \leq 0.1\, a_{tot}$ at the lowest temperatures. This proves the bulk nature of the magnetically ordered phases for these samples, with a volume fraction of the magnetically ordered phase larger than 90 % for all samples. In contrast, silicon concentrations of $x = 0.2$ and 0.4 exhibit a residual asymmetry with $a_1/a_{tot} \sim 0.11$ at lowest temperatures, which is an artifact of the experimental device. The measurements for $x = 0.2$ and 0.4 have been performed at a later time and a different slot adjustment for the μ^+-beam than for $x = 0.6$ and 0.8. In addition, the sample $CePt_3B_{0.6}Si_{0.4}$ shows a broadened transition and a magnetic volume fraction of ~ 80 % at lowest temperatures, which is in line with the residual weak oscillatory asymmetry signal observed at very low temperatures (Fig. 4.13 (b)). Also, these observations correspond to the temperature dependent magnetic specific heat contribution C_{mag}/T, which also reveals a broadened transition into the antiferromagnetic state for this sample (Fig. 4.9 (a)).

4.7.2 Zero field measurements

More detailed information on the magnetic properties, and in particular the nature of the magnetically ordered phases, are obtained from zero magnetic field (ZF) μSR experiments on $CePt_3B_{1-x}Si_x$, $0.0 \leq x \leq 0.8$. In this experimental configuration, the muon behavior only reflects the muon precession and relaxation from the internal magnetic fields in the magnetically ordered phases. Then, features like magnetic phase transitions or spin reorientation processes will result in changes of the internal magnetic fields and might show up in the muon signal.

In Fig. 4.15 time dependent μSR asymmetry spectra for $CePt_3B_{1-x}Si_x$, $0.0 \leq x \leq 0.8$ for selected temperatures are summarized. In comparison, the polarization for $CePt_3Si$ of Amato *et al.* [151] is shown in Fig. 4.16. For all samples, the transition from the paramagnetic phase into the magnetically ordered state is signaled by the occurrence of a spontaneous damped muon oscillation, which for $x > 0$ fully decays within

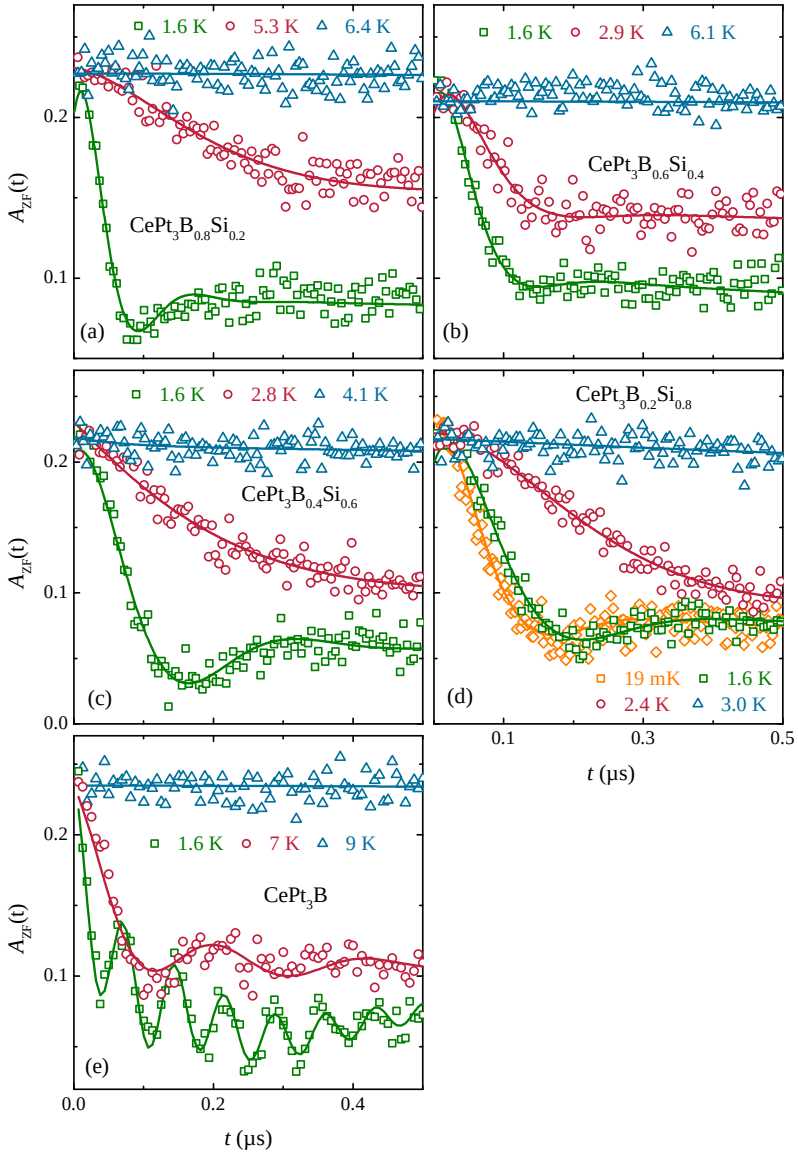

Fig. 4.15: Zero field μSR asymmetry spectra at various temperatures of $CePt_3B_{1-x}Si_x$, $x = 0.2$ (a), 0.4 (b), 0.6 (c), 0.8 (d) and 0.0 (e) from Ref. [162]. Solid lines are fits to the data. For $x = 0.8$ normalized LTF values at $T = 1.9$ mK are included.

one oscillation period. In agreement with the wTF μSR measurements, $CePt_3B_{0.6}Si_{0.4}$ is the only sample with just a weakly discernible oscillation (Fig. 4.15 (b)). Assuming that this sample contains a secondary non-magnetic phase with a volume fraction of about $20\,\%$, this behavior can be explained by a superposition of the oscillatory muon signal from the main phase and a background signal from a non-magnetic minority phase.

Furthermore, to investigate the possible presence of a ferromagnetic contribution in $CePt_3B_{0.2}Si_{0.8}$ additional ZF μSR measurements are carried out using the LTF instrument for temperatures between $0.019-1.6$ K, with one data set shown as an example in Fig. 4.15 (d). In order to compare the μSR data obtained from the GPS and LTF facilities, $A_{\rm ZF}(t)$ of LTF experiments are normalized (and adjusted to the values of GPS) to correct for the signal from silver backing in the LTF. (In the LTF experiments the sample was glued onto a high-purity silver holder.)

Following previous studies [151, 162], for $CePt_3B_{1-x}Si_x$, $0.0 \leq x \leq 1.0$, the muon signal in the magnetically ordered phases is described as a superposition of damped oscillation signals. Correspondingly, the ZF μSR asymmetry signal in the magnetically ordered state is analyzed by a superposition of n terms, were n represents the number of distinct muon sites:

$$A_{\rm ZF,magn}(t) = \sum_{i}^{n} \{\alpha_i \cos(\omega_i t + \phi_i) \exp(-\lambda_{T,i} t) + (1-\alpha_i) \exp(-\lambda_{L,i} t)\} \tag{4.13}$$

Here, the first component describes the muon precession with a frequency $\nu_i = \omega_i/2\pi$ caused by the local internal magnetic field B_{int} at each muon site. α_i denotes the fraction of transverse internal field components of the field distribution with respect to the initial muon spin, which give rise to a precession, and is expected to be 2/3 for an isotropic environment. For the temperature dependent data analyzed here a nearly constant fraction $\alpha_i \sim 0.7 \pm 0.1$ was found, indicating an almost coherent orientation for the spatial average of the localized Ce moments. As expected for a poly-

crystalline sample, the second "1/3 term" of each summand represents the fraction of muons possessing an initial polarization along the the internal field direction. Only close to the magnetic transition a deviation is observed as a consequence of the magnetic phase transition. Further, the longitudinal depolarization rate $\lambda_{L,i}$ ($\sim 0.1\,\mu s^{-1}$) reflects solely internal spin dynamics, while the transverse depolarization rate $\lambda_{T,i}$ ($\sim 10 - 20\,\mu s^{-1}$) describes both static and dynamic effects like the spin-spin-interaction. The temperature dependence of the precession frequency ω_i reflects the evolution of the (sublattice) magnetization.

For higher temperatures $T > T_N$ the paramagnetic phase is best described by the asymmetry function

$$A_{\mathrm{ZF,PM}}(t) = a_{KT} G_{KT}^{dyn}(\nu, \sigma, \Gamma, t), \tag{4.14}$$

with the dynamic Kubo-Toyabe function $G_{KT}^{dyn}(\nu, \sigma, \Gamma, t)$, the field distribution σ, the hopping rate Γ and the frequency ν (see section 3.1.5). In ZF μSR the frequency is fixed to $\nu = 0$, since the internal fields exhibit no temporal fluctuations. Γ describes dynamic effects, which are associated with hopping processes of muons between different interstitial sites. For a single muon site, the prefactors a_j in the Eqs. (4.13) and (4.14) represent the asymmetry parameters, with $\sum a_j$ giving the total asymmetry a_{tot}.

Previously, the experimental ZF muon depolarization data for $CePt_3B$ has been analyzed using Eq. (4.13) with a superposition of three terms ($n = 3$) for the magnetically ordered state and Eq. (4.14) for the paramagnetic phase, implying the existence of three distinct muon sites in the material. In these fits, the phase $\phi = 0$ and $\lambda_L \sim 0.1\,\mu s^{-1}$ are fixed for all muon sites. This procedure allows to study in detail the temperature dependence of the various fit parameters. Far below the phase transition for each muon site the transverse damping rate $\lambda_{T,i}$ is almost constant, and diverges at the phase transitions. The temperature dependence of the precession frequencies ω_i reflect the evolution of the bulk/sublattice magnetization in the antiferromagnetic and weakly ferromagnetic states, and is depicted in Fig. 4.17 for the largest frequency.

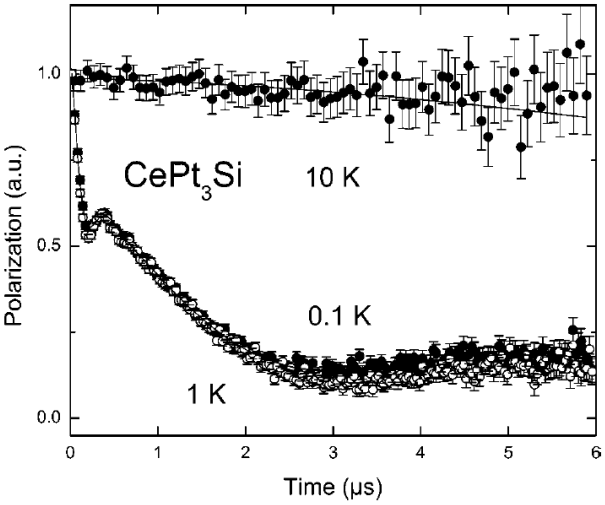

Fig. 4.16: Zero field μSR asymmetry spectra for polycrystalline $CePt_3Si$ in the superconducting phase at 0.1 K (filled circles), in the antiferromagnetic phase at 1.0 K (open circles) and in the paramagnetic phase at 10.0 K (upper curve) from Ref. [151].

Also, the antiferromagnetically ordered state in $CePt_3Si$ has been analyzed using this approach, but with a sum of two muon precession signals indicating the presence of at least two in-equivalent muon stopping sites sensing very low internal magnetic fields ($\leq$ 2.3 MHz), cf. Ref. [151] (data from that reference is included in Fig. 4.17).

All experimental ZF muon depolarization data for $CePt_3B_{1-x}Si_x$, $0.2 \leq x \leq 0.8$, has been analyzed using Eq. (4.13) with a superposition of two terms ($n = 2$) for the ordered state and Eq. (4.14) for the paramagnetic phase, which are depicted as solid lines in Fig. 4.15. In comparison, the necessity to use three muon sites for $CePt_3B$ reflects that the damping of the muon asymmetry spectra is much weaker in $CePt_3B$ than for silicon concentrations of $x \geq 0.2$. In effect, about ten oscillation periods have to be taken into account in the fit of the $CePt_3B$ data, which can only be properly done by using three muon sites (see Fig. 4.15). Per individual

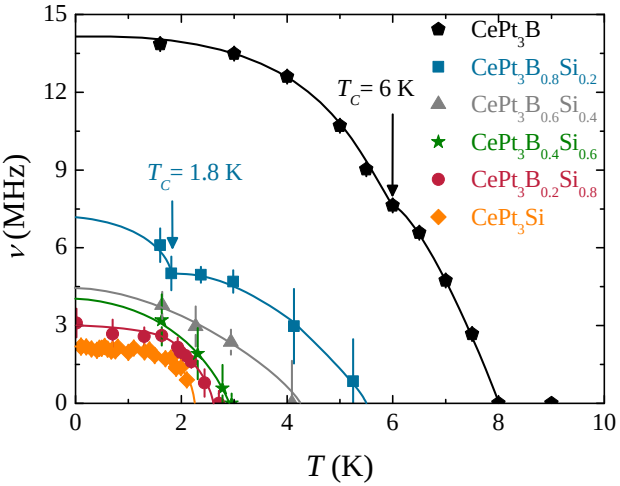

Fig. 4.17: Temperature dependence of ZF μSR frequencies of $CePt_3B_{1-x}Si_x$, $0.0 \leq x \leq 1.0$. The data for $x = 0.0$ and 1.0 is taken from the Refs. [151, 162]. Lines are included for better visibility of the transition temperatures T_N and T_C, arrows mark T_C.

muon site, however, the magnetic fields, and thus frequencies, are comparable. Conversely, for the alloyed samples the strong damping effectively wipes out the information about different local fields, *viz.*, muon sites. As well, the magnetic field associated to the precession frequency ν in Eq. (4.13) represents an average field. Now, the muon precession frequencies $\nu = \gamma_\mu / 2\pi B_{int}$ are of particular interest, which reflect the evolution of the magnetically ordered phases and magnetic moment μ_{ord} as function of temperature and silicon concentration. Fig. 4.17 displays the temperature dependent precession frequencies ν_i for $CePt_3B_{1-x}Si_x$, $0.0 \leq x \leq 1.0$. For clarity are only shown frequencies with the the highest values.

From the temperature dependence of the muon precession frequencies, the Néel temperature T_N can be estimated by determining $T(\nu = 0)$. As well, the maximum internal fields B_{int} are derived from the values $\nu(T = 0)$. Both quantities are summarized in Tab. 4.5.

Overall, we observe that the μSR frequencies decrease with increasing Si substitution. This behavior is in agreement with the observations on the magnetic bulk properties in the previous section of this chapter (section 4.5). Further, for decreasing temperature we found at first a rapid increase of precession frequencies, which for $T \rightarrow 0$ becomes almost temperature independent. Equally, T_N and $B_{int}(T = 0\ \mathrm{K})$ decrease with increasing Si concentration. For $0.0 \leq x \leq 0.4$ both quantities decrease significantly with Si alloying, while for larger x values the dependence is much weaker and for $x \rightarrow 1.0$ it approaches the behavior of $CePt_3Si$ [151].

$CePt_3B_{0.6}Si_{0.4}$ exhibits a transition into the antiferromagnetic phase at 4.3 K, whereas the specific heat $C_{mag}(T)$ only displays a weak signature at this temperature. Again, this might be attributed to a lesser quality of this particular sample, consistent with wTF μSR and bulk experiments. Summarizing the findings so far, the suppression of the antiferromagnetic phase in $CePt_3B_{1-x}Si_x$ with increasing silicon amount fully confirms the bulk measurements.

In contrast to the detection of long-range antiferromagnetic ordering, which is reflected in the occurrence of a distinct spontaneous muon precession, determining the transition into the weakly ferromagnetic phase is a much harder task. For $CePt_3B$ it was demonstrated previously that

x	T_N (K)	T_C (K)	$\nu(T = 0\ \mathrm{K})$ (MHz)	$B_{int}(T = 0\ \mathrm{K})$ (mT)
0.0	8.0	6.0	14	104
0.2	5.5	1.8	7	53
0.4	4.3	1.8	5	35
0.6	3.0	< 1.6	4	32
0.8	2.7	< 0.019	3	23
1.0	2.3	-	2	16

Tab. 4.5: Magnetic transition temperatures T_N and T_C, muon precession frequencies $\nu(T = 0\ \mathrm{K})$ and maximal internal fields $B_{int}(T = 0\ \mathrm{K})$ of $CePt_3B_{1-x}Si_x$, $0.0 \leq x \leq 1.0$, determined from ZF μSR measurements. The values for $CePt_3Si$ are taken from the Ref. [151].

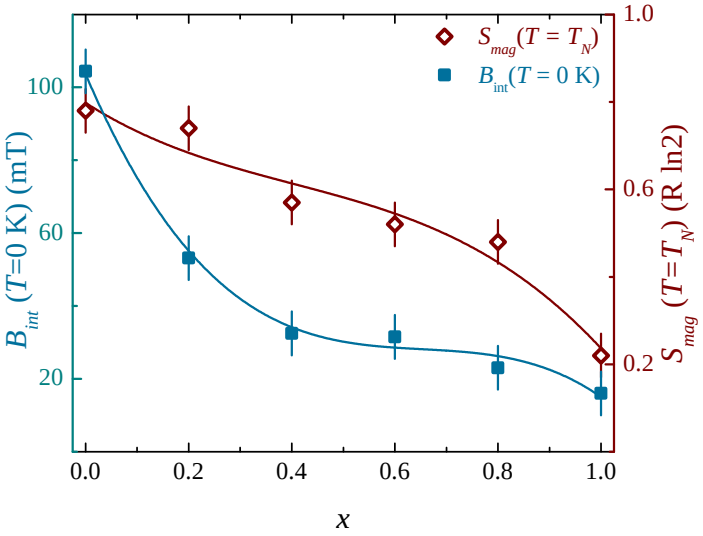

Fig. 4.18: Silicon dependency of maximal internal magnetic field $B_{int}(T = 0\ \mathrm{K})$ and magnetic entropy $S_{mag}(T = T_N)$ for $CePt_3B_{1-x}Si_x$, $0.0 \leq x \leq 1.0$. Solid lines are included for better visibility. The values for $CePt_3Si$ are taken from the Ref. [151].

a change of the slope in the temperature dependent muon oscillation frequency occurs below T_C [158, 162]. Ferromagnetic ordering causes additional muon oscillation compared to the antiferromagnetic muon precession (shown as green line in Fig. 4.15 (e)).

Further inspections of the temperature dependent oscillation frequencies reveal that for $CePt_3B_{0.8}Si_{0.2}$ there is a feature similar to that seen in $CePt_3B$. This behavior can be interpreted as an evidence for the occurrence of weak ferromagnetic ordering from canted magnetic moments, which we identified as T_C (see arrows in Fig. 4.17, values included in Tab. 4.5). The Curie temperature T_C obtained from these kinks are in agreement with the bulk measurements. $CePt_3B_{1-x}Si_x$ with $x = 0.4$ and 0.6 do not show a clear indication for ferromagnetic behavior for $T \geq 1.6$ K in the GPS experiments. Hence, from our data we set an upper limit for the ferromagnetic transition temperatures for these samples of $T_C \leq 1.6$ K.

$CePt_3B_{0.2}Si_{0.8}$ is also investigated in the LTF facility. The depolarization of the LTF measurements does not show a clear-cut feature signaling ferromagnetic behavior down to temperatures of 19 mK. As well, in the experiment no identification for superconductivity is observed.

The size of the magnetically ordered moment μ_{ord} represents one central characteristic of the magnetic properties of $CePt_3B_{1-x}Si_x$, which can be estimated from internal fields $B_{int}(T = 0\ \mathrm{K}) \propto \mu_{ord}$. A qualitative comparison with the magnetic entropy $S_{mag}(T = T_N)$ reveals that both behave in a similar way, cf. Fig. 4.18. The magnetic entropy is a measure of "disorder" of the magnetic lattice, which is proportional to μ_{ord}. Increasing the silicon concentration leads to a strictly monotone decrease of $B_{int}(T = 0\ \mathrm{K})$ and $S_{mag}(T = T_N)$, reflecting the gradual suppression of magnetic ordering with Si. Qualitatively, this can be understood within the Doniach phase diagram as a result of the increasing screening of localized magnetic moments via the Kondo effect.

Semiquantitatively, Fig. 4.18 further indicates that the size of the magnetically ordered moment changes by a factor of about 5 from $CePt_3B$ to $CePt_3Si$. Given the experimentally determined moment of $CePt_3Si$, $\mu_{ord} = 0.16\ \mu_B$/Ce atom [143], we would expect for $CePt_3B$ a moment of the order of $\mu_{ord} \sim 0.8\ \mu_B$/Ce atom, fully consistent with bulk and microscopic experimental data. Closer inspection of $B_{int}(T = 0\ \mathrm{K})$ and $S_{mag}(T = T_N)$ reveals that quantitatively a somewhat different dependence on the silicon concentration occurs. One might argue, that in contrast to the magnetic entropy, the internal field $B_{int}(T = 0\ \mathrm{K})$ is more sensitive to the weak ferromagnetic signal for $x < 0.6$. With the more rapid suppression of the ferromagnetic phase than the antiferromagnetic one, $B_{int}(T = 0\ \mathrm{K})$ initially also drops more quickly than $S_{mag}(T = T_N)$.

4.8 Summary

To summarize the findings presented here on the alloying system $CePt_3B_{1-x}Si_x$, $0.0 \leq x \leq 1.0$, antiferromagnetic and weakly ferromag-

netic phases are observed by means of various macroscopic bulk techniques and microscopic μSR experiments. The effect of silicon alloying is demonstrated in the corresponding magnetic phase diagram (Fig. 4.19), where the transition temperatures obtained from bulk and microscopic experimental techniques are plotted as function of x. While there is some variation of the absolute values of the antiferromagnetic transition temperature T_N and ferromagnetic transition temperature T_C, overall the different experiments yield rather similar results regarding the phase diagram.

All in all, the phase diagram implies that the antiferromagnetic phase of $CePt_3B$ ($T_N = 7.8$ K) transforms continuously into that of $CePt_3Si$ ($T_N = 2.2$ K), with a smooth suppression of the ordering temperatures. The antiferromagnetic transition temperatures T_N are almost constant for a silicon content of $x \geq 0.6$. In contrast, the weakly ferromagnetic phase in $CePt_3B$ ($T_C = 6.0$ K) is completely suppressed at a critical value of $x_c \sim 0.8$. Superconductivity appears close to stoichiometric $CePt_3Si$ ($T_c = 0.75$ K).

Weakly ferromagnetic behavior can occur as a result of the DM interaction in non-centrosymmetric systems by canting of antiferromagnetically ordered spins. This ferromagnetic signature is almost completely suppressed at the critical concentration x_c, suggesting that the DM interaction is weakened with Si alloying. With the complete suppression of the DM interaction unconventional superconductivity occurs in $CePt_3Si$. Qualitatively, this behavior can be discussed within the concept of the Doniach phase diagram, which considers the competition of long-range magnetic order from an RKKY-like exchange and the Kondo effect [25]. The suppression of antiferromagnetic and weakly ferromagnetic order is accompanied by a significant enhancement of electronic correlations, as evidenced by the increasing electronic specific heat coefficient γ. Here, it could be argued that in the strongly correlated state the DM interaction becomes less relevant, as it is not well-defined for a complex delocalized and correlated state of f-electrons coupled to the conduction electron band.

Also the splitting of the low-lying crystal electric field (CEF) levels de-

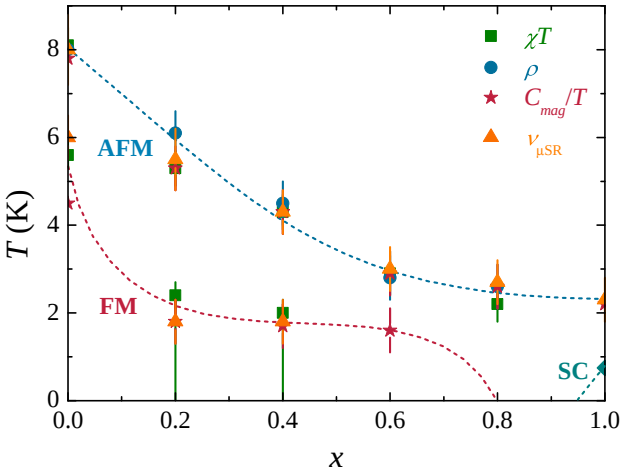

Fig. 4.19: Magnetic phase diagram of the antiferromagnetic (AFM) T_N, ferromagnetic (FM) T_C and superconducting (SC) T_c transition temperatures as function of silicon concentration x for $CePt_3B_{1-x}Si_x$, $0.0 \leq x \leq 1.0$. The values for $x = 0.0$ and 1.0 are taken from the Refs. [16, 163].

creases with Si alloying. Here, it could be asked if this variation also affects the ground state properties of $CePt_3B_{1-x}Si_x$. Now, judging from the evolution of bulk properties such as resistivity or susceptibility for the series of samples, there is only a quantitative reduction of the level splitting by about 20% with x, but no qualitative change, suggesting that the crystal field ground state remains the same for all samples. Then, with the level splitting of the order of 100 K, the ground state properties of $CePt_3B_{1-x}Si_x$ will depend primarily on the hybrdization between the f-electrons in the low lying CEF level and the conduction electrons.

With these ideas of the relevance of the DM interaction, we can speculate about the transformation of the antiferromagnetic phase in $CePt_3B$ into that of $CePt_3Si$. As indicated in the introduction, the antiferromagnetic structure in $CePt_3Si$ is rather simple, with a wave vector $\boldsymbol{q} = (0, 0, 0.5)$ [143]. While for $CePt_3B$ the wave vector is unknown so far, neutron scattering experiments have verified that it is not equal to the one of $CePt_3Si$ [158, 162]. Further, in these experiments no scattering intensity from a

magnetically ordered phase has been seen in a scattering angle range that would correspond to "ordinary" wave vectors, for instance with an antiferromagnetic doubling of the unit cell etc.. Conversely, this seems to suggest that the ordered magnetic phase in $CePt_3B$ reveals a long-range modulation of the spin-periodicity, which might lead to a signal in neutron scattering at low scattering angles inaccessible in the experiment carried out by Bleckmann [162]. Such a phase would also be consistent with the presence of the DM interaction in $CePt_3B$, which frequently produces such long-range modulations in magnetic materials. With the suppression of the DM interaction the long-range modulated state disappears, and instead the system locks into the wave vector of $CePt_3Si$.

In this context, a common approach to qualitatively assess the relevance and nature of magnetic fluctuations is to plot the product of susceptibility and temperature, χT, against the temperature T. This procedure is carried out in Fig. 4.20 for the complete alloying series $CePt_3B_{1-x}Si_x$. A decreasing product of χT with decreasing T is considered to indicate predominant antiferromagnetic fluctuations, as within the Curie Weiss law it reflects a negative temperature intercept, *viz.*, $\Theta_{CW} < 0$. Conversely, decreasing χT with increasing T indicates a ferromagnetic character of the fluctuations. From this figure, it is evident that $CePt_3B$ shows a signature of predominant ferromagnetic fluctuations, which is consistent with the phase diagram. Upon alloying, the figure suggests that these ferromagnetic fluctuations are suppressed on behalf of antiferromagnetic fluctuations. With this observation in mind, a line of thought might be that this change of the character of the fluctuation spectrum is an element relevant to account for superconductivity in $CePt_3Si$.

The silicon substitution of boron indicates for the resistivity and therefore of the Curie-Weiss temperature Θ_{CW} that for both $CePt_3B$ and $CePt_3Si$ the Kondo energy scale is of the order of 10 K, and increases with x by a factor of about two. Further, Θ_{CW} indicates that the basic magnetic energy scale T_{RKKY} is slightly larger than T_K (25 to 45 K), which also increases with Si concentration. In result, with replacing boron by silicon

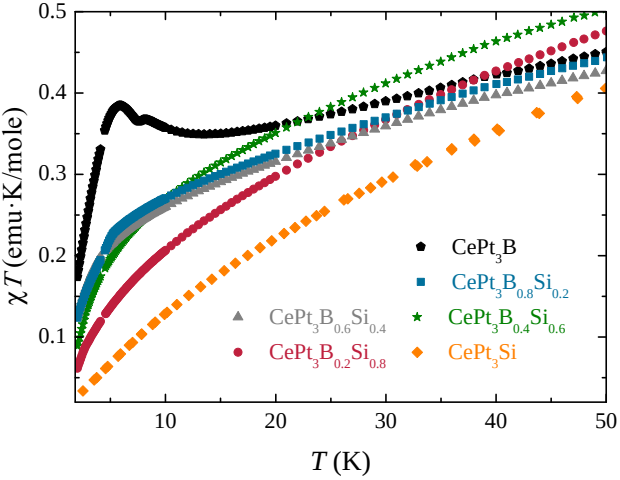

Fig. 4.20: A plot of the product χT versus T to illustrate the nature of predominant magnetic fluctuations for $CePt_3B_{1-x}Si_x$, $0.0 \leq x \leq 1.0$. The values for $CePt_3Si$ are taken from the Ref. [163].

in $CePt_3B_{1-x}Si_x$ a Doniach-like phase diagram is traversed, starting with the local moment magnet $CePt_3B$. For increasing Si amount the Kondo effect is enhanced and tends to win over magnetic order, with the end point of the heavy fermion antiferromagnetic superconductor $CePt_3Si$.

Commonly, such Doniach-like phase diagrams are observed in pressure experiments or in isoelectronic chemical pressure studies. In the present case, the situation is somewhat more complicated. Chemically a negative pressure is exerted in the alloying series $CePt_3B_{1-x}Si_x$ with a large increase of the lattice parameters with x. The negative pressure effect is also corroborated by the observation of a decreasing crystal field splitting with x. This negative pressure appears to be counteracted by the increasing electron count while replacing boron by silicon. Adding one conduction electron might lead to a small shift of the Fermi energy, and thus affect the density of states at the Fermi level. A first approximation the replacement of B by Si is often considered to not change band structure properties significantly [172–174]. These elements only produce broad bands at the

Fermi level, which should not be of great relevance to the magnetic properties of the materials. In consequence, $CePt_3B$ appears to represent a low pressure variant of $CePt_3Si$.

In fact, pressure experiments up to 5.5 GPa carried out on $CePt_3B$ show a slight increase of T_C by about $5\,\%$ with a constant ferromagnetic contribution at a pressure 1 GPa $\geq p \geq 5.5$ GPa. In contrast to $CePt_3Si$, in which the magnetic phase is suppressed at $p = 0.6$ GPa, in $CePt_3B$ a pressure of 5.5 GPa is not sufficient to eliminate the ferromagnetic behavior. Within the concept of the Doniach model, this observation reflects that $CePt_3B$ is still deep in the local moment region of the Doniach phase diagram. Therefore, a much higher pressure would be required to drive the system into the range of strong electronic correlations and close to a magnetic instability. Consequently, it would be very interesting to investigate if the properties of $CePt_3B_{1-x}Si_x$ under very high pressure resemble those of $CePt_3Si$, and in particular if the system becomes superconducting.

Given these observations, further studies are required for a detailed understanding of the magnetic instability in the context of unconventional superconductivity in $CePt_3Si$ and the suppression of the effective DM-interaction in $CePt_3B$. Possible routes to achieve this might be pressure studies of $CePt_3B_{1-x}Si_x$ and/or studies on samples with a finer gradation of the Si concentration close to $0.7 \leq x \leq 1.0$.

5 Quantum critical behavior in $Nb_{1-y}Fe_{2+y}$

As set out in the preceeding chapters, quantum critical phase transitions and the associated quantum critical behavior was observed in many intermetallic $4f$-electron compounds, for example various Ce and Yb compounds [8, 11, 102, 175]. In such correlated-electron materials quantum critical properties arise from the competition of local Kondo and non–local RKKY interactions. In contrast, only a few transition metal compounds are studied in detail in the context of quantum criticality, for instance the weakly magnetic metals MnSi [176], FeGe [177] and $ZrZn_2$ [178]. These systems with their remarkable magnetic structures (e.g., the helical spin structure in MnSi) show a number of yet not understood physical properties, which can be varied easily by means of non-thermal control parameters such as pressure and concentration. Detailed theoretical analysis [86, 108] predict spin density wave order close to quantum critical phase transitions in such itinerant systems. The same scenario possibly apply to the itinerant intermetallic series $Nb_{1-y}Fe_{2+y}$, which has been proposed to display ferromagnetic quantum criticality [17–19].

For decades $Nb_{1-y}Fe_{2+y}$ has been of interest to solid state physicists due to its rich magnetic phase diagram, which contains a number of different magnetic regions of ferromagnetic nature and a presumed spin density wave modulated state. Furthermore, at $1.5\,\%$ niobium excess a quantum critical point is observed. In this chapter the magnetic phase diagram is investigated in detail by discussing the results of two experimental techniques on a microscopic scale applied to the intermetallic series: the muon

spin relaxation and Mössbauer spectroscopy. In particular, the nature of the presumed spin density wave state is studied for stoichiometric and quantum critical $NbFe_2$.

5.1 Magnetic phase diagram of $Nb_{1-y}Fe_{2+y}$

The hexagonal $3d$-electron system $Nb_{1-y}Fe_{2+y}$ is a rare example of an itinerant intermetallic compound displaying quantum criticality in the vicinity of a weakly magnetic phase. The magnetic phase diagram of $NbFe_2$ develops upon tiny changes in stoichiometry (Fig. 5.1), and has been established via the temperature dependence of various thermodynamic and electrical transport properties [17–19, 179, 180].

$NbFe_2$ crystallizes as a C14 Laves phase system (cf. section 2.3) in the $MgZn_2$ hexagonal structure (space group $P6_3/mmc$; lattice parameter $a = 4.8401$ Å and $c = 7.8963$ Å) with 12 atoms in the unit cell (inset of Fig. 5.1). The iron atoms form a layered structure of a kagome lattice configuration with Fe($6h$) sites separated by Fe($2a$) atoms centered between the kagome triangles, while the niobium atoms occupy the interstices in this Fe structure and lie slightly out of the plane of the Fe($2a$) sites. In this structure, Fe($6h$) and Fe($2a$) atoms exist in a ratio of $3:1$. Niobium has a site symmetry of $4f$ at $(1/3, 2/3, x)$, Fe of $2a$ at $(0, 0, 0)$ and $6h$ at $(y, 2y, 3/4)$ with $x = 0.0657$ and $y = 0.1705$, respectively [18, 19].

In recent years the effect of slight changes in stoichiometry of $Nb_{1-y}Fe_{2+y}$ has been studied intensively, resulting in the discovery of a complex magnetic phase diagram divided into an Fe-rich, a stoichiometric $NbFe_2$ and a Nb-rich region. Nb- and Fe-rich $Nb_{1-y}Fe_{2+y}$, $y \leq -0.02$ and $y \geq 0.015$, respectively, possess different ferromagnetic states with ordered magnetic moments expected in a range of some tenth of a μ_B per Fe atom [18, 21]. While Nb-rich samples display a decreasing coercive field with increasing Nb-excess with a non-detectable hysteresis ($y \sim -0.06$), Fe-rich material shows a large ferromagnetic hysteresis [18]. Arrott-plot analysis yields a clear indication of a remanent mag-

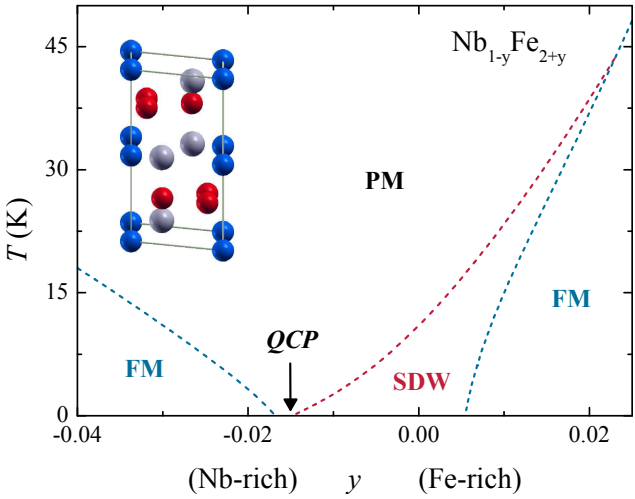

Fig. 5.1: The magnetic phase diagram for slightly doped $Nb_{1-y}Fe_{2+y}$ exhibits ferromagnetic (FM) and a presumed spin density wave (SDW) modulated states in the vicinity of a quantum critical point (QCP) at $y = 0.015$; the inset shows the hexagonal C14 Laves structure with atoms of Fe($6h$) in red, Fe($2a$) in blue, and Nb in gray; taken from Refs. [17, 19].

netization and therefore also of ferromagnetism in Nb-rich $NbFe_2$. Furthermore, spin-dependent Compton scattering measurements have been carried out for $y = +0.015$ indicating – in comparison with theoretical results concerning the spin density – a ferrimagnetic arrangement of Fe moments being more probable than a ferromagnetic state [181].

For $-0.015 \leq y \leq +0.05$ a spin density wave (SDW) modulated state is assumed to form. As for instance the stoichiometric $NbFe_2$ is representing a very rare case of SDW state in an intermetallic compound, with a Néel temperature T_N of around 10 K. The SDW ordering persists up to a concentration of 1.5% Nb-excess. Here a quantum critical point (QCP) with non-Fermi liquid behavior exists, followed by low-moment FM behavior in the Nb-rich state.

Sometimes in itinerant systems SDW or helical magnetism are found besides ferromagnetism. In the case of spontaneous ferromagnetism energy

bands are split into spin-up and spin-down bands, which are energetically shifted against each other in the absence of applied magnetic fields. Effectively, spontaneous ferromagnetism (FM) is possible if the Stoner criterion is fulfilled:

$$IN(E_F) > 1. \tag{5.1}$$

This condition for FM instabilities requires a strong Coulomb interaction ($\sim$ exchange coupling parameter I) and also a large density of states at Fermi energy $N(E_F)$ [115]. If the Stoner criterion is not satisfied, electronic interactions (which are also $\sim I$) still affect the magnetic properties of the conduction electrons. Thus, a wave vector-dependent susceptibility $\chi_{\boldsymbol{q}}$ is also enhanced by the Stoner factor and follows to:

$$\chi_{\boldsymbol{q}} = \frac{\chi_P f(q/2\pi)}{1 - IN(E_F) f(\boldsymbol{q}/2\pi)}, \tag{5.2}$$

where the function $f(\boldsymbol{q}/2\pi)$ is given by

$$f(\boldsymbol{q}/2\pi) = \frac{1}{2}\left(1 + \frac{1 - (\boldsymbol{q}/2\pi)^2}{\boldsymbol{q}/\pi} \log\left|\frac{\boldsymbol{q}/2\pi + 1}{\boldsymbol{q}/2\pi - 1}\right|\right). \tag{5.3}$$

This leads to an enhanced Pauli paramagnetism (χ_P) by a factor of $(1 - IN(E_F))^{-1}$, which also leads to a dramatic increase of the susceptibility via the Coulomb interaction. More specifically, for the present situation stoichiometric $NbFe_2$ is on the border of a FM instability reflecting a large Stoner factor $S \cong 180$ ($I \cdot N(E_F) = 0.99 \approx 1$) with

$$S = (1 - I \cdot N(E_F))^{-1} \tag{5.4}$$

and high Wilson ratio $R_W \cong 60$ [17] given by

$$R_W = \frac{\chi/\chi_0}{\gamma/\gamma_0}. \tag{5.5}$$

If $\chi_P f(\boldsymbol{q}/2\pi)$ reaches unity, the susceptibility diverges at the wave vector $\boldsymbol{q}$. Then, an oscillatory static magnetization can develop spontaneously

in the sample. Ferromagnetism develops for $\boldsymbol{q} = 0$, antiferromagnetism for $|\boldsymbol{q}| = \pi/a$, otherwise a SDW or spiral structures are expected as a function of $\boldsymbol{q}$.

Stoichiometric $NbFe_2$ is assumed to undergo a transition into a SDW modulated state with a long-wavelength helical or spiral ($\boldsymbol{q} \neq \boldsymbol{0}$) arrangement of Fe spins below a transition temperature $T_N = 10$ K, which is indicated by thermodynamic, transport and specific measurements measurements. Spin-glass transition, superparamagnetism and domain effects are excluded by ac-susceptibility, Arrott-plot and specific heat investigations [17, 18].

This presumed SDW state in $Nb_{1-y}Fe_{2+y}$, $-0.015 \leq y \leq 0.02$, are bounded by a FM phase of Fe-rich $NbFe_2$ and by a QCP for $y_c \cong -0.015$ of Nb-rich $NbFe_2$. This QCP appears to be the origin of a logarithmic Fermi liquid breakdown: the electronic resistivity scaling follows a $T^{3/2}$ power-law and a linear specific heat $C_p/T \propto \log T$ reflects a NFL behavior, which is characteristic for a FM metal [17, 18]. To date, neutron diffraction studies have been unable to directly establish the existence of such spin density wave modulated phase. Therefore, muon spin relaxation experiments are carried out in order to detect the SDW state and to distinguish it from a FM phase.

For this purpose, well-characterized high quality single- and polycrystalline samples of $Nb_{1-y}Fe_{2+y}$ are investigated, which have been characterized previously using Laue diffraction, electrical transport measurements and magnetometry. Tab. 5.1 lists the stoichiometry and the magnetic transition temperatures of all investigated samples. Single crystals were grown by a optical floating zone method utilizing a ultra high vacuum mirror furnace from polycrystalline precursor rods. These polycrystals were prepared from high-purity niobium and iron by radio-frequency induction melting. The samples used in this thesis closely correspond to similar single crystals from the same growth runs, which were characterized and investigated in prior detailed bulk studies [21, 180, 182–184].

sample name	y	T_N	T_C	crystal structure
OFZ28	$y = +0.018$	36	32	single crystalline
B4	$y = +0.0161$	30	22	polycrystalline
OFZ11	$y = 0.000$	12	-	single crystalline
OFZ29	$y = 0.000$	12	-	single crystalline
OFZ12	$y = -0.004$	8	-	single crystalline
C4	$y = -0.0055$	5.3	-	polycrystalline
C5	$y = -0.0117$	-	-	polycrystalline
C2	$y = -0.0190$		3.2	polycrystalline

Tab. 5.1: Overview for all investigated $Nb_{1-y}Fe_{2+y}$ samples: transition temperatures of the SDW (T_N) and FM (T_C) states are determined by thermodynamic studies [182].

5.2 Muon spin relaxation on $Nb_{1-y}Fe_{2+y}$

Since for slightly off-stoichiometric $Nb_{1-y}Fe_{2+y}$ a magnetic phase diagram was proposed that contains ferromagnetic and a presumed SDW phase, the aim of this muon spin relaxation study (μSR) was the determination of a detailed phase diagram by means of a microscopic technique, with a special focus on the assumed SDW state close to quantum critical behavior. If the SDW ordering is identified, it would confirm the theory of Belitz *et al.* and Conduit *et al.* [86, 108]. In recent years, first μSR spectroscopy was performed by M.R. Crook [66] on polycrystalline $Nb_{1-y}Fe_{2+y}$, $-0.04 \leq y \leq 0.04$, in a temperature range of 10 K$\leq T \leq$ 300 K. This data has identified both FM states and a intermediate phase for $-0.02 \leq y \leq 0.02$, which deals with the coexistence of both static and dynamic random fields. This implied a vague magnetic state of an anti-structure of the Fe atoms. Performing similar studies on well-characterized single crystalline and pure polycrystalline samples promises to produce more detailed results with a better resolution.

Therefore, single and polycrystalline samples $Nb_{1-y}Fe_{2+y}$ (Tab. 5.1) were studied in μSR experiments in weak transverse fields, zero fields and in longitudinal fields using the general purpose surface-muon (GPS)

and low temperature facility (LTF) instruments of the Swiss Muon Source at the Paul Scherrer Institut, Villigen, Switzerland.

5.2.1 Weak transverse field μSR studies

Weak transverse field (wTF) μSR experiments on $Nb_{1-y}Fe_{2+y}$ have been carried out in the range of 1.6 and 300 K using an external field of 5 mT applied at an angle of 90° relative to the polarized muon spin. The μSR data provides comprehensive microscopic information about the low temperature magnetic states in $Nb_{1-y}Fe_{2+y}$. Fig. 5.2 displays representative asymmetry spectra of wTF μSR experiments for $Nb_{1-y}Fe_{2+y}$ between 2 and 80 K. At higher temperatures (in the paramagnetic state), the muons precess with the frequency ω in the external field giving rise to an oscillatory asymmetry $A_{\mathrm{TF}}(t)$

$$A_{\mathrm{TF}}(t) = A_0 \cos(\omega t + \phi) \exp(-\frac{1}{2}(\sigma t)^2) \exp(-\lambda_{\mathrm{TF}} t). \tag{5.6}$$

Eq. (5.6) implies a local field distribution caused by nuclear dipoles and an additionally operative electronic relaxation process. Here, A_0 denotes the asymmetry parameter, $\omega = 2\pi f$ the muon frequency with $f \sim 0.65$ MHz, ϕ the phase shift, σ the width of a local magnetic field distribution[1] and λ_{TF} the damping rate.

At temperatures higher than 100 K the muon precession varies because of muon diffusion, an effect not analyzed in detail for the present measurements. At low temperatures, the signals are strongly damped and acquire an additional precession term from local internal fields, see Eqs. (5.7) and (5.8), in ZF μSR fits indicated by red lines in Fig. 5.2. From fits of Eq. (5.6) to the data we obtain a temperature dependence of the wTF asymmetry parameter, which is proportional to the paramagnetic volume fraction. In Fig. 5.3 the temperature dependence of the asymmetry parameter A_0 is plotted. It illustrates the complete loss of asymmetry for the samples with $y \geq -0.0055$, which proves the bulk nature of the magnet-

[1] For the analysis of the temperature dependence σ is fixed for each sample.

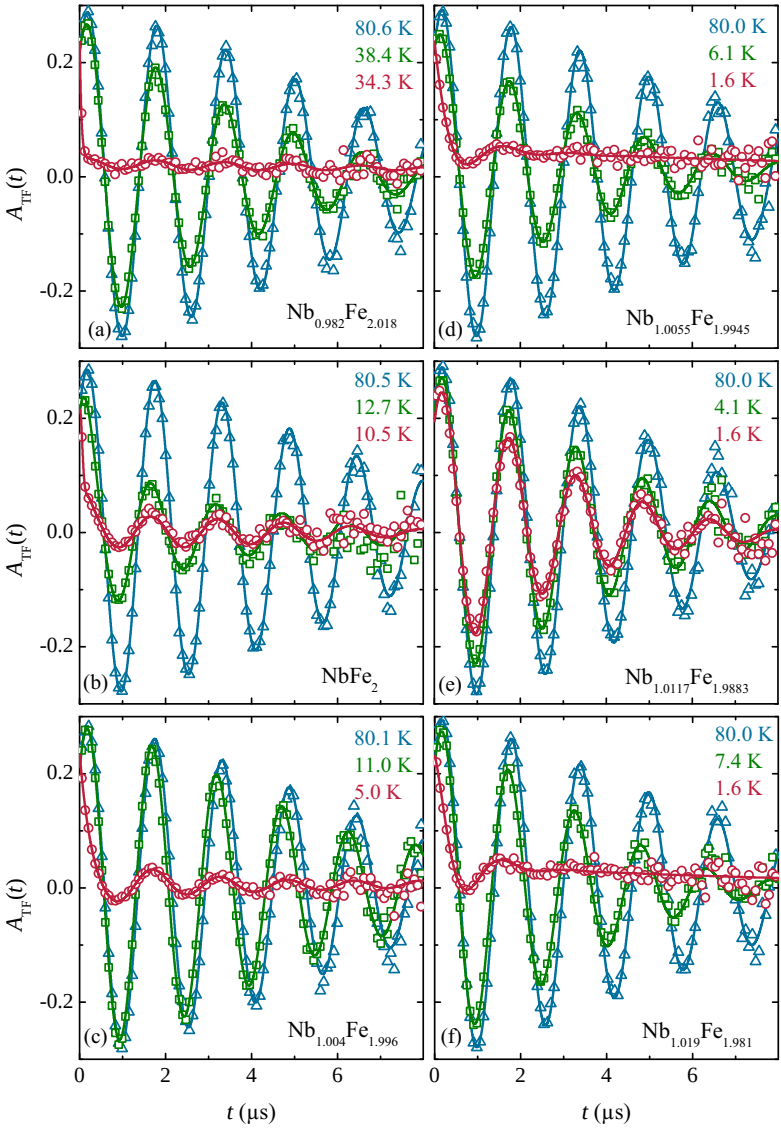

Fig. 5.2: Weak transverse field μSR asymmetry spectra between $1.6 - 80$ K in an external field of 5 mT for $Nb_{1-y}Fe_{2+y}$, $y = +0.018$ (a), 0.0 (b), -0.004 (c), -0.055 (d), -0.0117 (e) and -0.019 (f). Solid lines are fits to the data, for details see text.

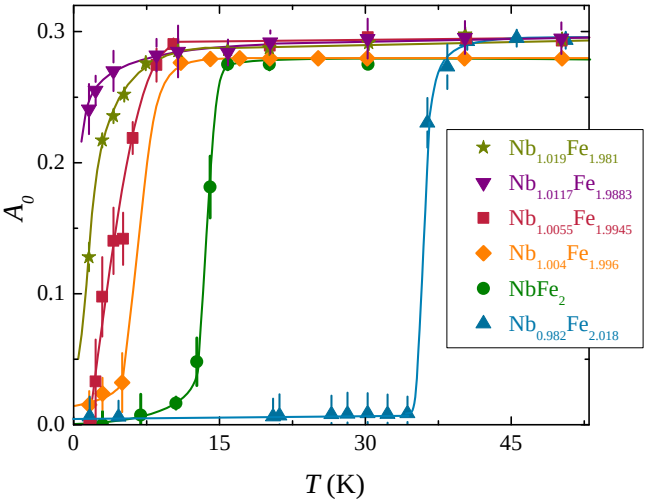

Fig. 5.3: Temperature dependence of the asymmetry parameter A_0 of wTF μSR measurements in $Nb_{1-y}Fe_{2+y}$, $y = -0.019$ (star), -0.0117 (inverse triangle), -0.0055 (cubic), -0.004 (diamond), 0.0 (circle) and $+0.018$ (triangle).

ically ordered phases for these samples at lowest temperatures. Since the muon detects internal magnetic fields, ω shifts and λ_{TF} of Eq. (5.6) diverges at a magnetic phase transition. This is the reason of the beginning magnetic behavior in the asymmetry spectra, while the fitting function of Eq. (5.6) is only valid for the paramagnetic region. The polycrystalline $Nb_{1.0055}Fe_{1.9945}$ seem to suggest a magnetically inhomogeneous sample together with magnetization measurements (cf. section 5.2.2), since the loss of asymmetry are incomplete up to $T \sim 1.7$ K. For the Nb-rich sample $Nb_{1.019}Fe_{1.981}$ a magnetic transition is observed also, although at lowest experimental temperatures of 2 K the asymmetry is not fully lost yet, implying that the magnetically ordered phase does not yet cover all of the sample. In contrast, in quantum critical $Nb_{1.0117}Fe_{1.9883}$ a bulk magnetic transition is not detectable down to temperatures of 0.02 K.

The transition temperatures are determined as the midpoint of the temperature dependent asymmetry parameter A_0 at the transition to 36 K

in $Nb_{0.982}Fe_{2.018}$, 14 K in $NbFe_2$, 8 K for $Nb_{1.004}Fe_{1.996}$, 5 K for $Nb_{1.0055}Fe_{1.9945}$ and 3 K for $Nb_{1.019}Fe_{1.9981}$, in good agreement with bulk studies [17, 18, 180, 182–184]. The evolution of the transition temperatures in context of the sample composition will be discussed later, and will be related to the observed μSR frequencies in zero field measurements and to the size of the ordered magnetic moment for the magnetically ordered states.

5.2.2 Zero field μSR studies

More detailed information, in particular on the magnetically ordered states of $Nb_{1-y}Fe_{2+y}$, is obtained by zero field (ZF) μSR experiments. Fig. 5.4 depicts the asymmetry spectra for temperatures covering the magnetic phase transitions for all samples at a time scale of $8\,\mu$s (for quantum critical $Nb_{1.0117}Fe_{1.9883}$ a temperature similar to the neighboring samples in the phase diagram is plotted). Varying temperatures reveals different asymmetry signatures for the magnetically ordered samples: a strongly damped low temperature magnetic state and a weakly damped high temperature non-magnetic state. Above the critical temperatures, in the paramagnetic range (blue data points/lines in the asymmetry spectra) the data for all samples indicates dynamic nuclear moments, which can be fitted by the non-analytically solvable dynamic Gaussian Kubo-Toyabe-type function (Eq. (3.25)) [128, 129] in zero field with a frequency $\nu = 0$ MHz, a constant Gaussian field relaxation $\sigma \sim 0.3\,\mu s^{-1}$ and a varying hopping rate Γ, which increases with decreasing temperature.

ZF μSR investigations in the magnetically ordered states (green data points/lines in the asymmetry spectra) show strongly damped asymmetry spectra $A_{ZF}(t)$, except for $Nb_{1.0117}Fe_{1.9883}$. Here, at the quantum critical point no long-range ordered magnetism is observed down to temperatures of 1.6 K, in full agreement with the wTF μSR measurements. For further analysis, another approach to interpret the experimental data comes by switching from the time into the frequency domain per numerical Fast Fourier Transformation (FFT) of the asymmetry spectra. Fig. 5.5

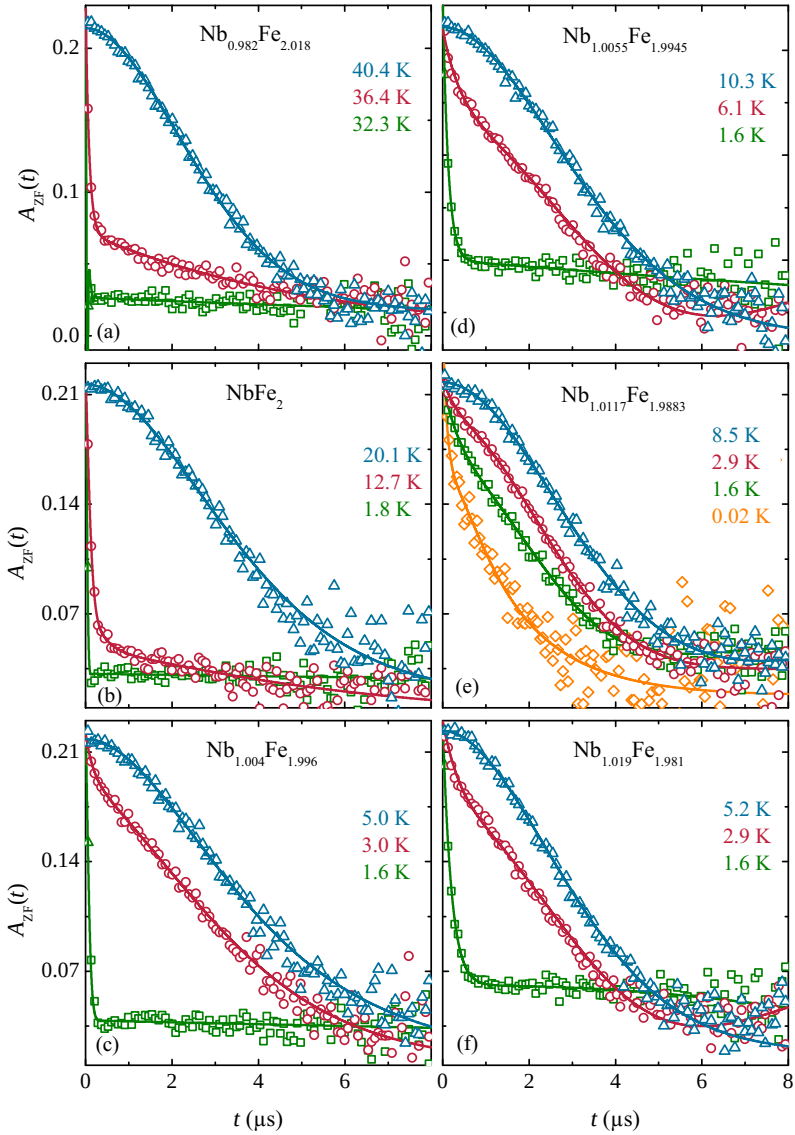

Fig. 5.4: Zero field μSR asymmetry spectra between $1.6 - 40$ K for a time range $t = 8$ μs for $Nb_{1-y}Fe_{2+y}$, $y = +0.018$ (a), 0.0 (b), -0.004 (c), -0.055 (d), -0.0117 (e) and -0.019 (f). Solid lines are fits to the data, for details see text.

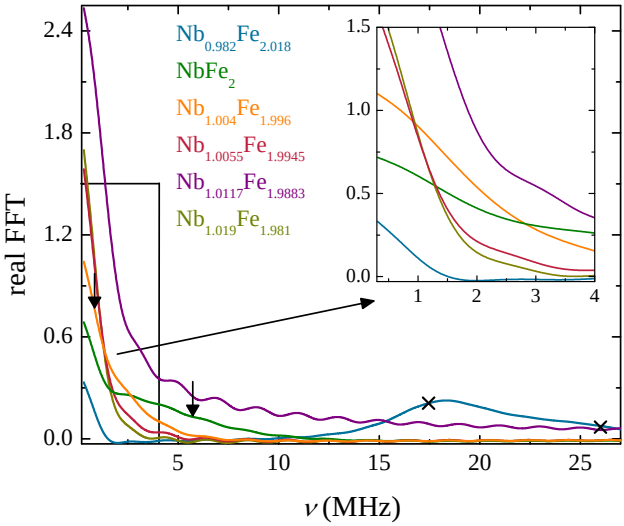

Fig. 5.5: Real part of the amplitude of the Fast Fourier Transformation (FFT) of A_{ZF} for $t \leq 0.5\,\mu$s of $Nb_{1-y}Fe_{2+y}$, $-0.019 \leq y \leq +0.018$, at a temperature of 1.6 K. Arrows and crosses indicate the characteristic frequencies $\Omega_{B/i}$ (SDW/FM), see Eqs. (5.8) and (5.7).

reveals a first overview of the real part of the FFT carried out on the muon relaxation asymmetry spectra at low temperatures (1.6 K). In this depiction, $Nb_{0.982}Fe_{2.018}$ exhibits as the only sample a broad maximum at finite frequency ν, consistent with ferro- or ferrimagnetic ordering from bulk magnetometry [17, 181].[2] Both, $NbFe_2$ and $Nb_{1.004}Fe_{1.996}$, have a broad maximum around zero frequency. This is, on top of the sample holder contribution, consistent with a spin density wave state that produces a static field distribution around zero field. These maxima become more narrow for $Nb_{1.0055}Fe_{1.9945}$ and $Nb_{1.019}Fe_{1.981}$, reflecting the very weak magnetic states of these compositions close to the QCP. At the QCP ($Nb_{1.0117}Fe_{1.9883}$) with an experimental error of 0.5 MHz the muon relaxation frequencies are determined to be zero with a deviation in the FFT amplitude, in agreement with the magnetic phase diagram from bulk mea-

[2]The broad anomaly around zero frequency with a FFT amplitude of about 0.3 stems from the sample holder.

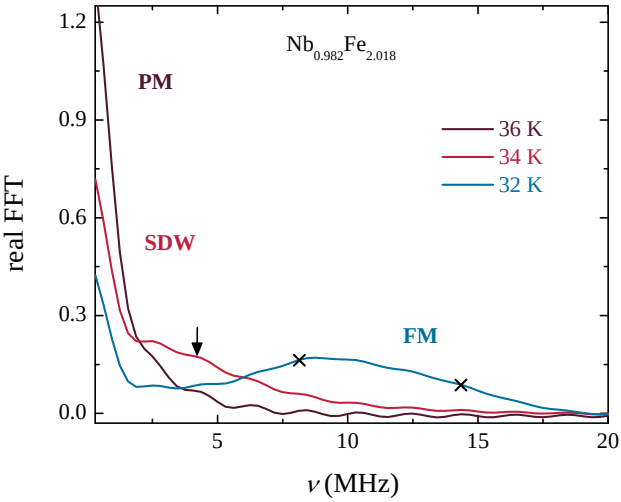

Fig. 5.6: Real part of the amplitude of the Fast Fourier Transformation (FFT) of A_{ZF} of $\mathrm{Nb}_{0.982}\mathrm{Fe}_{1.018}$ at temperatures $T = 36, 34, 32$ K. Arrows and crosses indicate the characteristic frequencies $\Omega_{B/i}$ (SDW/FM), see Eqs. (5.8) and (5.7).

surements (Fig. 5.1) – thus, magnetical ordering is fully suppressed.

Detailed analysis of the asymmetry spectra of the ZF μSR for $t \leq 0.2$ μs (Fig. 5.7) observes the different nature of muon relaxation in the different magnetic phases of $\mathrm{Nb}_{1-y}\mathrm{Fe}_{2+y}$ as well as the FFT analysis. For $\mathrm{Nb}_{0.982}\mathrm{Fe}_{2.018}$ a spontaneous muon rotation signature is detected at temperatures below 32 K (green data points/lines in the asymmetry spectra in Fig. 5.7 (a)), consistent with ferro- or ferrimagnetic ordering. This behavior can be analyzed in terms of two distinct muon sites with precession frequencies Ω_i caused by the local internal magnetic field according to

$$A_{\mathrm{FM}} = \sum_{i=1}^{2} a_i \left[\alpha_i \cos\left(\Omega_i t\right) \exp(-\lambda_{\mathrm{T},i} t) + (1-\alpha_i) \exp(-\lambda_{\mathrm{L},i} t)\right]. \quad (5.7)$$

The asymmetry parameter a_i is associated with muon site i, α_i denotes the fraction of transverse field components of the field distribution with

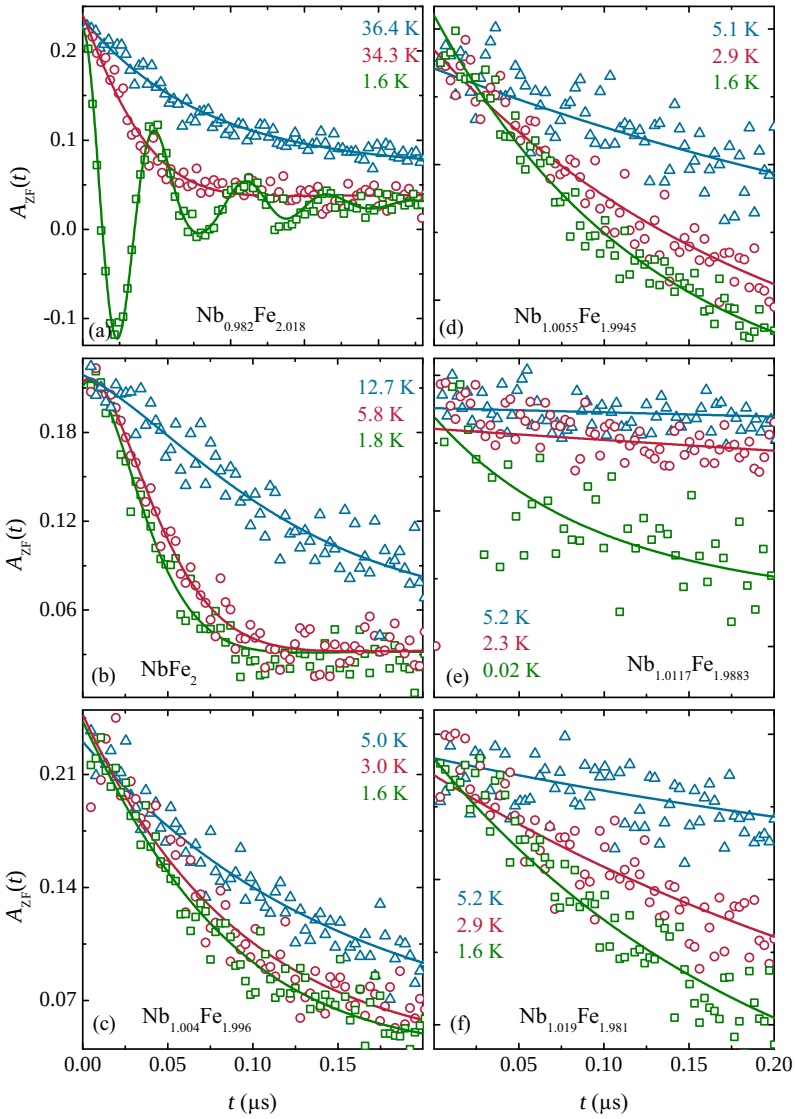

Fig. 5.7: Zero field μSR asymmetry spectra for $t \leq 0.2$ μs between $1.6 - 36$ K for $Nb_{1-y}Fe_{2+y}$, $y = +0.018$ (a), 0.0 (b), -0.004 (c), -0.055 (d), -0.0117 (e) and -0.019 (f). Solid lines are fits to the data, for details see text.

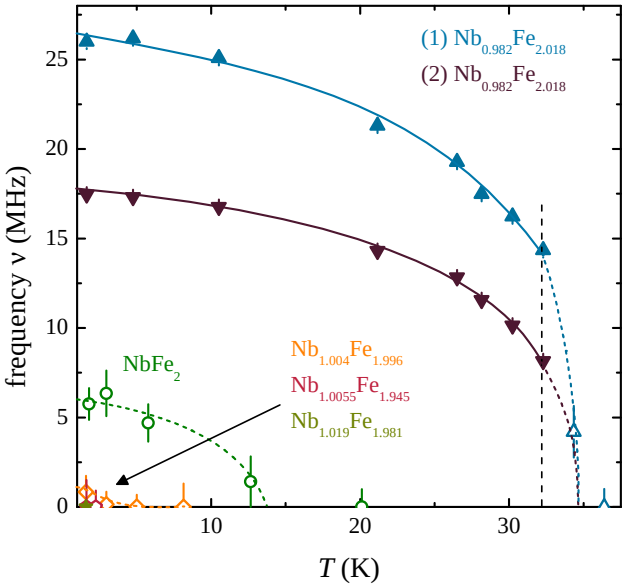

Fig. 5.8: Temperature dependence of μSR frequencies of $Nb_{1-y}Fe_{2+y}$, $y = +0.018$ (triangle), 0.0 (circle), -0.004 (diamond), -0.0055 (pentagon) and -0.019 (star). The closed symbols denote the frequencies of the FM state, the open ones the frequencies of the SDW state; solid and dashed lines are guides to the eye. To indicate the SDW phase transition in $Nb_{0.982}Fe_{2.018}$ a dashed line is drawn.

respect to the initial muon spin which gives rise to a precession. It remains nearly constant as a function of temperature indicating that also the direction of Fe moments stays the same. $\lambda_{T/L}$ define the transverse/longitudinal damping rates, which are almost constant with values of $\lambda_{T,i} \sim 25/20\ \mu s^{-1}$ and $\lambda_{L,i}$ of $1/0\ \mu s^{-1}$. While $\lambda_{T/L}$ diverge at the phase transitions. The characteristic muon relaxation frequencies Ω_i are indicated by crosses in Fig. 5.5 and Fig. 5.6, and fits to Eq. (5.7) are depicted as lines in Fig. 5.4 and Fig. 5.7. The temperature dependence of the precession frequencies Ω_i, are depicted as solid lines in Fig. 5.8, reflects the evolution of the bulk magnetization.

Also, based on magnetization experiments, the magnetic phase diagram

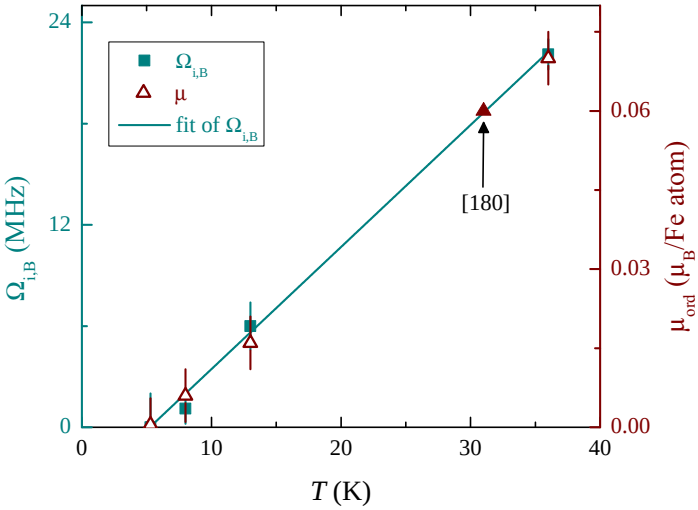

Fig. 5.9: The dependence of the precession frequency $\Omega_{i,B}(T)$ on the transition temperature for $Nb_{1-y}Fe_{2+y}$,$-0.019 \leq y \leq +0.018$ scales for the SDW and FM moment μ in the same way. μ are estimated by a linear evolution of $\Omega_{i,B}$ and the magnetic moment from Ref. [180] as a reference point (filled red triangle), for details see text.

(Fig. 5.1) has been reported that the Nb-rich $Nb_{1.019}Fe_{1.981}$ is ferromagnetic, similar to the Fe-rich $Nb_{0.982}Fe_{2.018}$. In contrast to the spontaneous muon rotation of the Fe-rich material, in Nb-rich $Nb_{1.019}Fe_{1.981}$ only a strongly damped asymmetry signal is observed in the magnetically ordered phase (Fig. 5.7 (f)). This difference might indicate another kind of (ferro-)magnetic order or may be due to the very small magnetic moments, which should scale in first approximation with the transition temperatures $T_C \sim 32$ K in $Nb_{0.982}Fe_{2.018}$ and 3 K in $Nb_{1.019}Fe_{1.981}$. With the size of the ordered moment for $Nb_{0.982}Fe_{2.018}$ reported to $0.06\,\mu_B$/Fe atom [180], the ordered moment for $Nb_{1.019}Fe_{1.981}$ should be of the order of a few 1/1000th of μ_B per Fe atom. After all, however, these experiments so far do not provide a definite result – further measurements of Nb-rich samples will have to be carried out in future.

According to the phase diagram from Ref. [17] (see Fig. 5.1) for

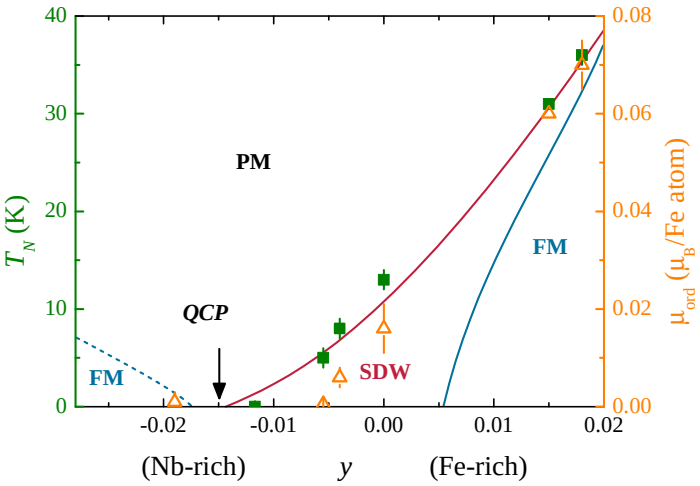

Fig. 5.10: The evolution of the transition temperature T_N (green squares) and magnetic moments μ_{ord} (orange triangles) scales with their compositions y for $Nb_{1-y}Fe_{2+y}$,$-0.016 \leq y \leq +0.016$ close to the QCP in a different way.

$Nb_{0.982}Fe_{2.018}$ a spin density wave phase is claimed to exist in a narrow temperature range between $T_C \sim 32$ K and $T_N \sim 36$ K. This different type of spin structure is also reflected in the real part of the FFT (Fig. 5.6), where the distinct maximum at finite frequency is replaced by a distribution around zero frequency. For all other magnetically ordered samples of $Nb_{1-y}Fe_{2+y}$ a similar response exists for frequencies centered very near to zero in the ordered phases (Fig. 5.5). It implies that this behavior represents a common spin density wave signature of the modulated magnetic phase. Therefore, and in view of the various bulk magnetic studies on $Nb_{1-y}Fe_{2+y}$, the overdamped asymmetry signal is ascribed to a wide field distribution of local magnetic fields caused by a SDW state. Following Refs. [131, 132] the local field distribution is parametrized with an internal Bessel function according to

$$A_{\mathrm{SDW}} = a\left[\alpha j_0\left(\Omega_{\mathrm{B}} t + \phi\right)\exp(-\Lambda_{\mathrm{T}} t) + (1-\alpha)\exp(-\Lambda_{\mathrm{L}} t)\right], \quad (5.8)$$

with asymmetry parameter a, fraction α, Bessel function j_0 and transversal/longitudinal damping rate $\Lambda_{\mathrm{T/L}}$. Here, the argument of the Bessel function contains the maximal frequency Ω_{B} of the SDW frequency distribution (corresponding to the maximal local field). The values Ω_B are indicated by arrows in Fig. 5.5 and Fig. 5.6. The constant α exhibits a larger transversal part than the longitudinal one for all samples. At the phase transition α, Λ_{T} and Λ_{L}diverge, while in the magnetic state this parameters are nearly constant.

Because the μSR frequencies Ω_i and Ω_B depend on the size of the ordered moment for the FM and SDW state, respectively, their evolution with temperature and sample composition is of particular interest. Fig. 5.8 depicts these μSR frequencies, which decrease with increasing Nb substitution. On closer examination, we observe for $Nb_{1.004}Fe_{1.996}$ a slow transition into the SDW phase. At the transition temperature $T_N \sim 8$ K the asymmetry parameter indicates that only a part of the sample volume ($\sim 35\,\%$) is already ordered, in good agreement with bulk and wTF μSR data. Frequencies with Nb concentration of $y = -0.0055$ and -0.019 are close to zero and do not show the typical temperature dependent behavior of magnetic phase transitions. Nevertheless, the magnetically ordered states are clearly visible in the strongly damped asymmetry functions, in the real part of the FFT and are analyzable with fitting functions of Eqs. (5.7) and (5.8). Moreover, for $Nb_{0.982}Fe_{2.018}$ the data points at ~ 34 K and ~ 36 K (open triangles in the SDW state) can be fitted using Eq. (5.8).

In stoichiometric $NbFe_2$ the temperature evolution of the frequency $\Omega_B(T)$ is consistent with a second order phase transition at $T_N \sim 13$ K, in good agreement with the results of bulk and wTF μSR data. Moreover, $\Omega_B(T = 0) \simeq 6$ MHz is larger than the value for $Nb_{0.982}Fe_{2.018}$ at 34 K, $\Omega_B(T = 0) \simeq 4$ MHz (open triangle in Fig. 5.8). If the SDW amplitude scales with Ω_B in the same way as the FM moment scales with Ω_i, then bulk measurements, which give about $0.06\,\mu_B$/Fe atom in $Nb_{0.985}Fe_{2.015}$ [180], suggest that at low temperatures the SDW amplitude is of the order of $0.01 - 0.02\,\mu_B$/Fe atom in $NbFe_2$, about $6 \cdot 10^{-3}\,\mu_B$/Fe atom in

$Nb_{1.004}Fe_{1.996}$ and about $5 \cdot 10^{-4}\,\mu_B$/Fe atom in $Nb_{1.0055}Fe_{1.9945}$. This rapid drop of the size of the magnetic moment by almost two orders of magnitude with varying composition y, when T_N appears to be reduced only by a factor six, is rather surprising (see Fig. 5.9 for a plot of the evolution of the moment size with transition temperatures).

Extrapolating the evolution of the magnetic moments with their compositions (see Fig. 5.10), the $\mu_{ord}(y)$-data from our μSR-study would imply a fully suppressed magnetic moment at a composition $y_c \sim -0.006 \pm 0.001$ (analogous to $y_c(T_N) \sim -0.009 \pm 0.002$), which is distinctly different from the value $y_c = -0.015$ obtained from bulk studies. It raises the question about the nature of the magnetically ordered phase in the quantum critical range $-0.006 \leq y \leq y_c$.

Quantum critical behavior in $Nb_{1.0117}Fe_{1.9883}$

Within the series of experiments presented here, for the first time a quantum critical sample, $Nb_{1.0117}Fe_{1.9883}$, is investigated by μSR in the GPS and LTF facilities down to temperatures of 0.02 K. As pointed out in the preceeding section, in this study no distinct indication for long-range magnetic ordering is observed, in full agreement with bulk measurements. The temperature dependence of the inverse magnetic susceptibility $\chi^{-1}(T)$ shows deviations from Curie-Weiss behavior below a temperature of 4.4 K (Fig. 5.11 (b)), which might reflect weak magnetic ordering of a part of the sample. Also, the asymmetry parameter of wTF μSR measurements, which indicate the paramagnetic volume fraction, shows an initial decrease (Fig. 5.3). In contrast to the wTF μSR data for other compositions in $Nb_{1-y}Fe_{2+y}$ the quantum critical $Nb_{1.0117}Fe_{1.9883}$ has to be analyzed by

$$A_{\mathrm{QCP,wTF}}(t) = A_{\mathrm{TF},1}(t) + A_{\mathrm{TF},2}(t). \tag{5.9}$$

Thus, in addition to the muon precession observed in the other samples $Nb_{1-y}Fe_{2+y}$ an additional signal exist, which is described as well by an oscillatory asymmetry function A_{TF} (Eq. (5.6)). Most likely, it simply re-

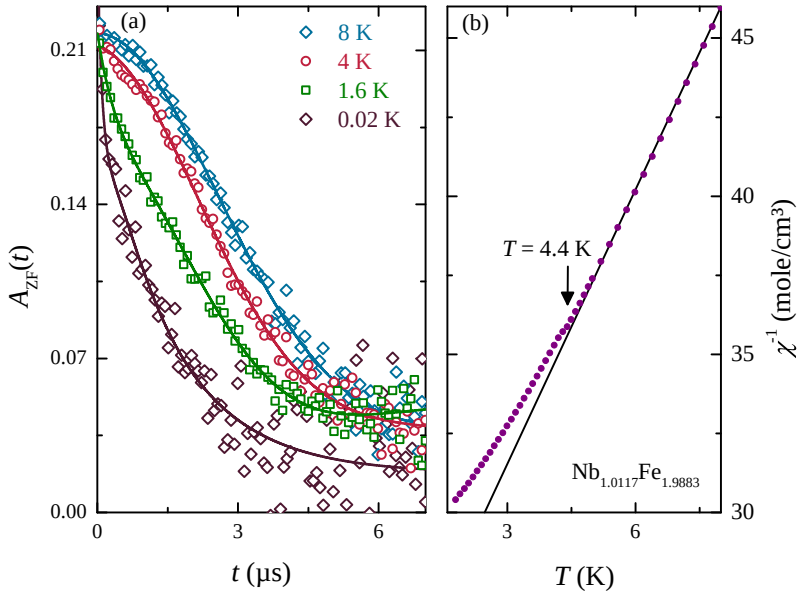

Fig. 5.11: ZF μSR asymmetry spectra (a) and inverse susceptibility $\chi^{-1}(T)$ in a magnetic field of $B = 1$ T (b) at temperatures $0.02\ \text{K} \leq T \leq 8\ \text{K}$ for $Nb_{1.0117}Fe_{1.9883}$.

flects two different muon sites in the sample. Also, for the other measured samples there should be two muon sites, but here only a very limited set of data has been taken in the paramagnetic regime, and those high temperature data sets could already be fitted using only one function $A_{\rm TF}$.

Next, Fig. 5.11 (a) depicts the asymmetry spectra of ZF μSR experiments utilizing the GPS and LTF facilities for the quantum critical sample $Nb_{1.0117}Fe_{1.9883}$. The asymmetry spectra of the LTF facility are rather noisy and include a signal from a dominant silver background from the sample holder. By comparing the ZF μSR measurements from both facilities, the LTF asymmetry spectra can be adjusted to correct for the silver background. Again, the asymmetry spectra of the ZF μSR exhibits an additional dynamic fluctuation component, which is fitted with an extra dynamic Gaussian Kubo-Toyabe-type function, $A_{\rm dyn,2}(t)$ (Eq. (3.25)).

Similar to the wTF measurements, the use of two dynamic contributions to the asymmetry most likely reflects the presence of two muon sites in $NbFe_2$.

In addition, below a temperature of 8 K a weakly damped signal is observed, which contains in a strong decay at the early time scale ($t \leq 0.4\,\mu$s). This fast decrease is parametrized by an additional exponential function. Thus, the ZF μSR spectra of $Nb_{1.0117}Fe_{1.9883}$ can be described by

$$A_{\mathrm{QCP,ZF}}(t) = A_{\mathrm{dyn},1}(t) + A_{\mathrm{dyn},2}(t) + \exp(-\lambda t). \tag{5.10}$$

Because of the zero field measurements the precession frequencies are $\nu_1/\nu_2 = 0$ MHz, the field distributions are fixed to $\sigma_1 = 0.237\,\mu\mathrm{s}^{-1}$ and $\sigma_2 = 0.369\,\mu\mathrm{s}^{-1}$, the fluctuation frequency Γ_1 increases up to 1.2 MHz with decreasing temperatures, $\Gamma_2 \sim 0$ MHz and the damping rate for fast fluctuations λ rises also up to $4.5\,\mu\mathrm{s}^{-1}$. Thus, in the quantum critical regime of $NbFe_2$ there are spin fluctuations which occur on different time scale.

Altogether, the μSR study on $NbFe_2$ in the quantum critical regime reveals qualitatively new insights, as the material behavior deviates from the long-range ordered samples. For $Nb_{1.0117}Fe_{1.9883}$ additional fluctuations on at least two different time scales are observed and might be linked to the NFL behavior.

5.2.3 Longitudinal field μSR studies

Longitudinal field (LF) μSR experiments were performed to clarify the nature of the local magnetic fields, i.e., whether these are static or dynamic. Exemplary, Fig. 5.12(a) and Fig. 5.12(b) depict the asymmetry spectra for $Nb_{1.004}Fe_{1.996}$ at 15 K ($viz.$, above the ordered phase) and quantum critical $Nb_{1.0117}Fe_{1.9883}$ at 1.6 K, respectively, with varying magnetic fields ($0 - 100$ mT) applied along the initial direction of the muon polarization. In both samples small magnetic fields completely decouple the muon spin – for $Nb_{1.004}Fe_{1.996}$ at 5 mT and for $Nb_{1.0117}Fe_{1.9883}$ at 100 mT. For the

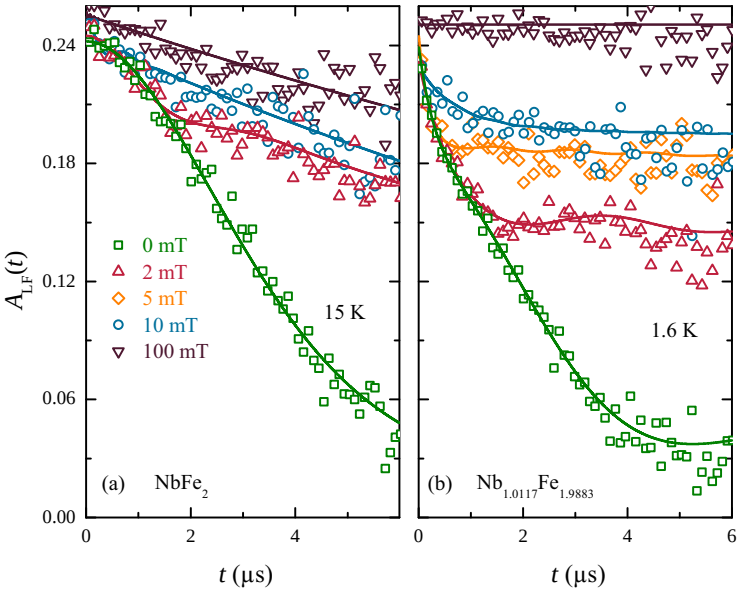

Fig. 5.12: Longitudinal field μSR asymmetry spectra for $Nb_{1.004}Fe_{1.996}$ (a) and $Nb_{1.0117}Fe_{1.9883}$ (b) under different longitudinal fields. Solid lines are fits to the data, for details see text.

former sample, already smallest fields of 2 mT lead to a partial suppression of static internal fields. Thus, for this sample static nuclear fields can be easily decoupled with applied fields, while in $Nb_{1.0117}Fe_{1.9883}$ low frequency fluctuating fields are present, consistent with the physical behavior in this quantum critical regime. In the static case a characteristic Kubo-Toyabe shape is displayed, whereas dynamic fluctuations remains a linear asymmetry function. The fits were generated by Eq. (3.25) for $Nb_{1.004}Fe_{1.996}$ and Eq. (5.10) for $Nb_{1.0117}Fe_{1.9883}$ with increasing fluctuation frequency Γ and λ in the case of $Nb_{1.0117}Fe_{1.9883}$.

Below the transition temperatures ($T < T_N$) LF μSR observe the muon spin relaxation of electronic local magnetic fields in the sample, as depicted for $Nb_{1.004}Fe_{1.996}$ in Fig. 5.13, respectively. For weak longitudinal fields applied along the initial direction of the muon polarization

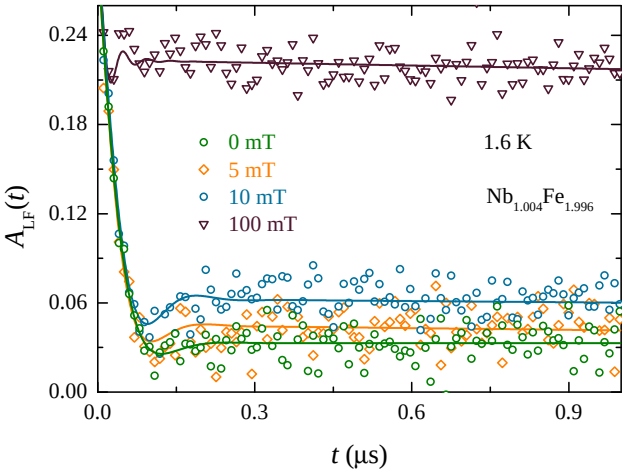

Fig. 5.13: Longitudinal field μSR asymmetry spectra for $Nb_{1.004}Fe_{1.996}$ under different longitudinal fields in the magnetical regime at $T = 1.6$ K. Solid lines are fits to the data, for details see text.

($B \leq 10$ mT) the absorptions spectra describe the SDW phase (see section 5.2.2), in consequences of the pronounced magnetic ground state. Only for magnetic fields of 100 mT the muon spin completely decouples.

All in all, the proposed magnetic phase diagram (Fig. 5.1) has been verified in our μSR study. TF and ZF μSR depolarization spectra clearly indicate in the temperature evolution of the experimental damped asymmetry functions the transition from paramagnetic into magnetically ordered states. For smallest time scales ($t \leq 0.3\,\mu$s) Fe-rich $Nb_{0.982}Fe_{2.0183}$ indeed exhibits a μSR-signal with an oscillating damped asymmetry signal in contrast to all other analyzed samples (Fig. 5.7). This clear difference in the μSR-signature may imply, in accordance with bulk measurements, ferromagnetic or ferrimagnetic ordering for this sample. Such behavior would have to be expected as well for the Nb-rich $Nb_{1.019}Fe_{1.981}$ according to the proposed FM properties from bulk measurements. Yet, this is not the case, the asymmetry spectra, possibly as a consequence of very

small magnetically ordered moments, displays only a damped signal, similar to $Nb_{1-y}Fe_{2+y}$, $-0.0055 \leq y \leq 0.0$. These damped asymmetry spectra for Fe substitution of $-0.0055 \leq y \leq 0.0$ in $Nb_{1-y}Fe_{2+y}$ are ascribed to a wide field distribution of local magnetic fields. These properties are caused by a SDW modulated state in accordance with previous studies [17–19, 179, 180].

A special position in our study takes $Nb_{1.0117}Fe_{1.9883}$, where no evidence of bulk magnetic ordering can be observed in the μSR depolarization. Only the asymmetry parameter of TF μSR measurements reveals a beginning decrease at lowest temperatures, which might indicate the onset of magnetic ordering in some segments of the sample. The asymmetry spectra of ZF μSR shows an additional exponentially damped signal on a short time scale, as compared to $Nb_{1-y}Fe_{2+y}$, $-0.0055 \leq y \leq 0.0$. Furthermore, the comparison of the real part of the FFT carried out on the muon relaxation asymmetry spectra of the quantum critical sample shows again a different behavior than for the other samples $Nb_{1-y}Fe_{2+y}$. In contrast, we observe a broadened maximum in the FFT around zero frequency, which possibly reflects the presence of local fluctuating fields for wide field and time ranges.

5.3 Mössbauer measurements on $Nb_{1-y}Fe_{2+y}$

In addition to the μSR-studies, Mössbauer spectroscopy experiments are performed on Fe-rich powder $Nb_{0.984}Fe_{2.016}$ between 4 K and 90 K using a conventional Mössbauer set-up. This study yields complementary information of the nature of the magnetic phases. For the material, the transition temperatures were determined independently to $T_C \sim 24$ K and $T_N \sim 30$ K via magnetization. In Fig. 5.14, as representative examples the Mössbauer absorption spectra are plotted in the paramagnetic phase at 90 K (a), in the spin density wave (SDW) modulated phase at 28 K (b) and in the ferromagnetic phase at 8 K (c).

At high temperatures the resonance pattern reveals a doublet structure typ-

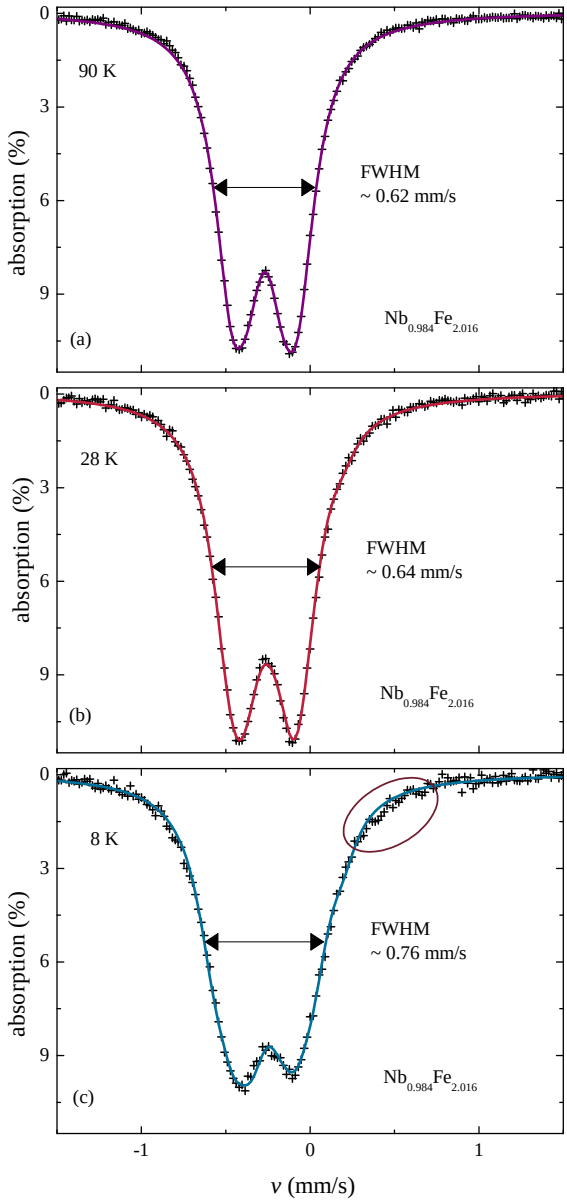

Fig. 5.14: Mössbauer absorption spectra of $Nb_{0.984}Fe_{2.016}$ at 90 K (a), 28 K (b) and 8 K (c). The full lines represent the fit used in the data analysis, the marker denotes an additional weak structure as discussed in the text.

ical for nuclear electric quadrupole interaction. For the fit we take into account two Fe sites, *i.e.,* Fe(*6h*) and Fe(*2a*), in a ratio of $3:1$ in agreement with the structure of the C14 Laves systems, with a quadrupole splitting of about $e^2qQ/2 \sim -0.19$ mm/s and 0.38 mm/s for the two sites. Upon lowering the temperature below T_N the onset of magnetic hyperfine splitting at the Fe sites becomes visible from a broadening of the resonance pattern. At lowest temperatures the line broadening becomes stronger with an asymmetric quadrupole splitting. Furthermore, additional weak structure is observed on the right flank of the Mössbauer absorption spectra (see marker in Fig. 5.14), which present an additionally kink in the flank of the Mössbauer absorptions spectra. Possibly, this might be a texture in the powdered sample.

Altogether, our data indicates a distinct magnetic phase transition in $Nb_{0.984}Fe_{2.016}$ for $T \leq 28$ K. In contrast to the μSR measurements, where a SDW modulated state and one with a ferro- or ferrimagnetic ordering is observed, Mössbauer experiments do not allow such a distinction. The SDW state, as identified by μSR experiments, shows only a weak line broadening without an asymmetric quadrupole splitting in the Mössbauer absorptions spectra at $T = 28$ K, allowing no further conclusions on the symmetry of the ordered state.

Hence, a detailed study of the magnetic structures is not possible, because of the small Zeeman splitting from magnetic moments in a range of some tenth of a μ_B per Fe atom [18, 21]. With the two distinct Fe sites which each produce a multitude of absorption lines from the superposition of quadrupole and magnetic hyperfine splitting, fit parameter interdependency is too high as to produce a unique set of fit parameters to account for the experimental data. The line broadening, however, can be parametrized by determining the line width of the absorption spectra as full width at half maximum FWHM as indicated in the Fig. 5.14. From this procedure, we establish the temperature dependence of the FWHM in the Fig. 5.15. From this plot, as indicated, we can identify a paramagnetic and another magnetic phase (for $T \leq 28$ K) in good agreement with bulk studies

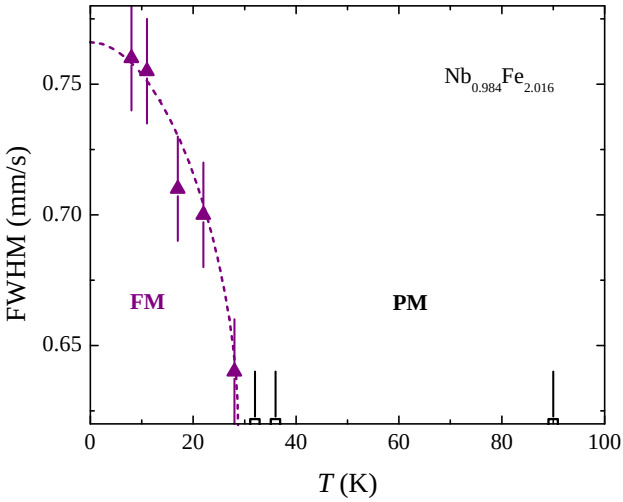

Fig. 5.15: Temperature dependence of the parametrized line broadening as full width half maximum (FWHM) data for Fe-rich powdered $Nb_{0.984}Fe_{2.016}$ with the paramagnetic (PM) and ferromagnetic (FM) phases.

[17, 18, 180, 182–184]. A second phase transition into the spin density wave modulated phase, which is proposed to occur for $T_N \sim 30$ K, can not be detected as result of the very low magnetic moments. Given these limitations in analyzing these Mössbauer data, additional Mössbauer experiments in applied magnetic fields of a few Tesla might be a possible solution.

Further, from the full width at half maximum FWHM, the magnetic hyperfine field at the Fe ions can be estimated to be less than 2 T, which in turn corresponds to an upper limit of the ordered magnetic moment of about $0.15\,\mu_B$/Fe atom from scaling to metallic Fe. This is consistent with the net moment of $0.06\,\mu_B$/Fe atom [180] inferred from bulk magnetometry. These findings contradict the suggestion based on Compton scattering at elevated magnetic fields [181] that Fe-rich $Nb_{0.985}Fe_{2.015}$ is ferrimagnetic, with magnetic moments of $0.4\,\mu_B$ ($-0.6\,\mu_B$) on the Fe (*6h*) (Fe (*2a*)) site. These moments on the Fe atoms imply magnetic hyper-

fine fields of greater or equal to 6 T (*i.e.*, in addition a total line broadening of 1.15 mm/s at FWHM). Hence, our observations using Mössbauer spectroscopy prove the existence of a weakly ferromagnetic phase in $Nb_{0.984}Fe_{2.016}$ and exclude a ferrimagnetic spin arrangement below T_C. The resolution of this discrepancy requires further investigation, but it may be attributed to the larger energy window probed by Compton scattering, which could cause large, slowly fluctuating moments to appear to be static.

5.4 High magnetic fields on $NbFe_2$

In recent years, one concept to address the physical properties of materials close to quantum criticality is that of multiple energy scales controlling the behavior of the material at the quantum critical point. For instance, this approach was applied to the f-electron intermetallic $YbRh_2Si_2$ [11, 68, 185]. A priori, at present, there are no simple arguments to predict if for a given material such a scenario might be applicable. In this situation, one can only test experimentally such a possibility. For $NbFe_2$, given the unusual behavior observed in the μSR spectra at the quantum critical point, it seems worthwhile to perform such an experimental check. Therefore, we have carried out a high magnetic field study on single crystalline stoichiometric $NbFe_2$ (sample number: OFZ29) by means of magnetization and resistivity experiments.

The experimental determination of the magnetization and resistivity has been performed in pulsed high magnetic fields at the Laboratoire National des Champs Magnétiques Intenses (LNCMI) in Toulouse, France. Measurements of the magnetization in pulsed magnetic fields are carried out by determining the magnetic induction in a pick-up coil system surrounding the sample, which is located inside the borehole of the external magnet and therefor limits the sample dimensions. A large field noise can be reduced due to a carefully positioning of the sample in the center of the pick-up coil system at the homogeneity area of the pulsed fields. The electrical resistivity has been studied utilizing a spot-welded ac four-point method. Magne-

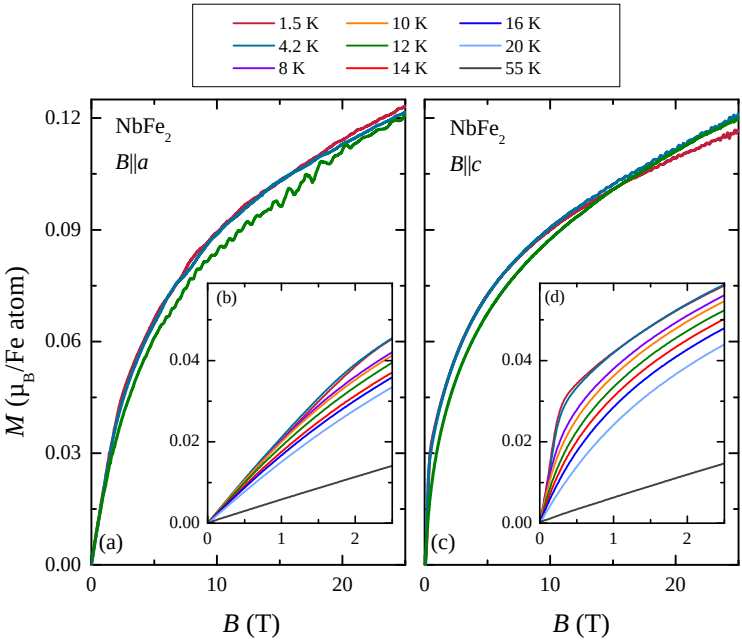

Fig. 5.16: High field magnetization of $NbFe_2$ for temperatures of 1.5, 4.2 and 12 K, with the external field up to 25 T aligned along the a axis (a) and c axis (c). Insets (b) and (d) display the magnetization up to 2.5 T in a temperature range of $1.5 - 55$ K.

tization and resistivity of well-characterized high quality single crystalline $NbFe_2$ have been investigated in external field up to 30 T aligned along the a- and c-axis in the temperature range of $1.4 - 55$ K, which were characterized extensively by bulk experiments of the Refs. [180, 182–184]. Correspondingly, the complete coil arrangement has been placed inside a ^{4}He cryostat.

Fig. 5.16 depicts the high field magnetization $M(B)$ for $NbFe_2$ as function of an external field up to 25 T aligned along the a- and c-axis with an equivalent trend at each temperature in a range of $1.5 - 55$ K; observed anomalies at high fields reflect experimental noise. In high magnetic fields, the magnetization of the PM and SDW modulated state

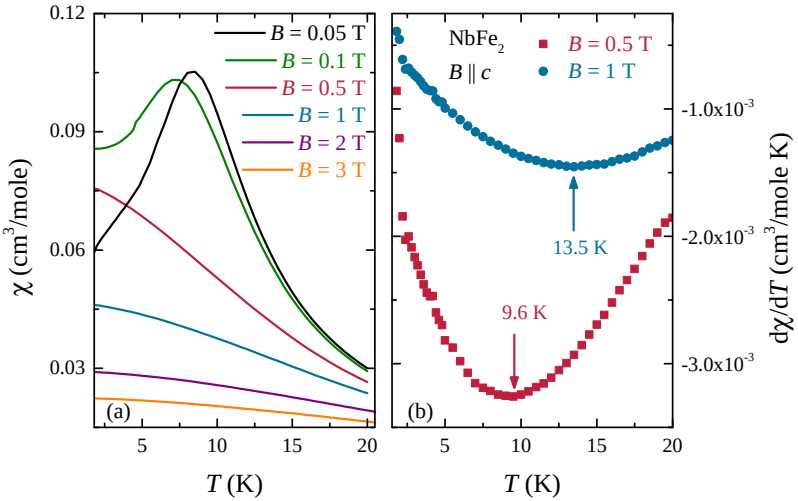

Fig. 5.17: (a) Temperature dependence of susceptibility χ for $NbFe_2$ for applied magnetic fields along the c-axis and (b) the derivatives $d\chi/dT$ versus T are displayed for $B = 0.5$ T and 1 T. The arrows mark the minima, corresponding to the energy scale $T^*_\chi(B)$; for details see text.

($T_N = 12$ K) does almost not change, in agreement with the study of polycrystalline samples in Ref. [182]. In contrast, for low magnetic fields ($B \leq 2.5$ T) a strong anisotropy in $M(B)$ occurs along and perpendicular to applied magnetic fields, see the insets of Fig. 5.16. At lowest temperatures ($T \leq 4.2$ K) the magnetic fields along the c-axis exhibit a distinct kink at a critical field B_c of about 0.4 T in good agreement with Refs. [17–19, 21]. This saturation point corresponds to a maximum in the susceptibility for temperatures close to a ferromagnetic instability, $T \to T_C$, as we will see in Figs. 5.17 and 5.18. For increasing temperatures, $T >> T_C$, this kink vanishes as an inflection point of the field-dependent magnetization $M(B)$ and moves to higher magnetic fields as a result of decreasing fluctuations close to a ferromagnetic instability.

In contrast to other weakly ferromagnetic systems with a first-order phase transition from PM-to-FM state, i.e. $ZrZn_2$ [88] and UGe_2 [186], the PM-to-SDW transition was found to be of second order in agreement to

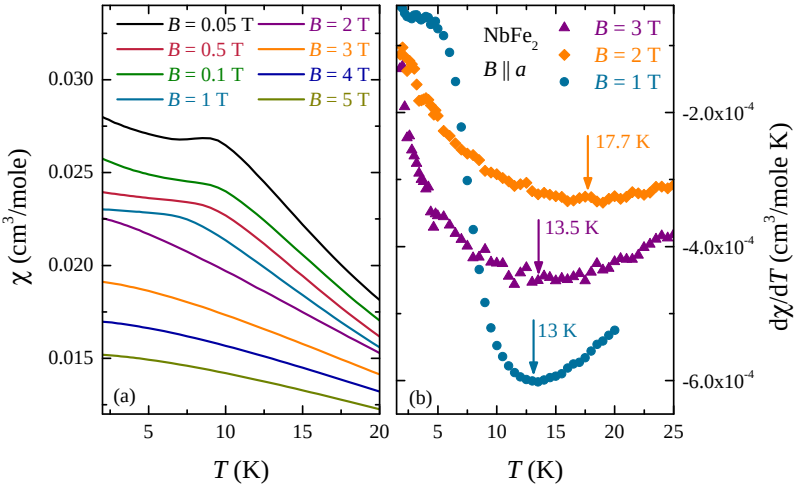

Fig. 5.18: (a) Temperature dependence of susceptibility χ of $NbFe_2$ for applied magnetic fields along the a-axis and (b) the derivatives $\mathrm{d}\chi/\mathrm{d}T$ versus T are displayed for $B = 1$ T, 2 T and 3 T. The arrows mark the minima, corresponding to the energy scale $T^*_\chi(B)$.

detailed bulk measurements of Moroni-Klementowicz *et al.* [18], even though $NbFe_2$ is rather close to a ferromagnetic state (cf. Fig. 5.1) [187].

Next, the field dependence of the electrical resistivity ρ along the c-axis is shown in Fig. 5.19 up to 16 T (a) and 30 T (b) for various temperatures. Below the SDW phase transition of stoichiometric $NbFe_2$ ($T_N = 12$ K) the electrical resistivity immediately drops for small magnetic fields, while above T_N (orange line) the slope of ρ at zero magnetic field is approximately zero. In addition, a broadened minimum in ρ is observed, which shifts to lower magnetic fields B with decreasing temperatures. Following the analysis proposed in the Refs. [11, 68, 95, 185, 188–190], the broadened minimum can be identified as an energy scale $T^*_\rho(B)$ from the distinct minimum of the derivative $\mathrm{d}\rho/\mathrm{d}B$ (Fig. 5.19 (c)). Typically the minimum in $\rho(B)$ corresponds with the minimum of the entropy in magnetic systems. Due to applied magnetic fields the magnetic fluctuations are suppressed and a minimum in $\rho(B)$ can be obtained in a magnetic system.

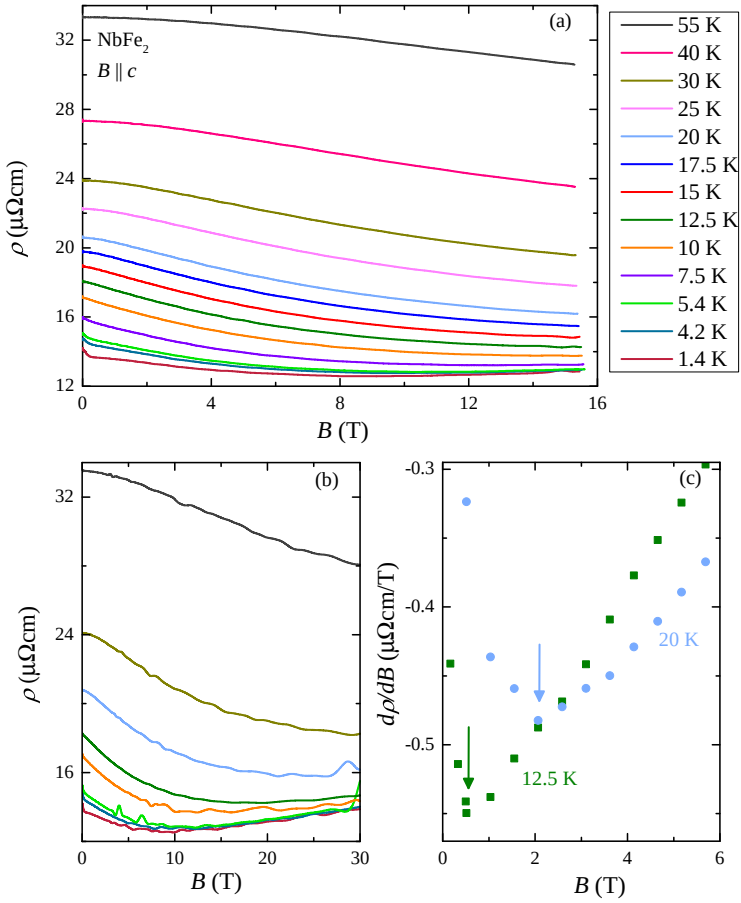

Fig. 5.19: Magnetic field dependence of the electrical resistivity for $NbFe_2$ for applied magnetic fields along the c-axis up to 16 T (a) and 30 T (b) at various temperatures. The derivatives $\mathrm{d}\rho/\mathrm{d}B$ versus B are displayed at $T = 12.5$ K and 20 K (c). The arrows mark the minima, corresponding to the energy scale $T^*_\rho(B)$; for details see text.

In the same line of thought, the dc-susceptibility $\chi = M/B$ as depicted in Figs. 5.17 (a) and 5.18 (a) allows to derive the energy scale $T^*(B)$ determined at the minimum of the derivation $\mathrm{d}\chi/\mathrm{d}T$ (Figs. 5.17 (c) and 5.18 (c)) for applied magnetic fields along the c- and a-axis. For low

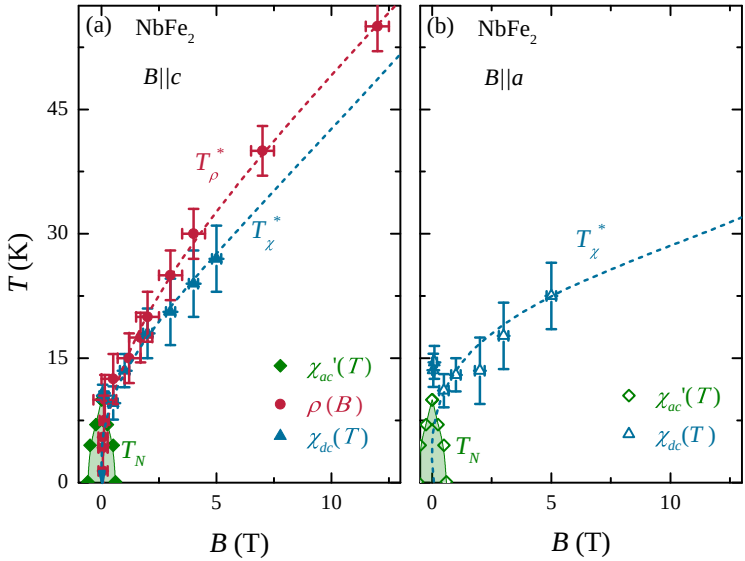

Fig. 5.20: Energy scale $T^*(B)$ for $NbFe_2$ derived from the dc-susceptibility $T^*_\chi(B)$ and resistivity $T^*_\rho(B)$ for $B||c$ (a) and $B||a$ (b). The green diamonds represents the SDW phase with the Néel temperature (T_N) according to the Refs. [17, 18].

magnetic fields ($B \leq 0.1$ T) the paramagnetic Curie-Weiss behavior undergoes into the SDW modulated state ($T_N = 12$ K) as indicated by a maximum, which moves with increasing B to decreasing temperatures.

Fig. 5.20 depicts both energy scales $T^*_\rho(B)$ and $T^*_\chi(B)$ of an applied magnetic field along the a- and c-axis, as determined from these procedures; $T^*_\rho(B)$ is only determined for $B||c$. According to the Refs. [185, 191], this energy scale represents the inflection point of the field derivative of the entropy $S(B)$, which could be obtained by $\Delta M/\Delta T \approx \mathrm{d}M/\mathrm{d}T = \mathrm{d}S/\mathrm{d}B$. Therefore, the scale $T^*(B)$ defines the lines of $\mathrm{d}^2S/\mathrm{d}B^2 = 0$, and the magnetic entropy decreases with increasing field. At the PM-to-SDW transition for $NbFe_2$, the field evolution of the energy scale $T^*(B)$ changes discontinuously up to a critical temperature, where $T^*(B)$ jumps suddenly to a zero temperature with a crossover field $B_0 = 0$ T.

A similar behavior of the temperature and field evolution of such an energy scale can be seen in the prototypical f-electron system $YbRh_2Si_2$ [11]. Here, the crossover line $T^*(B)$ describes the magnetic phase boundary $T_N(B)$ and the paramagnetic Landau-Fermi liquid phase $T_{LFL}(B)$ at $B = B_c$ in the zero-temperature limit and vanishes at the quantum critical point. For this material, quantum criticality is investigated extensively by thermodynamic and transport measurements [11, 68, 175, 185, 192]. The origin of the T^* line in $YbRh_2Si_2$ is an electronic deceleration of strong fluctuations caused by f-electrons, which separates a large Fermi surface (delocalized f-electrons) and a small Fermi surface with localized f-electrons. This energy scale vanishes at the QCP and is accompanied by a destruction of the Kondo effect.

In contrast, in the d-electron system $NbFe_2$ and also in several f-systems, e.g. $Yb(Rh_{1-x}Co_x)_2Si_2$, $x \geq 0.03$ [185, 193], the $T^*(B)$ scale clearly reaches into the magnetically ordered phase instead of being associated to quantum criticality. As well, a destruction of the Kondo effect appears not to be a proper scenario to account for this behavior. Thus, it is an example for an alternative scenario for this crossover behavior in such d-metal systems.

5.5 Discussion and Summary

Concluding this chapter, itinerant intermetallic $Nb_{1-y}Fe_{2+y}$, $-0.04 \leq y \leq 0.04$, exhibits a complex magnetic phase diagram including ferromagnetic ordering and a SDW modulated state. Slight changes in stoichiometry separate the phase diagram into regions with different magnetic properties, that is an Fe-rich region, close to stoichiometric $NbFe_2$ and a Nb-rich region. These three regions of the magnetic phase diagram have been confirmed to exist as bulk phases. This was realized by utilization of the microscopic techniques muon spin relaxation and Mössbauer spectroscopy for the first time.

Bulk measurements of previous studies presumed a SDW phase being sur-

rounded by different ferro- or ferrimagnetic phases in Nb- and Fe-rich regions [17–19, 21, 180, 181]. Spin-glass behavior, superparamagnetism and domain effects have been excluded for the SDW state [17, 18]. Weak transverse field μSR experiments observe a complete loss in the temperature dependent asymmetry parameter, and represent a measure for the volume fraction of the paramagnetic state. Hence, the asymmetry parameter proves the bulk nature of the magnetically ordered states. The internal magnetic field of the SDW phase is parametrized in ZF μSR by the fit best suited to describe the data: a Bessel function for the internal field distribution from a SDW state [131, 132]. Here, the conceptional problem is caused by the very small magnetic moments resulting in a damped asymmetry spectrum, leaving a wide margin for fit approaches to be used. In accordance with the bulk properties a fit of the Bessel function provides the best description of the local field distribution in the spin modulated phase.

Comparing ZF μSR asymmetry spectra for all investigated $Nb_{1-y}Fe_{2+y}$ samples, we detect a different nature of the magnetically ordered ground state for Fe-rich $Nb_{0.982}Fe_{2.018}$. In contrast to a strongly damped signal as for the SDW ordering, a spontaneous muon rotation signal occurs – indicating ferro- or ferrimagnetic order which gives rise to distinct local internal fields at the muon stopping sites. Mössbauer spectroscopy (for $Nb_{0.984}Fe_{2.016}$) proves the existence of a weakly ferromagnetic ordered state. From the line broadening a local magnetic hyperfine field of less than 2 T is estimated, which corresponds to an upper limit of the ordered magnetic moment of about $0.15\,\mu_B/$ Fe atom from scaling to metallic Fe. This is consistent with the net magnetic moment of $0.06\,\mu_B/$ Fe atom, as determined from magnetization measurements [180]. Previous Compton scattering studies have been used as an argument to propose ferrimagnetic order with magnetic moments of $0.4\,\mu_B(-0.6\,\mu_B/$ Fe atom) for the Fe ($6h$) (Fe ($2a$)) site [181]. These moments on the Fe atoms would imply transferred hyperfine magnetic fields of greater or equal to 6 T, which is disproven by the Mössbauer data.

The characteristic frequency of the internal field in the ferromagnetic state and the Bessel function for the internal field distribution in the SDW modulated states, which defines the order parameter, allow an estimation of the size of the magnetic moment. Assuming that the SDW amplitude scales in the same way as the ferromagnetic moments, a low temperature magnetic moment size range from about $0.06\,\mu_B$/Fe atom in $Nb_{0.984}Fe_{2.016}$ to only about $5 \cdot 10^{-4}\,\mu_B$/Fe atom in $Nb_{1.0055}Fe_{1.9945}$ is obtained.

The temperature evolution of the order parameter for $Nb_{1-y}Fe_{2+y}$, $-0.019 \leq y \leq -0.004$, appears to develop in a highly unusual way (Fig. 5.8). Close inspection of the data (e.g. in $Nb_{1.004}Fe_{1.996}$) indicates a wide temperature range for the phase transitions, with parts of PM and SDW states coexisting in this temperature window. Fits of the data at lowest temperatures with a strongly damped asymmetry spectrum yields $0 - 1$ MHz as the characteristic frequency of the μSR spectrum, which leads to an extremely small low temperature magnetic moment of a few $1/1000$st of $\mu_B/$ Fe atom.

All in all, the evolution of the temperature dependence of the order parameter is not a smooth function in the way expected for a second order phase transition parameter. Instead, magnetic order sets in at the transition temperature, but with an apparently very small characteristic frequency, which rises at a rather slow rate. A similar anomalous moment evolution was measured for instance for URu_2Si_2 [194]. Here, it has been demonstrated that such a behavior reflects a magnetically inhomogeneous sample [195]. In fact, wTF μSR measurements reveal that for $Nb_{1-y}Fe_{2+y}$, $-0.019 \leq y \leq -0.004$, the magnetic transitions are significantly broadened. In consequence, the determination of the characteristic frequency just below T_N is affected by the volume amount of magnetically ordered phase, causing a rather large experimental uncertainty. At lowest temperatures, with the complete loss of asymmetry in the wTF μSR, $Nb_{1-y}Fe_{2+y}$, $-0.0055 \leq y \leq 0.0$, has undergone the transition into the SDW state with a relaxation appropriately described by the Bessel function for the internal field distribution in the SDW modu-

lated state. In contrast, the relaxation for $Nb_{1.019}Fe_{1.981}$ is studied with an internal field distribution function for an assumed ferromagnetic state of bulk measurements. The strongly damped asymmetry spectrum indicates another kind of (ferro-)magnetic order. It is not clear if this is due to the very small magnetic moment of a few $1/1000$th of a $\mu_B/$ Fe atom, or if in fact the symmetry of the ordered magnetic state is not a ferromagnetic one. This observation, in turn, implies that for $Nb_{1-y}Fe_{2+y}$, $-0.019 \leq y \leq -0.004$ and $y \neq -0.0117$, phase separation into a magnetically ordered and a paramagnetic phase appears to occur over a wide temperature range. Altogether, our findings on the magnetic ground state of the series $Nb_{1-y}Fe_{2+y}$, $-0.019 \leq y \leq 0.016$, definitely proves that ferromagnetism is replaced by a bulk SDW phase upon approaching the quantum critical point (QCP).

Next, the evolution of the Fe ordered magnetic moments as function of the composition implies a completely suppressed magnetic moment at a critical composition $y_c \sim -0.006 \pm 0.001$, using an extrapolation of μ_{ord} as linear as possible. In contrast, bulk studies point to a distinctly different quantum critical point with a value $y_c = -0.015$ – suggesting either an unusual scaling of the magnetic moment with composition, such as $\mu_{ord} \propto (y-y_c)^k$ with $k \simeq 2 \pm 1$, or implying spontaneous phase segregation again. Fig. 5.10 indicates already a non-linear and non-consistent behavior for $\mu_{ord}(y)$ and $T_N(y)$. These findings raise the question about the nature of the magnetically ordered phase in the quantum critical range $-0.006 \leq y \leq y_c$.

Furthermore, μSR studies at a quantum critical point are performed for $Nb_{1.0117}Fe_{1.9883}$. For this sample, it has been established that down to lowest temperatures there is no magnetic order. Most notably, at lowest temperatures spin fluctuations occur on different time scales – a weakly damped signal ($t \leq 8\mu$s) with a strong drop at short times ($t \leq 0.4\mu$s). Up to now, there is no existing scenario that accounts for such behavior. Qualitatively, one might argue that different time scales correspond with different types of magnetic ordering, and that the suppression of magnetic

order at the QCP is thus the result of competition, to a degree reflecting the models at the basis of for instance the Doniach phase diagram. An experimental proof, or just an indication for this hypothesis does not exist at present. Usually, the experimental tool to further study this point would be inelastic neutron scattering. For $NbFe_2$, however, so far this approach has not resolved the issue, although various attempts have been carried out.

Alternatively, one might use further μSR studies to gain deeper insight into the physics of $NbFe_2$. Here, what would be required is a.) a determination of the muon stopping site, which would allow more accurate fits to describe the experimental data, and b.) a detailed study of the field and temperature dependence of the different relaxation times. Given the nature of μSR studies to be carried out at large scale facilities with only limited measurement time, following this concept was not possible in the present work.

Concluding, this microscopic study of the series $Nb_{1-y}Fe_{2+y}$ has established the intrinsic nature of the quantum critical point in the compositional phase diagram. Thus, the series does represent a prime example of a system to be discussed in the context of ferromagnetic quantum criticality.

6 Ferromagnetic fluctuations in $Ta(Fe_{1-x}V_x)_2$

The iron containing Laves phase compounds TFe_2 (T: transition metal) constitute one of the most important groups of intermetallic systems (cf. section 2.3), showing a multitude of different magnetic properties and ground states as function of the species T. For instance, some of these compounds display ferro- or antiferromagnetism, as for example $ZrFe_2$ [13, 196] and $TiFe_2$ [70]. In contrast, many of the hexagonal C14 Laves phase compounds, such as $NbFe_2$ and $TaFe_2$, are weakly to non-magnetic. Both materials exhibit a quite anomalous magnetic behavior with pronounced ferromagnetic/antiferromagnetic fluctuations (see for instance the preceding chapter 5 on $NbFe_2$). Moreover, concentration variations around the stoichiometric composition lead to various forms of ferro- and/or antiferromagnetism. Measurements of susceptibility and specific heat reveal the onset of very weak ferro- or antiferromagnetism, respectively, in the two systems [17, 18, 179, 197, 198]. These types of magnetically ordered states are generated for approximately the same number of d-electrons contributing to the conduction band, and for rather similar lattice constants. $TaFe_2$ has a slightly smaller mean atomic volume (~ 13.25 Å^3) than $NbFe_2$ (~ 13.35 Å^3) [197]. Hence, $TaFe_2$ could be expected to be closer to a quantum critical point than $NbFe_2$, due to the fact that magnetic properties in $NbFe_2$ can be tuned from a ferromagnetic via a spin density wave modulated state to a QCP by changing the composition within a narrow homogeneity range or by applying hydrostatic pressure [17, 19–21].

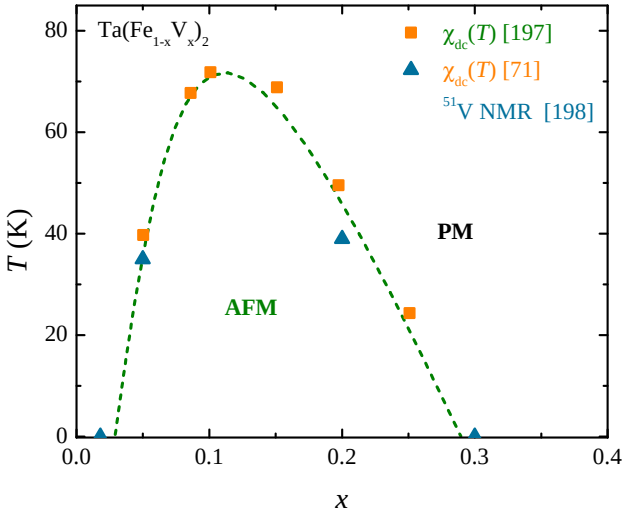

Fig. 6.1: Proposed magnetic phase diagram for Ta(Fe$_{1-x}$V$_x$)$_2$, $0.0 \leq x \leq 0.4$. The green and orange points have been obtained from dc-susceptibility measurements in a magnetic field of $B = 0.1$ T taken from Refs. [71, 197], and the blue data is a result of ^{51}V NMR experiments from Ref. [198].

Recent investigations of bulk experiments and ^{51}V NMR present present a paramagnetic ground state for stoichiometric TaFe$_2$, while substitution of vanadium for iron induces the formation of an itinerant antiferromagnetic state in the range of $0.05 \leq x \leq 0.25$ [71, 197–199]. At low temperatures the magnetic susceptibility of TaFe$_2$ increases to very high values (at magnetic fields of $B = 0.1$ T) without any phase transition. For Ta(Fe$_{0.98}$V$_{0.02}$)$_2$ this unusual behavior is most pronounced with the largest value of the magnetic susceptibility, while for $x \geq 0.025$ the values decrease already. Also, ^{51}V NMR studies observe a signature of critical fluctuations for $x = 0.025$ with a $T^{-0.86}$ dependence of $1/T_1T$ for small fields. This reveals Ta(Fe$_{0.98}$V$_{0.02}$)$_2$ as a system with a nearly ferromagnetic state. Accordingly, the magnetic phase diagram of Ta(Fe$_{1-x}$V$_x$)$_2$ as determined from bulk experiments and ^{51}V NMR is divided into three regimes, see Fig. 6.1. For very small concentrations of V up to $x = 0.025$

the system is paramagnetic with enhanced magnetization at low temperatures [71, 197]. Ta($Fe_{0.98}V_{0.02}$)$_2$ is a sample close to a ferromagnetic instability. Upon further doping for $0.05 \leq x \leq 0.25$, the data shows the appearance of weak antiferromagnetic (AFM) features with a dome-like shape of $T_N(x)$. For $x \geq 0.25$ the system shows paramagnetic behavior again. The effect of vanadium substitution has been taken as an argument to classify Ta($Fe_{1-x}V_x$)$_2$ as an itinerant weak AFM in the framework of Moriya's self-consistent renormalization theory [96]. To complement the studies carried out so far, and in particular to provide additional insight into the magnetic properties on a microscopic level, Mössbauer spectroscopy experiments have been performed on Ta($Fe_{1-x}V_x$)$_2$ and will be presented in this chapter.

For this study several polycrystalline samples of Ta($Fe_{1-x}V_x$)$_2$, $0.00 \leq x \leq 0.35$, have been prepared by A. Kerkau and G. Kreiner at the Max Planck Institute for Chemical Physics of Solids, Dresden. These have been produced by arc melting from high purity elements as starting materials (99.95% Ta, 99.995% Fe and 99.98% V) on the water-cooled copper hearth of an electric arc furnace and subsequent a heat treatment at 1150 °C. After annealing for 30 days the samples were quenched in water. The actual composition of the samples was determined by inductively coupled plasma optical emission spectrometry (ICP-OES). Also, X-ray powder diffraction, metallographic examinations and quantitative chemical analysis were carried out to check the phase quality, details are given in Ref. [197]. $TaFe_2$ crystallizes in the hexagonal C14 structure type (lattice parameter $a = 4.8821$ Å and $c = 7.8963$ Å [200]), while TaV_2 crystallizes in the cubic C15 structure type ($a = 7.160$ Å [201]). The lattice constants a and c increase almost linearly with the substitution of V for Ta($Fe_{1-x}V_x$). The homogeneity ranges of the C15 and C14 Laves phases are investigated in detail in Ref. [197], with a homogeneity range of the C14 phase of $0.0 \leq x \leq 0.35$.

Altogether, for the Mössbauer study six samples have been prepared, three of them being nominally stoichiometric $TaFe_2$ (samples labeled AK170,

AK136 and AK139), and another three with varying levels of vanadium alloying according to Ta(Fe$_{1-x}$V$_x$)$_2$, $x = 0.05$ (AK172), $x = 0.087$ (AK168)[1] and $x = 0.2$ (AK126). The three stoichiometric samples were produced to separate intrinsic from extrinsic magnetic properties. They show uniform versus non-uniform magnetic behavior. Further, the three alloyed samples have been chosen to cover the dome of the antiferromagnetic phase for the alloying phase diagram $T_N(x)$.

6.1 Magnetic behavior of Ta(Fe$_{1-x}$V$_x$)$_2$

For an essential characterization of the samples studied here, magnetization experiments were carried out in a vibrating sample magnetometer in the temperature range of $1.8 - 300$ K by M. Brando at the Max Planck Institute for Chemical Physics of Solids, Dresden. Parts of the results are already published in Ref. [197]. All in all, depending on the vanadium concentration in Ta(Fe$_{1-x}$V$_x$)$_2$ many interesting magnetic properties appear, which will be summarized below. In recent years several magnetic studies of the alloy Ta(Fe$_{1-x}$V$_x$)$_2$ systems have been carried out [71, 196, 197, 199, 200], resulting in the magnetic phase diagram in Fig. 6.1. The stoichiometric TaFe$_2$ and Ta(Fe$_{1-x}$V$_x$)$_2$ with a low vanadium concentration $x \leq 0.02$ are proposed to be paramagnetic, while Ta(Fe$_{1-x}$V$_x$)$_2$ with $0.05 \leq x \leq 0.25$ are reported to be itinerant antiferromagnets. Therefore, we studied the temperature dependence of magnetic dc-susceptibility $\chi(T)$ and inverse dc-susceptibility $\chi^{-1}(T)$ for all samples used in the following Mössbauer spectroscopy experiments (cf. Fig. 6.2). Starting from high temperatures in the paramagnetic (PM) phase, decreasing the temperature leads to two magnetic phase transitions: a first one around 90 K, and a second less sharp one at $T \leq 70$ K.

For a tighter definition of these transitions, ac-susceptibility experiments have been carried out under a weak alternating ac-field (with a frequency of 113 Hz) as function of the external magnetic field up to $B = 2.5$ T.

[1] The sample AK168 was prepared by Y. Yamada *et al.* [71].

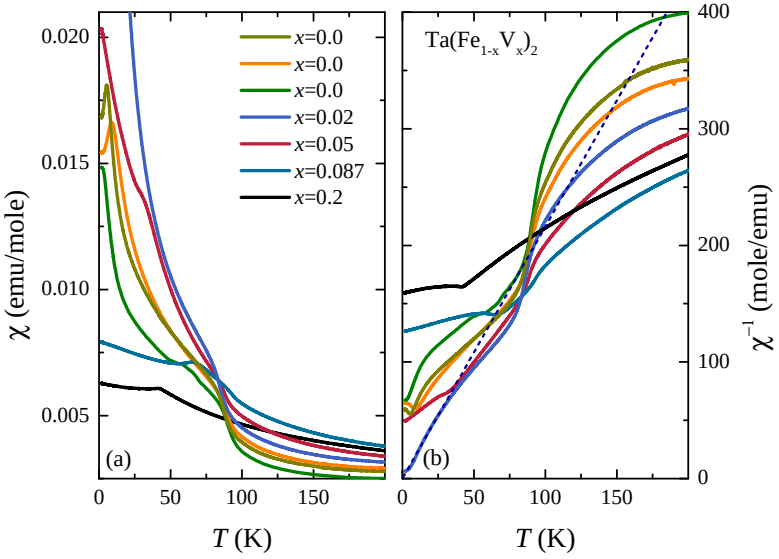

Fig. 6.2: Temperature dependence of the (a) dc-susceptibility $\chi(T)$ at $B = 0.1$ T and (b) and inverse dc-susceptibility $\chi^{-1}(T)$ for Ta($Fe_{1-x}V_x$)$_2$, $0.0 \leq x \leq 0.2$. Data is provided by M. Brando, Max Planck Institute for Chemical Physics of Solids, Dresden.

As a representative set of data the real component of the ac-susceptibility signal, $\chi'(T)$, of $TaFe_2$ (AK170) is shown in Fig. 6.3. Again, in this data, both phase transitions appear, but the first one (around 90 K) is almost completely suppressed for magnetic fields $B \geq 1$ T. Magnetization measurements indicate that this feature in the dc- and ac-susceptibility arises from a negligible amount of clustered ferromagnetic impurities. In other words, the transition at 90 K is a spurious artifact stemming from sample impurities and therefore we will not be considered for further experiments. Conversely, regarding the magnetic properties of Ta($Fe_{1-x}V_x$)$_2$, only the low temperature phase transition should be of relevance.

According to the dc-susceptibility data, at low temperatures stoichiometric $TaFe_2$ undergoes a transition at temperatures of $T_C = 2$ K (AK136), 5 K (AK170) and 9 K (AK139), respectively in contrast to Refs. [71, 196,

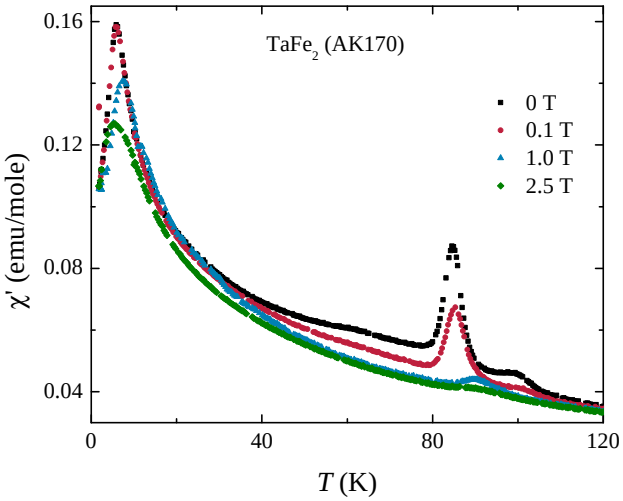

Fig. 6.3: Temperature dependence of the real component of the ac-susceptibility $\chi'(T)$ of $TaFe_2$ in external fields up to 2.5 T. Data is provided by M. Brando, Max Planck Institute for Chemical Physics of Solids, Dresden.

199, 200]. For $T < T_N$ the changing slopes in the Arrott plot (M^2 versus B/M) suggests a transition into a antiferromagnetic state [18], which is exemplary shown for AK139 and AK170 in Fig. 6.4. In contrast the Arrott plot for $Ta(Fe_{0.98}V_{0.02})_2$ show only a positive slope in the complete temperature range, this indicates no existence of spontaneous magnetization down to $T = 2$ K (see Fig. 6.5). For $T = 2$ K the extrapolation of the curve yields an intercept M^2, which goes almost to zero. A finite M^2 intercept at $B/M = 0$ would be a clear indication of ferromagnetism. Therefore, $Ta(Fe_{0.98}V_{0.02})_2$ is close to a ferromagnetic quantum critical point. For vanadium substitution of iron in $Ta(Fe_{1-x}V_x)_2$ the susceptibility $\chi(T)$ increases weakly with a shoulder at low temperatures and also show a shoulder of AFM ordering at the transition temperatures $T_N = 31$ K ($x = 0.05$, AK172), 66 K ($x = 0.087$, AK168) and 42 K ($x = 0.2$, AK126) in agreement to Y. Horie *et al.* [71].

These results are as well confirmed by ^{51}V NMR experiments of the

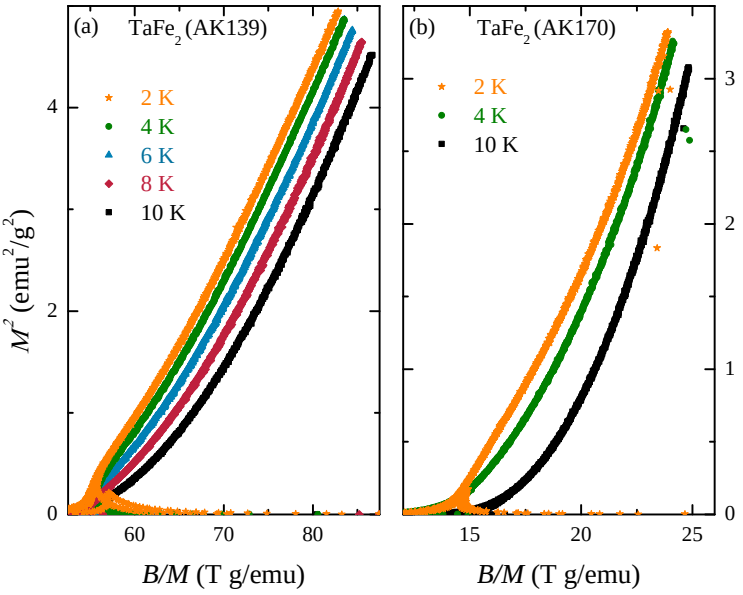

Fig. 6.4: Temperature dependence of the Arrott plot (M^2 versus B/M) of $TaFe_2$ for AK139 and AK170. Data is provided by M. Brando, Max Planck Institute for Chemical Physics of Solids, Dresden.

Refs. [71, 185], whereas for very small concentrations of V up to $x = 0.05$ the system is close to a FM instability. ^{51}V NMR experiments detect a small negative shift of the peak function and for small fields the ^{51}V $(1/T_1T)$ line indicates a $T^{-0.8}$ dependence of spin lattice relaxation rate, which is a signature of ferromagnetic spin fluctuations [71, 198].

However, for both samples of $x = 0.02$ (FM QCP) and $x = 0.2$ (AFM) a great difference in the dc-susceptibility at 2 K (Fig. 6.2) can be observed. The susceptibility of Ta($Fe_{0.98}V_x$)$_{0.02}$ is enhanced by spin fluctuations related to a Stoner factor of about 240 [197], which is estimated by comparing the experimental value of the susceptibility at $T = 2$ K with the expected value from the band structure calculations. In comparison, $NbFe_2$ exhibits a smaller Stoner factor of ~ 180 [17]. Furthermore, the fluctuating moment in this sample is analyzed with a linear fit to the Curie Weiss

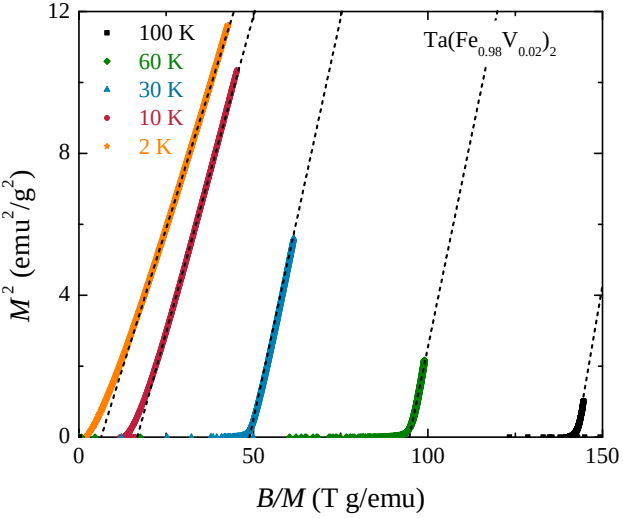

Fig. 6.5: Temperature dependence of the Arrott plot (M^2 versus B/M) for Ta(Fe$_{0.98}$V$_x$)$_{0.02}$ did not show any spontaneous magnetization. Data is provided by M. Brando, Max Planck Institute for Chemical Physics of Solids, Dresden.

law in $\chi^{-1}(T)$ below temperatures of 50 K [197], which is illustrated by a dashed line in Fig. 6.2 (b). In the special case of Ta(Fe$_{0.98}$V$_{0.02}$)$_2$ various magnetic studies point to a FM instability with an effective magnetic moment of $\mu_{eff} = 1.04\mu_B$ per Fe atom, which is much larger than the induced magnetic moment measured of $\sim 0.055\mu_B$/ Fe atom at 7 T (extrapolation of $M(B)$, see Ref. [197]). This leads to a characteristic feature of a weak itinerant ferromagnet. Thus, the strength of FM fluctuations decreases with increasing vanadium substitution. Therefore, itinerant antiferromagnetism develops in a range of $0.05 \leq x \leq 0.25$ at low temperatures ($T_N \leq 70$ K).

TaFe$_2$ and NbFe$_2$ show similar magnetic properties in the existence of strong antiferromagnetic or SDW order, which may suppress the appearance of ferromagnetism. Therefore, Ta(Fe$_{1-x}$V$_x$)$_2$ may exhibit a ferromagnetic QCP as well as Nb$_{1-y}$Fe$_{2+y}$.

6.2 Mössbauer measurements

The presence and extent of ferro- and antiferromagnetic correlations in $Ta(Fe_{1-x}V_x)_2$ are investigated on the powdered samples introduced above (section 6.1) by means of ^{57}Fe Mössbauer spectroscopy. The experiments were performed in a continuous-flow cryostat in the temperature range of $4 - 300$ K without externally applied magnetic fields. The main focus of this study is to locally investigate the development of magnetic order and the related magnetic hyperfine fields B_{hf} at the Fe sites. As starting point of the data analysis, we present representative spectra for all samples in absolute free magnetic states at a temperature around 100 K in Fig. 6.7 and Fig. 6.8. The absorption spectra show a doublet structure, which is typical for nuclear electric quadrupole interaction for the $I = 3/2 \rightarrow I = 1/2$ nuclear transition of ^{57}Fe. Closer inspection reveals that we have to take two pairs of quadrupole doublets into account, that have their origins of different electronic surroundings of Fe occupying Fe($6h$) and Fe($2a$) sites in the C14 Laves phases (cf. section 2.3). The two kinds of Fe sites have a relative occupancy ratio of $3 : 1$. This ratio can also be reproduced by the relative spectra areas of the two doublet pairs used in fitting.

At low temperatures (as we will see below), in the magnetically ordered states of $TaFe_2$ substituted with $5 - 20\%$ vanadium we also find a doublet structure with a significant line broadening. Notably the spectra structure now reveals asymmetry. This is caused by small magnetic hyperfine fields at the Fe atoms. Furthermore, it will turn out that B_{hf} has no distinct value, but rather shows a distribution.

All absorption spectra are analyzed using a full Hamiltonian comprising magnetic and electric quadrupole hyperfine interaction (MossWinn, model of W. Kündig [202]). This is necessary since both (quadrupole and magnetic) hyperfine interactions are of comparable strength and need to be diagonalized simultaneously for yielding eigenvalues (given relative position of resonance lines) and eigenvectors (for determining line intensities) for the nuclear levels. The nuclear static Hamiltonian is expressed in the coordinate eigensystem ($\boldsymbol{e_x}, \boldsymbol{e_y}, \boldsymbol{e_z}$) of the electrical field gradient (EFG)

and is solved by a diagonalization. For the case of ^{57}Fe the Hamiltonian matrix $\boldsymbol{H(I)}$ of the excited $I = 3/2$ level is a 4×4 Hermitian matrix. The elements are expressed by:

$$\begin{aligned} H(I)_{m_I,m_I} &= \omega_Q \hbar \left[3m_I^2 - I(I+1) - \omega_H \hbar m_I \cos(\beta)\right] \\ H(I)_{m_I,m_I+1} &= \frac{-\omega_H \hbar \sin(\beta)}{2} \sqrt{I(I+1) - m_I(m_I+1)}\, e^{i\alpha} \\ H(I)_{m_I,m_I+2} &= \frac{\omega_Q \hbar}{2} \eta \sqrt{[I(I+1) - (m_I+2)(m_I+1)]} \\ &\quad \cdot \sqrt{[I(I+1) - m_I(m_I+1)]} \end{aligned} \tag{6.1}$$

with

$$\omega_Q = \frac{1}{\hbar} \frac{eV_{zz}Q}{4I(2I-1)} \qquad \text{and} \qquad \omega_H = \frac{g_N(I)\boldsymbol{B_{hf}}\mu_N}{\hbar}, \tag{6.2}$$

where $\boldsymbol{B_{hf}}$ denotes the magnetic hyperfine field, β the polar angle and α the azimuthal angle of $\boldsymbol{B_{hf}}$ relative to the unit vector $\boldsymbol{e_z}$. V_{zz} is the electric field gradient main component (along $\boldsymbol{e_z}$), η the asymmetry parameter and Q the nuclear quadrupole moment of ^{57}Fe ($I = 3/2$). Additional, I marks the angular momentum quantum number of the excited or ground state of ^{57}Fe nucleus, while the magnetic spin quantum number m_I goes through the values of $-I, -I+1 ... I-1, I$. Further parameters are the gyromagnetic factor g_N and the nuclear magnetic moment μ_N of ground state of ^{57}Fe.

For proportional spectral areas the corresponding eigenvectors of the excited and ground state levels taking into account the appropriate angular momentum selection rules for the magnetic γ-transition between $I = 3/2$ and $I = 1/2$. The calculation of the Hamiltonian matrix of the ^{57}Fe ground state ($I = 1/2$) is done analogously to the calculation of the excited level (Eq. (6.1)), whereas $\boldsymbol{H(I)}$ is independent of Q. We furthermore have assumed that our samples are powders with random orientations of the electric field gradient versus the direction of γ-ray. Isomer shift IS (center of gravity of spectrum) and experimental line width LW are addi-

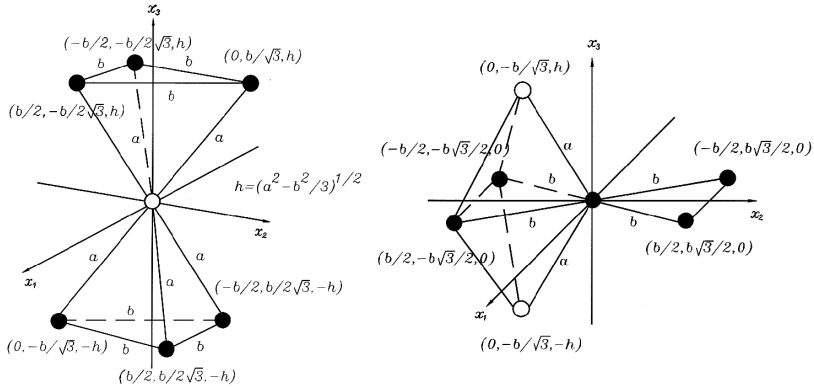

Fig. 6.6: Nearest-neighbor atomic environment of the C14 Laves ($2a$) site (a) and ($6h$) site (b) in an Cartesian coordinate system for principal axes of the EFG tensor, taken from Ref. [203].

tional fitting parameters.

On consideration of the multitude of possible fitting parameters (e.g. η), we introduce some simplification. η of the EFG is determined with a nearest-neighbor point-charge model according to a Mössbauer spectroscopic study of $Zr(Fe_xCr_{1-x})_2$ by J. A. H. Coaquira *et al.* [203]. Assuming that all nearest-neighbor sites are either Fe($2a$) or ($6h$) atoms or substituted by vanadium, this model takes into account the nearest-neighbor atomic environment of both Fe sites (Fig. 6.6), resulting in the diagonalized components of the EFG tensor (Eq. (3.37)). After all, for the Fe($2a$) sites it results in

$$V_{xx} = \frac{3d_b^2 - 6d_a^2}{d_a^5} = -0.214 \tag{6.3}$$

$$V_{yy} = \frac{3d_b^2 - 6d_a^2}{d_a^5} = -0.214 \tag{6.4}$$

$$V_{zz} = 6\left(\frac{3}{d_a^3} - \frac{d_b^2}{d_a^5} - 1\right) = -5.142 \tag{6.5}$$

$$\eta = 0.0 \tag{6.6}$$

and for the Fe($6h$) sites in

$$V_{xx} = \frac{-2}{d_a^3} - \frac{1}{d_b^3} = -0.214 \tag{6.7}$$

$$V_{yy} = \frac{2d_b^2}{d_a^5} - \frac{2}{d_a^3} + \frac{5}{d_b^3} = 0.357 \tag{6.8}$$

$$V_{zz} = \frac{4}{d_a^3} - \frac{2d_b^2}{d_a^5} - \frac{4}{d_b^3} = -0.142 \tag{6.9}$$

$$\eta \cong 0.2 \tag{6.10}$$

with the interatomic bond distance of $d_a = Fe(2a) - Fe(6h) = 2.412$ Å and $d_b = Fe(6h) - Fe(6h) = 2.410$ Å calculated for $TaFe_2$ by

$$d_a^2 = 3(1 - \frac{5}{6})^2 a^2 + \frac{1}{16}c^2 \tag{6.11}$$

$$d_b^2 = 9(1 - \frac{5}{6})^2 a^2 \tag{6.12}$$

for C14 Laves phases taking into account the lattice parameters a and c [204]. For the condition $|V_{xx}| < |V_{yy}| < |V_{zz}|$ and Eq. (3.34) the equations mentioned above lead to $\eta_{2a} = 0.0$ and $\eta_{6h} \cong 0.2$. Thus for both Fe($2a/6h$) sites the electric field exhibits an almost cubic symmetry at the position of the Fe nucleus in Ta(Fe$_{1-x}$V$_x$)$_2$. In this situation of a very small asymmetry parameter, the azimuthal angle α has negligible effect on the fitting. Therefore, we keep it fixed to zero.

6.2.1 Mössbauer studies on stoichiometric $TaFe_2$

As set out above, stoichiometric $TaFe_2$ seems to be paramagnetic with antiferromagnetic (AFM) fluctuations for $B = 0.1$ T as seen in susceptibility measurements (cf. section 6.1). We have studied the absorption spectra of stoichiometric $TaFe_2$ (AK170, AK136 and AK139), shown in Fig. 6.7 for the temperatures 4 K and 100 K respectively. For all samples the typical paramagnetic patterns of sharp doublet structures from nuclear quadrupole interactions are observed. Even at lowest temperatures the absorption spectra provide no evidence (line broadening, asymmetry, etc.)

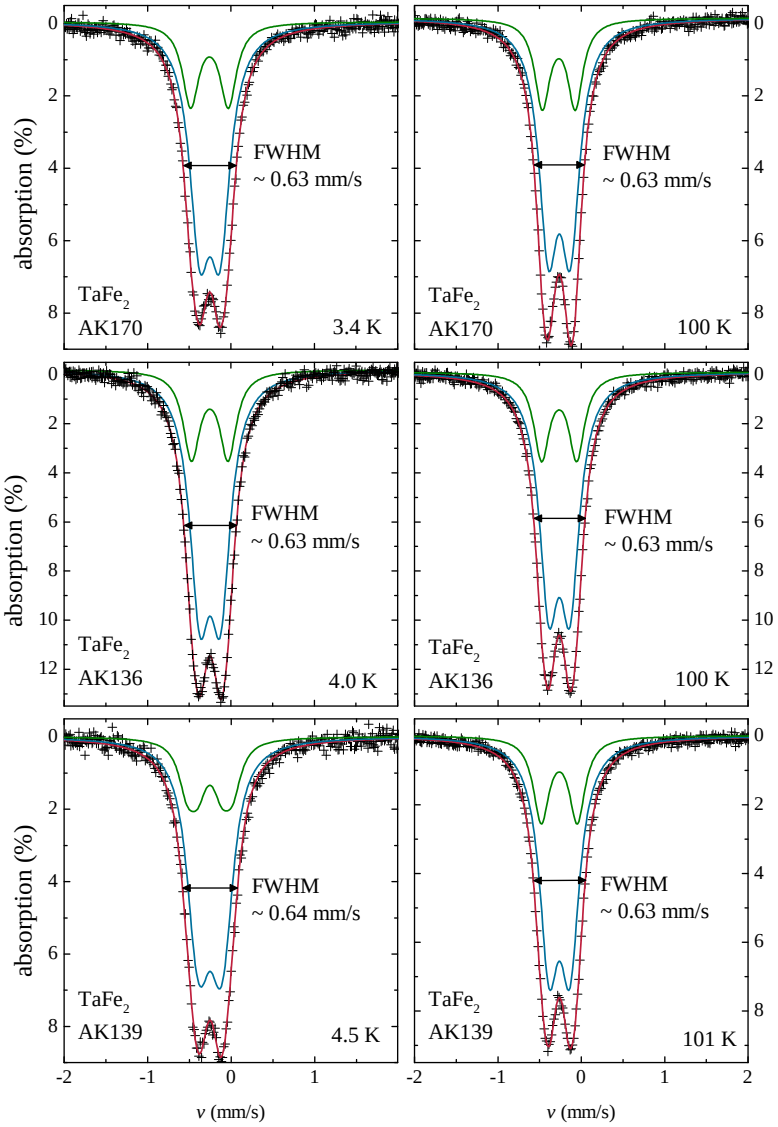

Fig. 6.7: Mössbauer absorption spectra of stoichiometric $TaFe_2$ analyzed using two subspectra for the Fe($2a$) (green) and Fe($6h$) sites (blue) at $\sim$ 4 K (left) and $\sim$ 100 K (right).

x	T (K)	IS (mm/s)	ΔE_Q (mm/s)	LW (mm/s)	IS (mm/s)	ΔE_Q (mm/s)	LW (mm/s)
		Fe ($2a$) site $A75\%$, $\eta = 0$			Fe ($6h$) site $A = 25\%$, $\eta = 0.2$		
AK170	250	-0.344	0.39	0.221	-0.339	0.25	0.274
	200	-0.317	0.39	0.221	-0.310	0.26	0.273
	100	-0.270	0.39	0.220	-0.263	0.26	0.274
	20	-0.252	0.44	0.227	-0.250	0.24	0.296
	8	-0.262	0.38	0.227	-0.252	0.27	0.277
	4	-0.257	0.24	0.238	-0.253	0.24	0.295
AK136	300	-0.371	0.38	0.242	-0.366	0.26	0.276
	250	-0.340	0.39	0.240	-0.336	0.26	0.282
	200	-0.291	0.39	0.206	-0.288	0.24	0.254
	100	-0.265	0.42	0.227	-0.262	0.25	0.276
	20	-0.256	0.40	0.224	-0.250	0.26	0.273
	8	-0.256	0.44	0.274	-0.252	0.25	0.309
	4	-0.253	0.44	0.240	-0.250	0.25	0.292
AK139	175	-0.277	0.44	0.214	-0.276	0.21	0.290
	150	-0.278	0.43	0.231	-0.274	0.24	0.281
	100	-0.264	0.43	0.228	-0.262	0.25	0.278
	40	-0.257	0.41	0.215	-0.252	0.26	0.271
	20	-0.257	0.41	0.232	-0.253	0.26	0.279
	8	-0.257	0.43	0.239	-0.253	0.26	0.282
	4	-0.253	0.48	0.242	-0.251	0.25	0.290

Tab. 6.1: Fitted parameters of the Mössbauer absorption spectra of stoichiometric $TaFe_2$ used for the fits two sites for Fe ($2a$) and Fe ($6h$) in a ratio of $1:3$, $B_{hf} = 0$, $\beta = 0$ and $\alpha = 0$.

of a phase transition down to 4 K. Thus, in contrast to the susceptibility measurements by means of Mössbauer spectroscopy no magnetic ordering behavior in stoichiometric $TaFe_2$ is detected. Therefore, the magnetic properties observed in the bulk measurements could be ascribed to inhomogeneous samples (and thus magnetic order form a minority phase).
As described above the absorption spectra analyzed by means of the model in section 6.2 with a fixed area fraction for iron ions occupying $(2a)$ and $(6h)$ sites in a ratio of $1:3$. The results of the fits are shown in Fig. 6.7 and summarized in Tab. 6.1. The temperature dependence of the isomer shifts IS and the full line width LW are identical for both Fe sites. The IS decreases with lowered temperatures as result of the temperature dependent second order Doppler shift (see chapter 3.2.2). Both Fe sites exhibit almost equal IS values, which indicates the same valence in both Fe sites. Besides, the electric quadrupole splitting ($\Delta E_Q = 1/2eQV_{zz}\sqrt{1+\eta^2/3}$) for the Fe($2a$) sites with $\Delta E_Q = 0.44$ mm/s is about two times larger than for the Fe($6h$) sites $\Delta E_Q = 0.26$ mm/s. This great deviation to the calculated values of V_{zz} and η (in section 6.2) is surprising. However, this reveals that the absolute values do not correspond to the nearest-neighbor point-charge model.

6.2.2 Mössbauer studies on $Ta(Fe_{1-x}V_x)_2$

The alloyed samples $Ta(Fe_{1-x}V_x)_2$ in the range of $0.04 \leq x \leq 0.27$ and at temperatures of $T \leq 70$ K undergo transitions into itinerant antiferromagnetic states. In order to analyze this type of magnetic order on a microscopic scale, Mössbauer spectroscopy experiments were performed for the distinct vanadium concentrations $x = 0.05, 0.087$ and 0.2 (sample numbers: AK172, AK168, AK126). Fig. 6.8 depicts the absorption spectra in the magnetically ordered state at a temperature of 5 K and in the paramagnetic phase at ~ 80 K.
Again, as in stoichiometric $TaFe_2$, in the paramagnetic phase a doublet structure is observed for all samples, which is fitted accordingly (see Tab. 6.2 and solid lines in Fig. 6.8). For low temperatures the doublets

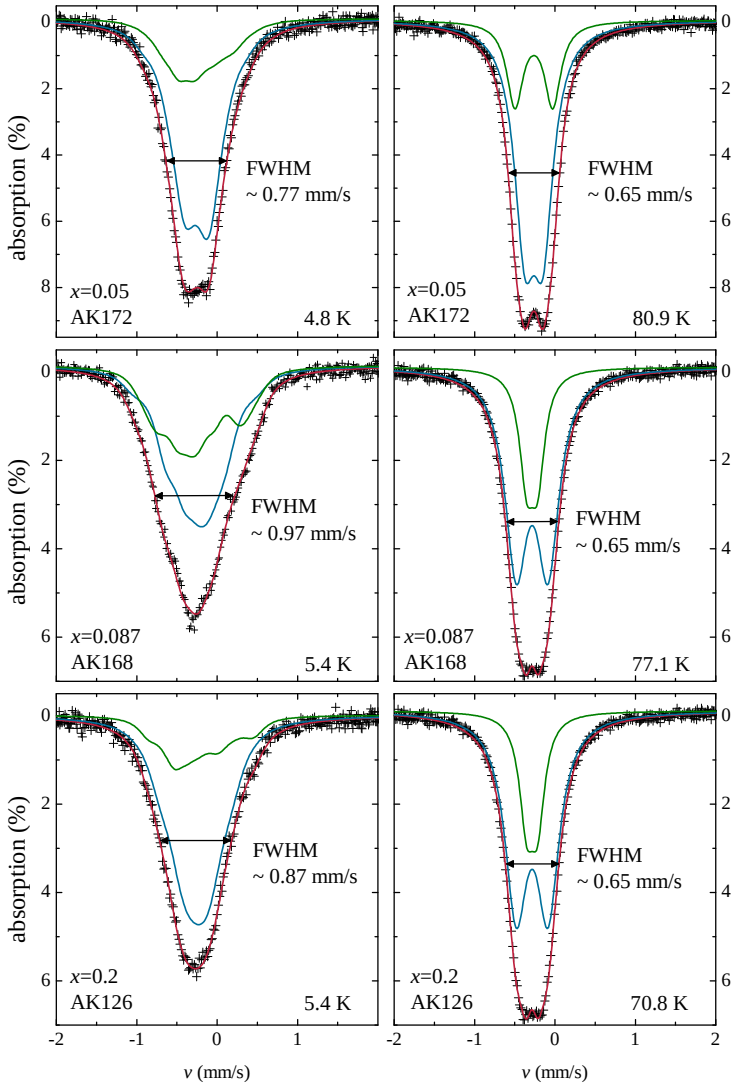

Fig. 6.8: Mössbauer absorption spectra of Ta($Fe_{1-x}V_x$)$_2$ with $x = 0.05$ (AK172), $x = 0.087$ (AK168) and $x = 0.2$ (AK126) analyzed using two subspectra for the Fe($2a$) (green) and the Fe($6h$) sites (blue), at $\sim$ 5 K (left) and $\sim$ 80 K (right).

x	T (K)	IS (mm/s)	B_{hf} (T)	ΔE_Q (mm/s)	LW (mm/s)	IS (mm/s)	B_{hf} (T)	ΔE_Q (mm/s)	LW (mm/s)
		Fe ($2a$) site $A = 75\%$, $\eta = 0$				Fe ($6h$) site $A = 25\%$, $\eta = 0.2$			
	300	-0.369	0	0.43	0.236	-0.369	0	0.23	0.277
	100	-0.268	0	0.42	0.230	-0.266	0	0.24	0.306
	80	-0.263	0	0.47	0.243	-0.262	0	0.23	0.312
AK172	50	-0.255	0	0.48	0.236	-0.254	0	0.22	0.302
	40	-0.255	0	0.49	0.227	-0.253	0	0.21	0.307
$x = 0.05$	30	-0.246	0	0.48	0.266	-0.256	0	0.25	0.297
	20	-0.255	1.217	0.42	0.232	-0.253	0.700	0.28	0.310
	12	-0.255	1.462	0.42	0.232	-0.253	0.826	0.28	0.310
	4	-0.255	1.864	0.42	0.232	-0.253	1.140	0.28	0.310
	295	-0.370	0	0.41	0.272	-0.373	0	0.24	0.275
AK168	75	-0.258	0	0.41	0.249	-0.261	0	0.24	0.283
	55	-0.258	1.159	0.41	0.249	-0.261	1.199	0.24	0.283
$x = 0.087$	15	-0.258	2.677	0.41	0.249	-0.261	1.849	0.24	0.283
	5	-0.258	2.718	0.41	0.249	-0.261	1.984	0.24	0.283
	295	-0.367	0	0.42	0.225	-0.373	0	0.19	0.301
AK126	70	-0.283	0	0.55	0.260	-0.284	0	0.22	0.321
	40	-0.253	0.342	0.55	0.260	-0.259	0.445	0.22	0.321
$x = 0.2$	15	-0.253	1.422	0.55	0.260	-0.259	1.193	0.22	0.321
	5	-0.253	1.843	0.55	0.260	-0.259	1.614	0.22	0.321

Tab. 6.2: Fitted parameters of Mössbauer absorptions spectra of Ta($Fe_{1-x}V_x)_2$, $x = 0.05, 0.087$ and 0.2 (sample numbers: AK172, AK168 and AK126) for two sites of Fe ($2a$) and Fe ($6h$) in a ratio of $1:3$.

broaden, which indicates the existence of a small magnetic hyperfine field at the Fe nucleus. Again, the fitting model described above is used with a distribution of positive free magnetic hyperfine field values for both Fe sites. B_{hf} is given by the weighted average of the corresponding hyperfine field distribution curve, as depicted in Fig. 6.9. The parameters obtained from the fit are summarized in Tab. 6.2, in particular B_{hf} is reflecting magnetic order in the samples.

The appearance of temperature dependent magnetic hyperfine fields for both Fe sites verifies long-range magnetic order in alloyed Ta(Fe$_{1-x}$V$_x$)$_2$ for $0.05 \leq x \leq 0.2$. The remarkable distribution of B_{hf} reveals not only one but several broad maxima of probability (Fig.6.9). The broadened distribution can not originate from a ordinary commensurate AFM structure, but rather suggests a possible spin density wave (SDW) modulated state.

Fig. 6.9 (a-c) also shows the weighted average of B_{hf} for both Fe sites due to the complex probability distribution. For describing the development of magnetic order and in view of the complex probability distribution of B_{hf} it appears more reasonable to neglect the distribution and only plot the weighted average B_{hf} taken from both sites. This is shown in Fig. 6.9 (a-c) by dashed lines. From this we can extrapolate magnetic transitions using a temperature dependent $B_{hf} \sim B_0 \left(1 - (T/T_N)^2\right)^n$ with $n \sim 0.5$. Thus, the determined magnetic transition temperatures of T$_N$ = 26 K, 63 K and 41 K for $x = 0.05, 0.087$ and 0.2 confirm the magnetic phase diagram (Fig. 6.1). The extrapolated B_{hf} for lowest temperatures correspond to magnetic ordered moments of less than $\mu \leq 0.2\,\mu_B/$ Fe atom.

For the fits in the SDW ordered state we had to introduce a polar angle β of the magnetic field relative to V_{zz} of $\sim 40°$ for the Fe($2a$) sites and of $\sim 65°$ for the Fe($6h$) sites. In view of the complicated probability distribution of B_{hf}, these angles also have only a weighted character and can only be considered with a large experimental error.

Furthermore, the isomer shift IS and electric quadrupole splitting ΔE_Q exhibit a similar behavior and values as given for stoichiometric TaFe$_2$ in section 6.2.1.

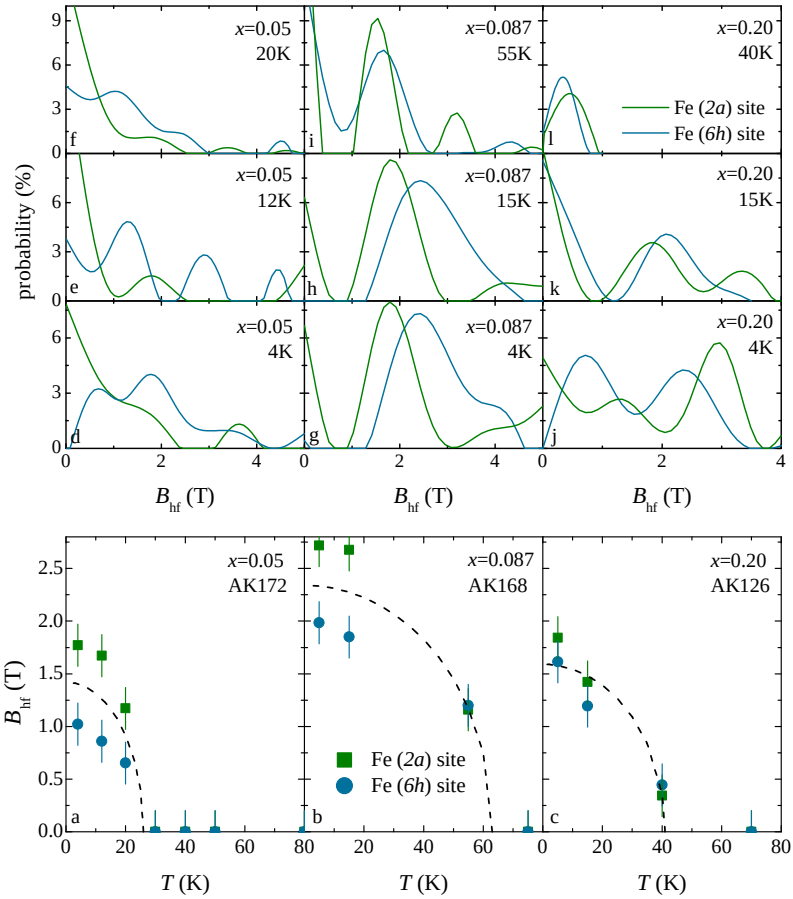

Fig. 6.9: Temperature dependence of (a-c) the weighted average of B_{hf} of $Ta(Fe_{1-x}V_x)_2$, $x = 0.05, 0.087$ and 0.2 (sample numbers: AK172, AK168 and AK126) and (d-l) the probability of magnetic hyperfine fields for Fe $(2a)$ (green) and Fe $(6h)$ (blue) sites.

6.3 Summary

Summarizing, the magnetic properties of the C14 Laves phase system $Ta(Fe_{1-x}V_x)_2$, $0.00 \leq x \leq 0.35$, reveals a complex magnetic phase diagram at low temperatures. While stoichiometric $TaFe_2$ is regarded

to be paramagnetic, doping with minor amounts of vanadium, $viz.$, Ta($Fe_{1-x}V_x$)$_2$, leads to a very unusual magnetic behavior. In alloying studies, magnetization and ^{51}V NMR measurements indicate a system close to a ferromagnetic instability for $x = 0.02$. Upon higher V concentrations up to $x = 0.3$, the experiments were interpreted in terms of Ta($Fe_{1-x}V_x$)$_2$ to undergo AFM ordering with a dome-like shape as a function of nominal increasing V content [71, 197, 198].

However, Mössbauer spectroscopy measurements cannot be accounted to show an ordinary commensurate antiferromagnetic structure, but rather suggest a spin density wave modulated order. Hence, Ta($Fe_{1-x}V_x$)$_2$ can be considered as a candidate for SDW order in the proximity of FM fluctuations. Fig. 6.10 shows the determined magnetic phase diagram, which can be divided into three regimes. For very small concentrations of V up to $x = 0.02$, the system resides close to FM instability, indicated by an enhanced magnetization at low temperatures as well as a $T^{-0.86}$ dependence of $1/T_1T$ for small fields in the ^{51}V NMR spectra. Upon further alloying, the appearance of SDW ordering with a dome-like shape of $T_N(x)$ can be assumed. For $x \geq 0.3$, the system shows paramagnetic behavior again. Altogether, V doping in Ta($Fe_{1-x}V_x$)$_2$ leads to a transformation of the system from a strongly ferromagnetic fluctuating to a paramagnetic one via a SDW dome-like regime.

In detail, we observe a paramagnetic state with a narrow doublet structure in the absorption spectra with our Mössbauer spectroscopy experiments, which reveals weak nuclear electric quadrupole interactions. With iron substituted by vanadium in $TaFe_2$ a magnetic state appears at low temperatures, whereas a line broadening of the doublet structure with a magnetic hyperfine field distributions occurs. This excludes itinerant antiferromagnetism, but rather suggests a SDW ordering for vanadium concentrations of $0.04 \leq x \leq 0.27$ in Ta($Fe_{1-x}V_x$)$_2$. Itinerant antiferromagnetism would expect discrete magnetic hyperfine fields. The weighted average of magnetic hyperfine fields leads to an estimation for a magnetic ordering moment of about $0.2\,\mu_B$ per Fe atom. Unfortunately, such small fields

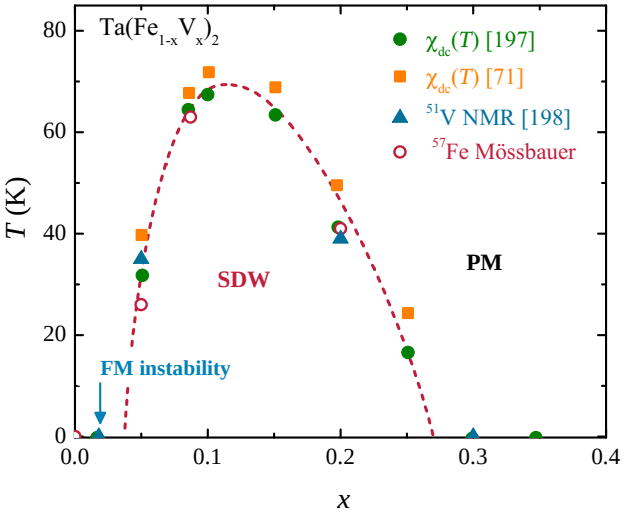

Fig. 6.10: The determined magnetic phase diagram for slightly alloyed $Ta(Fe_{1-x}V_x)_2$ exhibits FM fluctuations at $x = 0.02$ and a spin density wave (SDW) modulated state in the range $0.05 \leq x \leq 0.25$, in contrast to Refs. [71, 197, 198]

prevent a strong line splitting to analyze magnetic hyperfine field with detailed information. Mössbauer spectroscopy under high magnetic fields could be a better option. Nevertheless, a complex magnetic phase diagram of $Ta(Fe_{1-x}V_x)_2$ is detected including Mössbauer spectroscopy, bulk and ^{51}V NMR measurements [71, 198].

However, in stoichiometric $TaFe_2$ and with very weak vanadium concentrations, $x \leq 0.04$, the SDW modulated magnetic state is suppressed. In contrast to bulk measurements (e.g. susceptibility) and ^{51}V NMR studies no ferromagnetic order can be detected. At this point other techniques (e.g. μSR) should be performed to exclude effects of inhomogeneous samples.

In comparison, $Ta(Fe_{1-x}V_x)_2$ reveals a common behavior as observed in $Nb_{1-y}Fe_{2+y}$ with similar order of magnitude of the electric quadrupole doublets in Mössbauer absorptions spectra, whereas both systems exhibit low magnetic ordering moments of a SDW modulated magnetic state. Fur-

thermore, $Nb_{1-y}Fe_{2+y}$ induces a ferromagnetic quantum critical point (FM QCP) at the transition of FM via the SDW phase at $y \sim -0.01$ (cf. section 5.2.2). Similarly, a FM QCP for $x \sim 0.02$ would also be conceivable, because of the large Stoner enhancement factor of the order of 240 and ferromagnetic instability in Ta($Fe_{0.98}V_{0.02}$)$_2$.

All in all, the magnetic properties of these compounds are not fully understood yet, but with the detection of the magnetic hyperfine field distribution in Mössbauer spectroscopy experiments, it seems to be clear that the magnetic dome-like phase is a SDW modulated magnetic state for $0.04 \leq x \leq 0.27$. In dependence of increasing vanadium concentrations for $0.0 \leq x \leq 0.04$ weak FM fluctuations might be suppressed by the SDW state, with a possible FM QCP around $x \sim 0.02$.

7 Conclusion and outlook

In this thesis concentration-dependent magnetic phase diagrams have been studied regarding the quantum critical properties in the $4f$-electronic system $CePt_3B_{1-x}Si_x$ and in the $3d$-electronic systems, $Nb_{1-y}Fe_{2+y}$ and $Ta(Fe_{1-x}V_x)_2$. All compounds reveal ferromagnetic instabilities that affect extraordinary physical ground state properties of strong electronic correlations, which might originate from quantum critical behavior or unconventional superconductivity. Due to this remarkable behavior a combined study on a macroscopic and microscopic scale via measurements of thermodynamic, transport, muon spin relaxation (μSR) and Mössbauer spectroscopy experiments has been carried out.

In certain cases, these metals show magnetic ground states differing from the Landau Fermi liquid model in their thermodynamic and transport properties, what indicates a quantum critical behavior in most cases [5–9, 11–14]. Moreover, the antiferromagnetic $CePt_3B_{1-x}Si_x$ shows a weak ferromagnetic behavior for high boron concentrations, which is induced as a result of the Dzyahloshinskii-Moriya interaction in a noncentrosymmetric system. In stoichiometric $CePt_3Si$ the ferromagnetic behavior is suppressed completely and unconventional superconductivity occurs [15, 16, 205]. In comparison, $Nb_{1-y}Fe_{2+y}$ exhibits a more complex magnetic phase diagram including a quantum critical point at $y = -0.015$ Nb-excess surrounded by a spin density wave modulated state and ferromagnetic states with very low magnetic moments of one tenth μ_B per iron atoms. Recent studies revealed deviations from the Landau Fermi liquid in thermodynamic and transport properties with quantum critical behavior for $NbFe_2$ [17–19]. The spin density wave modulated state was

disputed for a long time. These issues of such remarkable behavior are resolved by muon spin relaxation and Mössbauer experiments, which confirmed the spin density wave modulated state near a ferromagnetic quantum critical point in $Nb_{1-y}Fe_{2+y}$ for the first time. Furthermore, studies on $Ta(Fe_{1-x}V_x)_2$, which is isostructural to $NbFe_2$, has been studied in the context of ferromagnetic instabilities, while vanadium substitution induces also magnetic ground state properties with a similar behavior to $Nb_{1-y}Fe_{2+y}$ [71].

The main focus of this study was the investigation of the magnetic properties on a microscopic scale as a function of temperature and external magnetic fields by muon spin relaxation (μSR) and Mössbauer spectroscopy. The local magnetic environment with its static or dynamic character of the electronic or nuclei magnetic fields in the sample is observed by μSR measurements. Implanted muons in magnetically ordered materials precess with an oscillatory frequency, which is proportional to the local internal magnetic fields in the investigated sample. The large magnetic moments of the muons make the measurements very sensitive to extremely small magnetic fields [115]. Even smallest magnetic moments of one tenth μ_B per iron atoms and fast spin fluctuations at the quantum critical point can be detected in $Nb_{1-y}Fe_{2+y}$. ^{57}Fe Mössbauer spectroscopy is performed to examine iron-based magnetic structures. Analyzing the magnetic hyperfine structure allows the investigation of the ^{57}Fe nuclei and their electronic environment by the detection of local magnetic fields. In addition, the Coulomb interaction between nuclear and electronic charge distribution can be determined by the electric quadrupole moments of the electric field gradient subjected to the nucleus.

In the first part of this thesis the magnetic phase diagram of the alloying series of the $4f$-electronic system $CePt_3B_{1-x}Si_x$, $0.0 \leq x \leq 1.0$, is determined by means of bulk and microscopic measurements detecting an antiferromagnetic, ferromagnetic and superconducting state. The antiferromagnet $CePt_3B$ ($T_N = 7.8$ K) performs a continuous transformation

from the antiferromagnetic phase into the heavy fermion superconductor $CePt_3Si$ ($T_N = 2.2$ K), with a smooth suppression of the Néel temperature T_N. The weakly ferromagnetic contribution of $CePt_3B$ is completely suppressed with the substitution of boron by silicon at a critical value of $x_c \sim 0.8$. Weakly ferromagnetic behavior occurs as a result of the Dzyahloshinskii-Moriya (DM) interaction in non-centrosymmetric systems by canting of antiferromagnetically ordered spins. With the complete suppression of the weakly ferromagnetic state unconventional superconductivity occurs in $CePt_3Si$ ($T_c = 0.75$ K). Replacing boron by silicon represents a chemical pressure study within the concept of the Doniach phase diagram, which considers the competition of long-range magnetic order from an RKKY-like exchange (T_{RKKY}) and the Kondo effect (T_K) with energy scales of $T_K \sim 10$ K and $T_{RKKY} \sim 25 - 45$ K. With increasing Si the Kondo effect is enhanced and tends to win over the magnetic order as evidenced of a significant enhancement of electronic correlations in the heavy fermion superconductor $CePt_3Si$. Moreover, μSR and magnetization experiments reveal a suppression of the ferromagnetic fluctuations in $CePt_3B$ on behalf of antiferromagnetic fluctuations. This change might suggest that the magnetic fluctuation spectrum is an element relevant for superconductivity in $CePt_3Si$. Further, the increasing silicon concentration leads to an increase of the lattice parameters and exerts a negative chemical pressure, while the increasing electron number counteracts this pressure. In consequence, the magnetic properties change with the substitution of B by Si, and thus affect the density of states at the Fermi level. Therefore, $CePt_3B$ can be seen as a low pressure variant of $CePt_3Si$. Pressure studies up to 5.5 GPa of $CePt_3B$ confirm this assumption. $CePt_3B$ shows only a slight increase of the ferromagnetic transition temperature for $p \leq 1$ GPa with a following constant ferromagnetic contribution at a pressure of 1 GPa $\leq p \leq 5.5$ GPa. In contrast, the magnetic phase for $CePt_3Si$ is already suppressed at $p = 0.6$ GPa. Within the concept of the Doniach model, this reflects that $CePt_3B$ is a local moment system. A more detailed understanding

of the unconventional superconductor $CePt_3Si$ could not be achieved within this study. The analyzed system $CePt_3B_{1-x}Si_x$ with the alloying steps of $20\,\%$ exhibits no superconductivity and no phase transition from the the weakly ferromagnetic state into superconductivity. The weakly ferromagnetic state is suppressed for $y_c \approx 0.8$ far away from the superconductor $CePt_3Si$. Further studies at lowest temperatures with a smaller gradation of Si concentration close to $0.7 \leq x \leq 1.0$ are required for a detailed analysis of the magnetic instability and its correlation with unconventional superconductivity.

In the second part of this thesis the $3d$- transition metallic system $Nb_{1-y}Fe_{2+y}$, $-0.019 \leq y \leq -0.004$, was analyzed by means of μSR, Mössbauer spectroscopy and bulk measurements in high magnetic fields. For a long time the complex magnetic phase diagram with a presumed spin density wave modulated phase surrounded by ferromagnetic states and a quantum critical point at $1.5\,\%$ niobium excess was discussed. Now, microscopic studies confirm the suspected SDW phase with a totally magnetic ordered ground state at low temperatures for the first time. The SDW states are detected with a wide field distribution of an overdamped zero field μSR asymmetry signal in contrast to a spontaneous muon rotation signal of ferromagnetism. The magnetic state of Fe-rich $NbFe_2$ was identified to be ferromagnetic with an upper limit of the ordered magnetic moment of about $0.15\,\mu_B$/Fe atom by a combination of the results of μSR and Mössbauer spectroscopy measurements. Further, local internal fields in the μSR experiments lead to precession frequencies of muons at their stopping sites, which depend on the size of the magnetically ordered moment of the ferromagnetic and spin density wave modulated states. The extrapolated evolution of the magnetic moments with the sample composition proves a fully suppressed magnetic moment at $y_c \sim -0.006 \pm 0.001$. This is distinctly different from the value $y_c = -0.015$ at the QCP obtained from bulk magnetometry. This raises the question about the nature of the magnetically ordered phase in the in-

termediate range $-0.006 \leq y \leq y_c$, and the possibility of the occurrence of a partially ordered phase [14, 206] close to a ferromagnetic quantum critical point with SDW modulated magnetic order. Furthermore, the examination of $Nb_{1-y}Fe_{2+y}$, $y = -0.0117$, close to the quantum critical point reveals a qualitatively different behavior to the observed SDW state in μSR experiments at low temperatures down to 0.02 K. In contrast to the non-magnetic asymmetry signal an additional fluctuation at a very short time scale ($t \leq 0.4\,\mu s$) was detected. This unusual observation might indicate a signature for ferromagnetic quantum criticality, in view of the results of bulk studies [17], and which has to be clarified in further theoretical and experimental investigations. In the context of this thesis ferromagnetic instabilities are verified in $Nb_{1-y}Fe_{2+y}$, being replaced by a spin density wave modulated state next to a FM QCP as described in Ref. [103]. To clarify the magnetic structure in detail we are looking forward to the latest inelastic neutron scattering experiments of P. Niklowitz. First results of inelastic neutron spectra show unusual temperature-dependent, strong quasielastic scattering near the vector $\mathbf{q_1}$ in the vicinity of (002) [207]. This might indicate the scenario of a ferromagnetic quantum critical point, which is masked by emerging modulated magnetic order. Alternatively, one might use further μSR studies to gain deeper insight into the physics of $NbFe_2$. Here, what would be required is a.) a determination of the muon stopping site, which would allow more accurate fits to describe the experimental data, and b.) a detailed study of the field and temperature dependence of the different relaxation times.

In the last part of this thesis the isoelectronic C14 Laves phase $TaFe_2$, which has approximately the same $3d$-electron counts and only slightly smaller lattice parameters than $NbFe_2$, was studied. The magnetic phase diagram of the alloyed system $Ta(Fe_{1-x}V_x)_2$, $0.0 \leq x \leq 0.2$, was investigated by ^{57}Fe Mössbauer spectroscopy and thermodynamic experiments. While stoichiometric $TaFe_2$ is paramagnetic with weak ferromagnetic fluctuations, the compositional phase diagram exhibits a ferromagnetic

instability for a vanadium concentration of $x = 0.02$. Larger substitutions of iron by vanadium generate a magnetically ordered ground state in the regime of $0.04 \leq x \leq 0.27$. The ^{57}Fe Mössbauer absorption spectra reveal a magnetic hyperfine field distribution undergoing a line broadening of the electronic doublet structure, indicating low magnetic moments of the order of $0.2\,\mu_B$ per Fe atoms. The magnetic hyperfine fields resulting from these moments were analyzed as a distribution function, indicating a spin density wave modulated magnetic ground state for $0.04 \leq x \leq 0.27$ with slightly larger magnetic moments than in $Nb_{1-y}Fe_{2+y}$. In a next step, ^{57}Fe Mössbauer experiments with applied magnetic fields are expected to split the magnetic hyperfine field of ^{57}Fe nucleus, which could clarify the nature of the spin density wave modulated state.

Altogether, $Ta(Fe_{1-x}V_x)_2$ and $Nb_{1-y}Fe_{2+y}$ reveal a common behavior with similar spin wave modulated states of very low magnetic moments $\mu_{ord} \leq 0.1\,\mu_B/$ Fe atom. $Nb_{1-y}Fe_{2+y}$ reveals a ferromagnetic quantum critical point at the transition from a ferromagnetic phase into a spin density wave modulated state of second order at $y \sim -0.01$. The ferromagnetic instability in $Ta(Fe_{0.98}V_{0.02})_2$ also implies a FM QCP close to a SDW state. For the future, this scenario of a ferromagnetic quantum critical point needs more examination both from the theoretical and experimental side. In contrast, in the magnetic phase diagram of $CePt_3B_{1-x}Si_x$ no quantum critical point is observed, while the suppression of the weakly ferromagnetic state is accompanied by the formation of unconventional superconductivity.

List of Figures

List of Tables

Bibliography

[1] L. D. Landau, Soviet Physics JETP **3**, 920 (1957).

[2] L. D. Landau, Soviet Physics JETP **5**, 101 (1957).

[3] L. D. Landau, Soviet Physics JETP **8**, 70 (1959).

[4] W. Heisenberg, Z.Phys **43**, 172 (1927).

[5] G. R. Stewart, Rev. Mod. Phys. **56**, 755 (1984).

[6] G. R. Stewart, Rev. Mod. Phys. **73**, 797 (2001).

[7] N. D. Mathur, F. M. Grosche, S. R. Julian, I. R. Walker, D. M. Freye, R. K. W. Haselwimmer, and G. G. Lonzarich, Nature **394**, 39 (1998).

[8] F. Steglich, J. Aarts, C. D. Bredl, W. Lieke, D. Meschede, W. Franz, and H. Schäfer, Phys. Rev. Lett. **43**, 1892 (1979).

[9] H. Pfau, S. Hartmann, U. Stockert, P. Sun, S. Lausberg, M. Brando, S. Friedemann, C. Krellner, C. Geibel, S. Wirth, S. Kirchner, E. Abrahams, Q. Si, and F. Steglich, Nature **484**, 493 (2012).

[10] H. v. Löhneysen, A. Rosch, M. Vojta, and P. Wölfle, Rev. Mod. Phys. **79**, 1015 (2007).

[11] P. Gegenwart, Q. Si, and F. Steglich, Nature Phys. **4**, 186 (2008).

[12] S. Friedemann, N. Oeschler, S. Wirth, C. Krellner, C. Geibel, F. Steglich, S. Paschen, S. Kirchner, and Q. Si, Proc. Natl. Acad. Sci. USA **107**, 14547 (2010).

[13] Y. Muraoka, M. Shiga, and Y. Nakamura, J. Phys. Soc. Jpn. **40**, 905 (1976).

[14] C. Pfleiderer, L. Pintschovius, H. v. Löhneysen, M. Garst, and A. Rosch, Nature **427**, 227 (2004).

[15] E. Bauer, G. Hilscher, H. Michor, C. Paul, E. W. Scheidt, A. Gribanov, Y. Seropegin, H. Noël, M. Sigrist, and P. Rogl, Phys. Rev. Lett. **92**, 027003 (2004).

[16] S. Süllow, G. Nieuwenhuys, A. Menovsky, and J. Mydosh, Physica B: Condens. Matter **199&200**, 644 (1994).

[17] M. Brando, W. J. Duncan, D. Moroni-Klementowicz, C. Albrecht, D. Grüner, R. Ballou, and F. M. Grosche, Phys. Rev. Lett. **101**, 026401 (2008).

[18] D. Moroni-Klementowicz, M. Brando, C. Albrecht, W. J. Duncan, F. M. Grosche, D. Grüner, and G. Kreiner, Phys. Rev. B **79**, 224410 (2009).

[19] D. A. Tompsett, R. J. Needs, F. M. Grosche, and G. G. Lonzarich, Phys. Rev. B **82**, 155137 (2010).

[20] Y. Yamada, J. Armitage, R. Graham, and P. Riedi, J. Magn. Magn. Mat. **104–107**, 1317 (1992), proceedings of the International Conference on Magnetism, Part {II}.

[21] W. J. Duncan, O. P. Welzel, D. Moroni-Klementowicz, C. Albrecht, P. G. Niklowitz, D. Grüner, M. Brando, A. Neubauer, C. Pfleiderer, N. Kikugawa, A. P. Mackenzie, and F. M. Grosche, Phys. Status Solidi B **247**, 544 (2010).

[22] A. J. Schofield, Contemporary Physics **40**, 95 (1999).

[23] H. Schulz, *Fermi liquids and non-Fermi liqiuds*, in E. Akkermans, G. Montambaux, J. Pichard, J. Zinn-Justin, *Proceedings of Les Houches Summer Scholl LXI*, Elsevier, Amsterdam, 533 (1995).

[24] G. Fritsch, Physik in unserer Zeit **18**, 17 (1987).

[25] S. Doniach, Physica B+C **91**, 231 (1977).

[26] P. Coleman, *Heavy Fermions: Electrons at the Edge of Magnetism*, John Wiley & Sons, Ltd (2007).

[27] A. Schröder, G. Aeppli, R. Coldea, M. Adams, O. Stockert, H. v. Löhneysen, E. Bucher, R. Ramazashvili, and P. Coleman, Nature **407**, 351 (2000).

[28] O. Trovarelli, C. Geibel, S. Mederle, C. Langhammer, F. M. Grosche, P. Gegenwart, M. Lang, G. Sparn, and F. Steglich, Phys. Rev. Lett. **85**, 626 (2000).

[29] J. Kondo, Progr. Theor. Phys. **32**, 37 (1964).

[30] C. Enss and S. Hunklinger, *Tieftemperaturphysik*, Springer-Verlag, Berlin, Heidelberg (2000).

[31] M. A. Ruderman and C. Kittel, Phys. Rev. **96**, 99 (1954).

[32] T. Kasuya, Progr. Theor. Phys. **16**, 58 (1956).

[33] M. Jourdan, M. Huth, and H. Adrian, Nature **398**, 47 (1999).

[34] E. Dagotto, Rev. Mod. Phys. **66**, 763 (1994).

[35] K. Ishida, H. Mukuda, Y. Kitaoka, K. Asayama, Z. Q. Mao, Y. Mori, and Y. Maeno, Nature **396**, 658 (1998).

[36] D. Jérome, A. Mazaud, M. Ribault, and K. Bechgaard, J. Physique Lett. **41**, 95 (1980).

[37] K. Bechgaard, K. Carneiro, M. Olsen, F. B. Rasmussen, and C. S. Jacobsen, Phys. Rev. Lett. **46**, 852 (1981).

[38] Y. Kamihara, T. Watanabe, M. Hirano, and H. Hosono, J. Am. Chem. Soc **130**, 3296 (2008).

[39] A. Subedi, L. Zhang, D. J. Singh, and M. H. Du, Phys. Rev. B **78**, 134514 (2008).

[40] J. Bardeen, L. N. Cooper, and J. R. Schrieffer, Phys. Rev. **108**, 1175 (1957).

[41] W. Buckel and R. Kleiner, *Supraleitung: Grundlagen und Anwendungen*, 6. Auflage, Wiley-VCH Verlag, Weinheim (2007).

[42] P. Thalmeier, M. Jourdan, and M. Huth, Physik Journal **1**, 51 (2002).

[43] M. R. Norman, *Unconventional superconductivity*, in K.-H. Bennemann and J. B. Ketterson, *Novel superfluids*, Oxford University Press **2**, 592 (2014), preprint arXiv:cond-mat.supr-con/1302.3176.

[44] T. Kawai, H. Muranaka, M.-A. Measson, T. Shimoda, Y. Doi, T. D. Matsuda, Y. Haga, G. Knebel, G. Lapertot, D. Aoki, J. Flouquet, T. Takeuchi, R. Settai, and Y. Ōnuki, J. Phys. Soc. Jpn. **77**, 064716 (2008).

[45] H. R. Ott, H. Rudigier, Z. Fisk, and J. L. Smith, Phys. Rev. Lett. **50**, 1595 (1983).

[46] N. Kimura, K. Ito, K. Saitoh, Y. Umeda, H. Aoki, and T. Terashima, Phys. Rev. Lett. **95**, 247004 (2005).

[47] I. Sugitani, Y. Okuda, H. Shishido, T. Yamada, A. Thamizhavel, E. Yamamoto, T. D. Matsuda, Y. Haga, T. Takeuchi, R. Settai, and Y. Ōnuki, J. Phys. Soc. Jpn. **75**, 043703 (2006).

[48] E. Bauer, H. Kaldarar, A. Prokofiev, E. Royanian, A. Amato, J. Sereni, W. Brämer-Escamilla, and I. Bonalde, J. Phys. Soc. Jpn. **76**, 051009 (2007).

[49] P. A. Frigeri, D. F. Agterberg, A. Koga, and M. Sigrist, Phys. Rev. Lett. **92**, 097001 (2004).

[50] P. A. Frigeri, D. F. Agterberg, and M. Sigrist, New J. Phys. **6**, 115 (2004).

[51] K. V. Samokhin, E. S. Zijlstra, and S. K. Bose, Phys. Rev. B **69**, 094514 (2004).

[52] F. Laves, Naturwissenschaften **27**, 65 (1939).

[53] P. Villars and L. D. Calvert, *Pearson's Handbook of Crystallographic Data for Intermetallic Phases*, American Society for Metals International, Materials, Ohio, **1-4**, 2 edition (1991).

[54] G. Sauthoff, *Intermetallics*, VCH, Weinheim (1995).

[55] F. Stein, M. Palm, and G. Sauthoff, Intermetallics **12**, 713 (2004).

[56] U. Müller, *Anorganische Strukturchemie*, 6. Auflage, Viewieg+Teubner, GWV Fachverlage GmbH, Wiesbaden (2008).

[57] F. C. Frank and J. S. Kasper, Acta Crystallogr. **11**, 184 (1958).

[58] F. C. Frank and J. S. Kasper, Acta Crystallogr. **12**, 483 (1959).

[59] F. Stein, M. Palm, and G. Sauthoff, Intermetallics **13**, 1056 (2005).

[60] G. E. R. Schulze, Z. Elektrochem. **45**, 849 (1939).

[61] D. Andrae, B. Paulus, U. Wedig, and M. Jansen, Z. Anorg. Allg. Chem. **639**, 1963 (2013).

[62] D. J. Thoma and J. H. Perepezko, J. Alloys Comp. **224**, 330 (1995).

[63] G. Hilscher, J. Magn. Magn. Mat. **27**, 1 (1982).

[64] X.-Q. Chen, W. Wolf, R. Podloucky, P. Rogl, and M. Marsman, Phys. Rev. B **72**, 054440 (2005).

[65] S. Asano and S. Ishida, J. Magn. Magn. Mat. **70**, 187 (1987).

[66] M. Crook, *Spin fluctuations and itinerant magnetism in hexagonal Laves phase $NbFe_2$ and related compounds*, Ph.D. thesis, University of Reading (1995).

[67] S. Asano and S. Ishida, J . Phys. F: Met. Phys. **18**, 501 (1988).

[68] P. Gegenwart, T. Westerkamp, C. Krellner, Y. Tokiwa, S. Paschen, C. Geibel, F. Steglich, E. Abrahams, and Q. Si, Science **315**, 969 (2007).

[69] C. Zhang, Z. Zhang, S. Wang, H. Li, J. Dong, N. Xing, Y. Guo, and W. Li, J. Alloys Comp. **448**, 53 (2008).

[70] H. R. Rechenberg, L. Morellon, P. A. Algarabel, and M. R. Ibarra, Phys. Rev. B **71**, 104412 (2005).

[71] Y. Horie, S.-i. Kawashima, Y. Yamada, G. Obara, and T. Nakamura, J. Phys.: Conf. Ser. **200**, 032078 (2010).

[72] A. Subedi and D. J. Singh, Phys. Rev. B **81**, 024422 (2010).

[73] M. R. Crook and R. Cywinski, Hyp. Int. **85**, 203 (1994).

[74] D. Moroni-Klementowicz, R. Burrell, D. Fort, and F. M. Grosche, Physica B **359-361**, 80 (2005).

[75] R. Ballou, Can. J. Phys. **79**, 1475 (2001).

[76] T. Sakai and H. Nakano, Phys. Rev. B **83**, 100405(R) (2011).

[77] O. A. Starykh, Rep. Prog. Phys. **78**, 052502 (2015).

[78] Y. Nishira and Y. Yamaguchi, J. Phys. Soc. Jpn. **52**, 3630 (1983).

[79] Y. Nishira and Y. Yamaguchi, J. Phys. Soc. Jpn. **54**, 1122 (1985).

[80] T. Vojta, Ann. Phys. (Leipzig) **9**, 403 (2000).

[81] S. Sachdev, *Quantum phase transitions*, Cambridge University Press, Cambridge, 2. edition (2011).

[82] P. Ehrenfest, 36. Verhandlingen der Koninklijke Akademie van Wetenschappen, Amsterdam, 153–157, Communications from the Physical Laboratory of the University of Leiden, **75b** (1933).

[83] W. Nolting, *Grundkurs, Theoretische Physik, 6. Statistische Physik*, Vieweg Lehrbuch (1998).

[84] M. Vojta, Rep. Prog. Phys. **66**, 2069 (2003).

[85] M. Vojta, Physik Journal **1**, 55 (2002).

[86] D. Belitz, T. R. Kirkpatrick, and J. Rollbühler, Phys. Rev. Lett. **94**, 247205 (2005).

[87] N. Doiron-Leyraud, I. Walker, L. Taillefer, M. Steiner, S. R. Julian, and G. Lonzarich, Nature **425**, 595 (2003).

[88] M. Uhlarz, C. Pfleiderer, and S. M. Hayden, Phys. Rev. Lett. **93**, 256404 (2004).

[89] O. Stockert, H. v. Löhneysen, A. Rosch, N. Pyka, and M. Loewenhaupt, Phys. Rev. Lett. **80**, 5627 (1998).

[90] F. Grosche, I. Walker, S. Julian, N. Mathur, D. Freye, M. Steiner, and G. Lonzarich, J. Phys.: Condens. Matter **13**, 2845 (2001).

[91] G. R. Stewart, Rev. Mod. Phys. **78**, 743 (2006).

[92] J. A. Hertz, Phys. Rev. B **14**, 1165 (1976).

[93] A. J. Millis, Phys. Rev. B **48**, 7183 (1993).

[94] T. Moriya and T. Takimoto, J. Phys. Soc. Jpn. **64**, 960 (1995).

[95] Q. Si, M. S. Rabello, K. Ingersent, and J. L. Smith, Nature **413**, 804 (2001).

[96] T. Moriya, *Self-Consistent Renormalization (SCR) Theory of Spin Fluctuations*, in *Spin Fluctuations in Itinerant Electron Magnetism*,

Springer Series in Solid-State Sciences, Berlin Heidelberg, **56**, 44–81 (1985).

[97] P. Coleman, C. Pépin, Q. Si, and R. Ramazashvili, J. Phys.: Condens. Matter **13** (35), R723 (2001).

[98] M. Vojta, Phys. Rev. B **78**, 125109 (2008).

[99] Q. Si and F. Steglich, Science **329**, 1161 (2010).

[100] Q. Si, *Quantum Criticality and the Kondo Lattice*, in L. D. Carr, *Understanding Quantum Phase Transitions*, (2010).

[101] L. Zhu, M. Garst, A. Rosch, and Q. Si, Phys. Rev. Lett. **91**, 066404 (2003).

[102] A. Steppke, R. Küchler, S. Lausberg, E. Lengyel, L. Steinke, R. Borth, T. Lühmann, C. Krellner, M. Nicklas, C. Geibel, F. Steglich, and M. Brando, Science **339**, 933 (2013).

[103] D. Belitz and T. R. Kirkpatrick (2012), preprint arXiv:cond-mat.str-el/1204.0873.

[104] V. Taufour, D. Aoki, G. Knebel, and J. Flouquet, Phys. Rev. Lett. **105**, 217201 (2010).

[105] E. A. Yelland, J. M. Barraclough, W. Wang, K. V. Kamenev, and A. D. Huxley, Nature Physics **7**, 890 (2011).

[106] M. Otero-Leal, F. Rivadulla, M. García-Hernández, A. Piñeiro, V. Pardo, D. Baldomir, and J. Rivas, Phys. Rev. B **78**, 180415 (2008).

[107] D. Belitz, T. R. Kirkpatrick, and T. Vojta, Phys. Rev. Lett. **82**, 4707 (1999).

[108] G. J. Conduit, A. G. Green, and B. D. Simons, Phys. Rev. Lett. **103**, 207201 (2009).

[109] K. Gramm, L. Lundgren, and O. Beckmann, Phys. Scripta **13**, 93 (1976).

[110] J. Magnusson, C. Djurberg, P. Granberg, and P. Nordblad, Rev. Sci. Instrum. **68**, 3761 (1997).

[111] T. M. Dauphinee and E. Mooser, Rev. Sci. Instrum. **26** (7), 660 (1955).

[112] K. A. Borup, E. S. Toberer, L. D. Zoltan, G. Nakatsukasa, M. Errico, J.-P. Fleurial, B. B. Iversen, and G. J. Snyder, Rev. Sci. Instrum. **83** (12), 123902 (2012).

[113] R. Bachmann, F. J. DiSalvo, T. H. Geballe, R. L. Greene, R. E. Howard, C. N. King, H. C. Kirsch, K. N. Lee, R. E. Schwall, H.-U. Thomas, and R. B. Zubeck, Rev. Sci. Instrum. **43**, 205 (1972).

[114] F. Pobell, *Matter and Methods at Low Temperatures*, Springer-Verlag, Berlin, Heidelberg, 2. edition (1996).

[115] S. Blundell, *Magnetism in Condensed Matter*, Oxford University Press (2008).

[116] G. Schatz, A. Weidinger, and M. Deicher, *Nukleare Festkörperphysik: Kernphysikalische Messmethoden und ihre Anwendungen*, 4. überarb. Auflage, Wiesbaden : Vieweg + Teubner (2010).

[117] A. Abragam and B. Bleaney, *Electron Paramagnetic Resonance of Transition Ions*, Dover (1986).

[118] A. Abragam, *The principles of nuclear magnetism*, Oxford University Press (1961).

[119] A. S. Oja and O. V. Lounasmaa, Rev. Mod. Phys. **69** (1997).

[120] G. K. Wertheim, *Mössbauer Effect: Priniciples and Applications*, Akademic Press (1964).

[121] M. T. Dove, *Structure and Dynamics –An Atomic View of Materials*, Oxford University Press (2003).

[122] S. J. Blundell, Contemporary Physics **40**, 175 (1999).

[123] T. D. Lee and C. N. Yang, Phys. Rev. **104**, 254 (1956).

[124] R. L. Garmin, L. M. Ledermann, and M. Weinrich, Phys. Rev. **105**, 1415 (1957).

[125] J. I. Friedman and V. L. Telegdi, Phys. Rev. **105**, 1681 (1957).

[126] A. Schenck, *Muon Spin Rotation Spectroscopy*, Adam Hilger Ltd, Bristol (1985).

[127] A. Amato, Rev. Mod. Phys. **69**, 4 (1997).

[128] P. Dalmas de Réotier and A. Yaouanc, J. Phys.: Condens. Matter **9**, 9113 (1997).

[129] R. S. Hayano, Y. J. Uemura, J. Imatato, N. Nishida, T. Yamazaki, and R. Kubo, Phys. Rev. B **20**, 850 (1979).

[130] J. Major, J. Mundy, M. Schmolz, A. Seeger, K. Döring, K. Fürderer, M. Gladisch, D. Herlach, and G. Majer, Hyp. Int. **31**, 259 (1986).

[131] L. P. Le, A. Keren, G. M. Luke, B. J. Sternlieb, W. D. Wu, Y. J. Uemura, J. H. Brewer, T. M. Riseman, R. V. Upasani, L. Y. Chiang, W. Kang, P. M. Chaikin, T. Csiba, and G. Grüner, Phys. Rev. B **48**, 7284 (1993).

[132] L. Le, R. Heffner, J. Thompson, G. Nieuwenhuys, D. Maclaughlin, P. Canfield, B. Cho, A. Amato, R. Feyerherm, F. Gygax, and A. Schenck, Hyp. Int. **104**, 49 (1997).

[133] A. Keren, Phys. Rev. B **50**, 10039 (1994).

[134] P. Dalmas de Réotier and A. Yaouanc, J. Phys.: Condens. Matter **4**, 4533 (1992).

[135] R. Mössbauer, Z. Phys. **151**, 124 (1958).

[136] H. Wegener, *Der Mößbauer-Effekt und seine Anwendung in Physik und Chemie*, 2. Auflage, Bibliographisches Institut Mannheim Hochschultaschenbücher-Verlag (1966).

[137] P. Gütlich, Chem. Unserer Zeit **4**, 133 (1970).

[138] D. Barb, *Grundlagen und Anwendungen der Mössbauerspektroskopie*, Akademie-Berlag, Berlin (1980).

[139] M. Sigrist and K. Ueda, Rev. Mod. Phys. **63**, 239 (1991).

[140] C. Pfleiderer, Rev. Mod. Phys. **81**, 1551 (2009).

[141] S. Hashimoto, T. Yasuda, T. Kubo, H. Shishido, T. Ueda, R. Settai, T. D. Matsuda, Y. Haga, H. Harima, and Y. Ōnuki, J. Phys.: Condens. Matter **16**, L287 (2004).

[142] P. W. Anderson, Phys. Rev. B **30**, 7 (1984).

[143] N. Metoki, K. Kaneko, T. D. Matsuda, A. Galatanu, T. Takeuchi, S. Hashimoto, T. Ueda, R. Settai, Y. Ōnuki, and N. Bernhoeft, J. Phys.: Condens. Matter **16**, L207 (2004).

[144] M. Yogi, Y. Kitaoka, S. Hashimoto, T. Yasuda, R. Settai, T. D. Matsuda, Y. Haga, Y. Ōnuki, P. Rogl, and E. Bauer, Phys. Rev. Lett. **93**, 027003 (2004).

[145] E. Bauer, I. Bonalde, and M. Sigrist, J. Low Temp. Phys. **37**, 748 (2005).

[146] R. Lackner, M. Sieberer, H. Michor, G. Hilscher, E. Bauer, P. S. Salamakha, O. L. Sologub, and K. Hiebl, J. Phys.: Condens. Matter **17** (11), S905 (2005).

[147] T. Takeuchi, T. Yasuda, M. Tsujino, H. Shishido, R. Settai, H. Harima, and Y. Ōnuki, J. Phys. Soc. Jpn. **76** (1), 014702 (2007).

[148] M. Nicklas, F. Steglich, J. Knolle, I. Eremin, R. Lackner, and E. Bauer, Phys. Rev. B **81**, 180511 (2010).

[149] Y. Aoki, A. Sumiyama, G. Motoyama, Y. Oda, T. Yasuda, R. Settai, and Y. Ōnuki, Physica C **470**, S554 (2010).

[150] K. Kaneko, O. Stockert, B. Fåk, S. Raymond, M. Skoulatos, T. Takeuchi, and Y. Ōnuki, Phys. Rev. B **89**, 241105 (2014).

[151] A. Amato, E. Bauer, and C. Baines, Phys. Rev. B **71**, 092501 (2005).

[152] K. Kaneko, O. Stockert, M. Skoulatos, A. Schneidewind, T. Takeuchi, T. D. Matsuda, Y. Haga, R. Settai, Y. Ōnuki, and N. Metoki, J. Phys. Soc. Jpn. **81**, SB006 (2012).

[153] I. Dzyaloshinsky, J. Phys. Chem. Solids **4**, 241 (1958).

[154] T. Moriya, Phys. Rev. **120**, 91 (1960).

[155] P. Bak and M. H. Jensen, J. Phys. C: Solid State Phys. **13**, L881 (1980).

[156] O. Nakanishi, A. Yanase, A. Hasegawa, and M. Kataoka, Solid State Commun. **35**, 995 (1980).

[157] K. Prokeš, R. Feyerherm, E. Dudzik, V. Sechovský, and M. Mihalik, J. Phys.: Condens. Matter **23**, 076001 (2011).

[158] D. Rauch, S. Süllow, M. Bleckmann, A. Buchsteiner, N. Stüßer, H.-H. Klauss, H. Luetkens, and E. Bauer, J. Phys.: Conf. Ser. **391**, 012055 (2012).

[159] O. Sologub, J. Hesterb, P. Salamakhab, E. Leroyc, and C. Godartc, J. Alloys Comp. **337**, 10 (2002).

[160] L. Vegard, Z. Phys. **5**, 17 (1921).

[161] M. Ohashi, *et al.*, (unpublished).

[162] M. Bleckmann, *Itinerant to localized views on f-electron systems: A multiprobe study*, Ph.D. thesis, TU Braunschweig (2009).

[163] E. Bauer, R. Lackner, G. Hilscher, H. Michor, M. Sieberer, A. Eichler, A. Gribanov, Y. Seropegin, and P. Rogl, J. Phys.: Condens. Matter **17**, 1877 (2005).

[164] C. Kittel, *Einführung in die Festkörperphysik*, 5. Auflage, R. Oldenbourg Verlag München Wien (1980).

[165] M. A. Continentino, S. N. d. Medeiros, M. T. D. Orlando, M. B. Fontes, and E. M. Baggio-Saitovitch, Phys. Rev. B **64**, 012404 (2001).

[166] J. W. Kreitlow, *Druckstudien zu strukturellen und magnetischen Eigenschaften molekularer und molekülbasierter Magnete*, Ph.D. thesis, TU Braunschweig (2008).

[167] N. Tateiwa, Y. Haga, Z. Fisk, and Y. Ōnuki, Rev. Sci. Instrum. **82**, 053906 (2011).

[168] N. Tateiwa, Y. Haga, T. D. Matsuda, S. Ikeda, T. Yasuda, T. Takeuchi, R. Settai, and Y. Ōnuki, J. Phys. Soc. Jpn. **74**, 1903 (2005).

[169] G. Motoyama, Y. Yamaguchi, K. Maeda, A. Sumiyama, and Y. Oda, J. Phys. Soc. Jpn. **77**, 075004 (2008).

[170] J. D. Thompson, Rev. Sci. Instrum. **55**, 2 (1984).

[171] A. Eiling and J. Schilling, J. Phys. F: Metal Phys. **11**, 623 (1981).

[172] L. M. Sandratskii and J. Kübler, Phys. Rev. B **50**, 9258 (1994).

[173] M. Diviš, L. Steinbeck, M. Richter, and P. Mohn, J. Alloys Comp. **321**, 10 (2001).

[174] A. N. Yaresko, V. N. Antonov, and B. N. Harmon, Phys. Rev. B **68**, 214426 (2003).

[175] O. Trovarelli, C. Geibel, S. Mederle, C. Langhammer, F. M. Grosche, P. Gegenwart, M. Lang, G. Sparn, and F. Steglich, Phys. Rev. Lett. **85**, 626 (2000).

[176] C. Pfleiderer, P. Böni, U. K. Rößler, and A. Rosch, Science **316** (2007).

[177] P. Pedrazzini, H. Wilhelm, D. Jaccard, T. Jarlborg, M. Schmidt, M. Hanfland, L. Akselrud, H. Q. Yuan, U. Schwarz, Y. Grin, and F. Steglich, Phys. Rev. Lett. **98**, 047204 (2007).

[178] R. P. Smith, M. Sutherland, G. G. Lonzarich, S. S. Saxena, N. Kimura, S. Takashima, M. Nohara, and H. T. Takagi, Nature **455**, 1220 (2008).

[179] M. Brando, D. Moroni-Klementowicz, C. Albrecht, and F. Grosche, Physica B **378-380**, 111 (2006).

[180] S. Friedemann, M. Brando, W. J. Duncan, A. Neubauer, C. Pfleiderer, and F. M. Grosche, Phys. Rev. B **87**, 024410 (2013).

[181] T. D. Haynes, I. Maskery, M. W. Butchers, J. A. Duffy, J. W. Taylor, S. R. Giblin, C. Utfeld, J. Laverock, S. B. Dugdale, Y. Sakurai, M. Itou, C. Pfleiderer, M. Hirschberger, A. Neubauer, W. Duncan, and F. M. Grosche, Phys. Rev. B **85**, 115137 (2012).

[182] W. J. Duncan, *Quantum Phase Transitions in $NbFe_2$ and $BaFe_2As_2$*, Ph.D. thesis, Royal Holloway, University of London (2010).

[183] A. Neubauer, *Single crystal growth of intermetallic compounds with unusual low temperature properties*, Ph.D. thesis, Physik Department E21, TU München (2011).

[184] A. Neubauer, J. Boeuf, A. Bauer, B. Russ, H. Löhneysen, and C. Pfleiderer, Rev. Sci. Instrum. **82**, 013902 (2011).

[185] M. Brando, L. Pedrero, T. Westerkamp, C. Krellner, P. Gegenwart, C. Geibel, and F. Steglich, Phys. Status Solidi B **250**, 485 (2013).

[186] A. Huxley, I. Sheikin, and D. Braithwaite, Physica **284B**, 1277 (2000).

[187] M. Brando, D. Belitz, F. M. Grosche, and T. R. Kirkpatrick (2015), arXiv:1502.02898.

[188] T. Paschen, S.and Lühmann, S. Wirth, P. Gegenwart, C. Trovarelli, O.and Geibel, F. Steglich, P. Coleman, and Q. Si, Nature **432**, 881 (2004).

[189] S. Friedemann, N. Oeschler, S. Wirth, C. Krellner, C. Geibel, F. Steglich, S. Paschen, S. Kirchner, and Q. Si, J. Phys.: Condens. Matter **23**, 094216 (2011).

[190] Q. Si and S. Paschen, Phys. Status Solidi B **250**, 425 (2013).

[191] Y. Tokiwa, T. Radu, P. Gegenwart, C. Geibel, and F. Steglich, Phys. Rev. Lett. **102**, 066401 (2009).

[192] P. Gegenwart, J. Custers, C. Geibel, K. Neumaier, T. Tayama, K. Tenya, O. Trovarelli, and F. Steglich, Phys. Rev. Lett. **89**, 056402 (2002).

[193] S. Friedemann, S. Wirth, S. Kirchner, Q. Si, S. Hartmann, C. Krellner, C. Geibel, T. Westerkamp, M. Brando, and F. Steglich, J. Phys. Soc. Jpn. **80** (2011), sAICHE Tokyo 2010.

[194] C. Broholm, J. K. Kjems, W. J. L. Buyers, P. Matthews, T. T. M. Palstra, A. A. Menovsky, and J. A. Mydosh, Phys. Rev. Lett. **58**, 1467 (1987).

[195] K. Matsuda, Y. Kohori, T. Kohara, K. Kuwahara, and H. Amitsuka, Phys. Rev. Lett. **87**, 087203 (2001).

[196] M. Shiga and Y. Nakamura, J. Phys. Soc. Jpn. **47**, 1446 (1979).

[197] A. Kerkau, *Disorder in Laves Phases*, Ph.D. thesis, Technische Universität Dresden (2012).

[198] M. Baenitz and M. Brando (2013), private communications.

[199] K. Kai, T. Nakamura, and M. Yamamoto, J. Phys. Soc. Jpn. **29**, 1094 (1970).

[200] H. Wada, M. Hada, M. Shiga, and T. Nakamura, J. Phys. Soc. Jpn. **59**, 701 (1990).

[201] L. S. Guzei, E. M. Sokolovskaya, I. G. Sokolova, G. V. Vysotskaya, G. N. Ronami, and S. M. Kuznetsova, Vestnik Moskovskogo Universiteta Seriya **11**, 696 (1970).

[202] W. Kündig, Nucl. Instrum. Methods Phys. **48**, 219 (1967).

[203] J. A. H. Coaquira, H. R. Rechenberg, and J. Mestnik Filho, J. Alloy. Comp. **288**, 42 (1999).

[204] J. A. H. Coaquira, *Propriedades magnéticas e hiperfinas das ligas* $Zr(Fe_xCr_{1-x})_2$ *e seus hidretos*, Ph.D. thesis, Universität of Sao Paulo (1998).

[205] D. Rauch, S. Süllow, M. Bleckmann, B. Klemke, K. Kiefer, M. S. Kim, M. C. Aronson, and E. Bauer, Phys. Rev. B **86**, 245104 (2012).

[206] Y. Uemura, T. Goko, I. Gat-Malureanu, J. Carlo, P. Russo, A. Savici, A. Aczel, G. MacDougall, J. Rodriguez, G. Luke, S. Dunsiger, A. McCollam, J. Arai, C. Pfleiderer, P. Böni, K. Yoshimura, E. Baggio-Saitovitch, M. Fontes, J. Larrea, Y. Sushko, and J. Sereni, Nature Physics **3**, 29 (2007).

[207] P. Niklowitz, *et al.*, (2014) private communications.

Acknowledgments

At this point I would like to express my gratitude to all of my colleagues, friends and family, who helped and supported me as much as possible during the beautiful and also difficult stages of the completion of this thesis.

First of all, I want to give my "biggest" thank you to my supervisor Prof. Dr. Stefan Süllow, for giving me the opportunity to carry out studies close to quantum critical materials in a wide field of experimental techniques, for having an open ear for all of my rather stupid questions and for motivating me, whenever it was necessary. The time he has sacrificed in the support of this thesis, in particular for correcting my english phrases, was not self-evident. I truly appreciate the fruitful discussions and useful comments to all the scientific challenges. Furthermore, I want to thank him for giving me the opportunity to visit many workshops, conferences and research stayings all over the world.

I would also like to thank Dr. Malte Grosche for the cooperation and provision of samples of $Nb_{1-y}Fe_{2+y}$, and for taking over the job of the second referee. It was always a pleasure to discuss the newest research results of $Nb_{1-y}Fe_{2+y}$ with him. I stayed in his working group at the Cavendish Laboratory in Cambridge for three month during my Master thesis and had the chance to learn the melting of glass for Flux growth preparation and something about the awesome "Harry Potter"-like college life. Thanks to Dr. Yang Zou for inviting me.

Furthermore I would like to thank Prof. Dr. Gertrud Zwicknagl for being the chairman of the examination board and for review this thesis under the

theoretical aspect.

A special thank goes to Prof. Dr. Jochen Litterst, who accompanied me in the exciting measurement times at the PSI, but also supported me in the analysis and with many fruitful discussions about the experimental technique at the microscopic scale: the μSR and the Mössbauer spectroscopy. In this context, I should also not forget to mention Priv.-Doz. Dr. Dirk Menzel for the countless measurements at the commercial SQUID magnetometer.

I am particularly happy about the collaboration with Dr. Manuel Brando and Dr. Michael Baenitz from the Max Planck institute for chemical physics of solids in Dresden. I want to thank for their friendly support, discussions and provision of samples of $Ta(Fe_{1-x}V_x)_2$. Within their bulk and ^{51}V NMR studies we succeeded in the determination of the complex magnetic phase diagram of $Ta(Fe_{1-x}V_x)_2$.

In addition, I want to thank Hiroyuki Hidaka, Seigo Yamazaki and Prof. Dr. Hiroshi Amitsuka for their friendship and support during my stay in their working group at the VLT group at the Hokkaido University in Sapporo. I am grateful for the high pressure experiments with the ceramic anvil pressure cell and also for the "food and drinking" experience in Yokohama and Tokyo.

To my colleagues at the institute of condensed matter physics, TU Braunschweig, goes a very special thanks for their supporting, for the extraordinary work climate with amusing discussions, and as well for the extraordinary conference stayings. These are: Dr. Teresa Henning, Dr. Josefin Engelke, Dr. Dirk Schulze Grachtrup, Dr. Mathias Kraken, Dr. Britta Willenberg and Elaheh Sadrollahi. Moreover, I had the pleasure to work together with several bachelor and master students during their thesis, which were partially closely connected to my work. Namely I would like to mention Philipp Horenburg, Steffen Hartwig and Christoph Balceris.

Furthermore, I am thankful to the workshop, electronics and technical staff, which are especially Lisa Hoffman, Thilo Lampe and Lutz Nagatz for the very fast help and repairs at any time.

During the last year, in the writing process of this thesis, I already worked at the working group of solid state density at the PTB Braunschweig. I thanks this members for their kind support.
Finally, and in no way at least I want to thank my family and my friend Carsten. Especially for the last months I am grateful to Carsten. He always believed in me and had to motivate me for several times. I do appreciate that, he kept my options open whenever it was possible.

"**Thank you!**" to all the people I worked with. I had a memorable nice time!